Title

Quantum Optimal Control of Many-Body Kohn-Sham Systems on Two-Dimensional Domains With Nonregular Meshes

Author

Chen, Yuan

Publication Date

2024

UNIVERSITY OF CALIFORNIA
RIVERSIDE

Quantum Optimal Control of Many-Body Kohn-Sham Systems on Two-Dimensional Domains With Nonregular Meshes

A Dissertation submitted in partial satisfaction
of the requirements for the degree of

Doctor of Philosophy

in

Physics

by

Yuan Chen

September 2024

Dissertation Committee:

Dr. Bryan M. Wong, Chairperson
Dr. Vivek Aji
Dr. Hai-Bo Yu

The Dissertation of Yuan Chen is approved:

Committee Chairperson

University of California, Riverside

Acknowledgments

First and foremost, I wish to express my profound gratitude to my academic supervisor, Prof. Bryan M. Wong, who generously welcomed me into his group despite my being a high-year student at the time. His insightful advice, meticulous editing, and thoughtful support have been invaluable throughout this multi-year journey. I am continually inspired by his serious dedication and boundless energy in research, driving me to persist in my academic endeavors. Additionally, I am thankful to Bryan for his generosity, exemplified by his free lunches and New Year's gifts.

I also extend my appreciation to my committee members, Prof. Vivek Aji and Prof. Hai-Bo Yu, for their time, expertise, and invaluable feedback.

A special debt of gratitude goes to Prof. John W Gary, my former supervisor, who guided me for three years. His leadership in the realm of experimental particle physics and support for my research collaboration at CERN have been instrumental in my journey. His care for both my research and personal well-being has been a constant source of encouragement. Under his supervision, I advanced to PhD candidacy, and though I regret not continuing in that research direction, my appreciation for Prof. Gary's guidance is immeasurable.

I am grateful to Prof. Luat T Vuong for her support and assistance during my effort to resume the Ph.D. program after a year's leave.

Acknowledgment is also due to Prof. Kirill Shtengel for the honor of being part of his group in my program's first year. His profound knowledge and personal instruction have left a lasting impression on me.

I owe many thanks to Dr. Derek E Beving for his assistance with class registration, paperwork processing, and petition handling. His role as my graduate advisor has been fortuitous.

My gratitude extends to Dr. Hua Wei for entrusting me with his project and for his patient explanations. Special thanks go to Yi Zhang, my best labmate and friend at CERN; his presence made both my research and life there significantly smoother. I also thank Dr. Xian Wang for introducing me to Prof. Bryan, Dr. Zulfikhar A. Ali for his consistent, heartfelt help and guidance, and Dr. Qiang Xu for many enriching academic discussions. Appreciation is also due to Dr. Mahmut Okyay and Simon Sandhofer for their help in proofreading and revising my papers. Additionally, I am grateful to all my labmates and colleagues at CERN and UCR; their companionship made my days vibrant and fulfilling.

Finally, I extend my deepest and sincerest thanks to my family members, whose unwavering support and companionship have been my strength throughout this journey.

To my parents for all the support and love

ABSTRACT OF THE DISSERTATION

Quantum Optimal Control of Many-Body Kohn-Sham Systems on Two-Dimensional Domains With Nonregular Meshes

by

Yuan Chen

Doctor of Philosophy, Graduate Program in Physics
University of California, Riverside, September 2024
Dr. Bryan M. Wong, Chairperson

Density functional theory (DFT) is an effective computational model that enables calculations of properties and dynamical evolution under external fields for quantum many-body systems from first principles. On the other hand, there has been a burgeoning interest in addressing the "inverse" problem: Can we design a control field to steer a quantum system toward a desired configuration? Quantum Optimal Control (QOC) has risen to prominence as a potent framework in this regard. A lot of progress has been made, especially for the finite-dimensional quantum spin system. However, the optimal control of interacting many-body systems is a relatively young research field.

The first part of this dissertation presents a computational scheme that integrates the exact nonlocal exchange operator into ground-state calculations for multi-shell nanowires with various cross-sectional shapes, employing the finite element method. This method is applied to several core-shell nanowires, underscoring the crucial role of the nonlocal exchange operator. We demonstrate its significant influence on electronic properties, such as electron occupancy numbers, energy eigenvalues, energy separations, and electron localization patterns.

The latter half of this work delineates a computational methodology for applying QOC to interacting many-body systems within arbitrary geometric domains within the DFT context. Employing the Lagrangian multiplier method, we derive the gradient expression for the loss functional. A propagator integration method (Green's function) is implemented to evolve wavefunctions forward and backward, incorporating the WKB approximation to accommodate spatially varying effective electron mass. This optimization problem is iteratively solved to determine the optimal control field. Our approach is validated through a test example and subsequently applied to two complex systems, demonstrating its reliability and efficacy. These applications also allow us to investigate the effects of varying propagation times on control strategies and explore the feasibility of manipulating entire systems using localized control potentials.

Contents

List of Figures

List of Tables

Chapter 1

Introduction

This chapter begins with a concise overview of Density Functional Theory (DFT), a powerful framework for addressing the many-body Schrödinger equation. This theory underpins the research presented in Chapters 2 and 3. Subsequently, we explore Quantum Optimal Control (QOC), particularly its application to multi-electron interacting quantum systems, which forms the core subject of Chapter 3.

1.1 Density Functional Theory: Solving Many-Body Systems

At the atomic and subatomic scale, the quantum mechanism governs the evolution and behavior of systems. In the non-relativistic regime, the most general form of the equation of motion is the Schrödinger equation. Theoretically, by resolving this equation in conjunction with electromagnetic and statistical mechanical principles, we could unravel the entire dynamics of any condensed matter system. Such a method falls under the realm of first-principle calculations, which derive all system physics from fundamental assumptions or axioms without relying on empirical or experimental data. This approach is relatively straightforward for single entities, such as an electron or a nucleus. However, real-world scenarios frequently necessitate the examination of many-body interacting systems. Additionally, unique phenomena often emerge at the mesoscopic scale (between the nanometer and the micron) [1, 2]. The particle count in such systems can range from hundreds to approximately 6×10^{23} (Avagadros number). In other words, we have to solve a many-body wavefunction

$$\Psi_{\mathrm{MB}}(\mathbf{r}_1, \mathbf{r}_2, \cdots, \mathbf{r}_N), \tag{1.1}$$

conforming to the Schrödinger equation

$$i\hbar \frac{\partial \Psi_{\mathrm{MB}}}{\partial t} = \left(\hat{T} + \hat{V}\right) \Psi_{\mathrm{MB}}, \tag{1.2}$$

where $\mathbf{r}_i$ is the coordinate of the i-th partical, and $\hat{T}$ and $\hat{V}$ denote the kinetic energy and total potential energy operator. If we know the many-body wavefunction Ψ_{MB}, all properties can be calculated using Ψ_{MB}. For example, we can compute the expectation value of an observable $\hat{\mathcal{O}}$ by $\langle \Psi_{\mathrm{MB}} | \hat{\mathcal{O}} | \Psi_{\mathrm{MB}} \rangle$. Unfortunately, solving Eq. 1.2 for large N is practically unfeasible due to the immense computational and storage requirements, compounded by the complexity of particle interactions, notably Coulombic interactions [1]. This challenge paves the way for the application of DFT, which we will discuss in the following section.

1.1.1 The Hohenberg-Kohn Theorem

Density Functional Theory (DFT) stands as a computational paradigm that facilitates first-principle calculations of many-body systems, striking a balance between accuracy and computational efficiency. Central to DFT is the Hohenberg-Kohn theorems [3], which form its foundational principles. The first of these theorems establishes a unique correspondence between the ground state density, denoted as $n_0(\mathbf{r})$, and the external potential $v(\mathbf{r})$, apart from a constant of trivial significance. This correlation has profound implications. It suggests that knowledge of the ground state density effectively determines the external potential and, consequently, the Hamiltonian. Therefore, resolving Eq. 1.2 would yield the many-body wavefunction. As such, the ground state density is pivotal in defining all system properties, encompassing both ground and excited states. This insight leads to an intriguing proposition: By solving for the ground state density, rather than the more complex many-body wavefunction, we can extract all desired quantities, reducing the degrees of freedom from $3N$ to just 3.

But the question arises, how do we ascertain $n_0(\mathbf{r})$? Given that Ψ_{MB} is a unique functional of $n_0(\mathbf{r})$, the ground state energy $E_0[n_0(\mathbf{r})]$ can also be written as a functional of $n_0(\mathbf{r})$. The second Hohenberg-Kohn theorem states that the ground state density of the system is the density that minimizes E_0. Thus, these theorems substantially simplify the problem's dimensionality, allowing us to approach the determination of the ground state density as an optimization problem.

Nevertheless, from a practical standpoint, the above theorems, despite their theoretical significance, do not directly facilitate the resolution of the problem, as the explicit form of the functional $E_0[n(\mathbf{r})]$ remains generally unknown. The access to the form of $E_0[n(\mathbf{r})]$ would requie solving Eq. 1.2. In practical applications, approximate forms of the functional $E_0[n(\mathbf{r})]$ are employed, which can then be computationally minimized, providing a pragmatic approach to tackling this intricate problem.

1.1.2 The Kohn-Sham Method

For an interacting many-body system, the ground-state energy can be decomposed into distinct components, as expressed in the following equation:

$$\mathrm{E}_0 = \mathrm{T} + \mathrm{E}_{ee} + \int n_0(\mathbf{r}) v(\mathbf{r}) \mathrm{d}\mathbf{r}, \tag{1.3}$$

where T is the kinetic energy, E_{ee} is the expectation value of the electron-electron repulsion operator, and the last term $\int n_0(\mathbf{r}) v(\mathbf{r}) \mathrm{d}\mathbf{r}$ corresponds to the energy due to the external potential $v(\mathbf{r})$. Notably, only the latter term is directly a functional of electron density. Being rigorous, E_{ee} is defined as:

$$\mathrm{E}_{ee} = \frac{1}{2} \int \frac{\rho_2(\mathbf{r}_1, \mathbf{r}_2)}{|\mathbf{r}_1 - \mathbf{r}_2|} \mathrm{d}\mathbf{r}_1 \mathrm{d}\mathbf{r}_2, \tag{1.4}$$

where $\rho_2(\mathbf{r}_1, \mathbf{r}_2)$ is the electron pair density, given by:

$$\rho_2(\mathbf{r}_1, \mathbf{r}_2) = N(N-1) \int \cdots \int \left| \Psi_{\mathrm{MB}}(\mathbf{r}_1, \mathbf{r}_2, \cdots, \mathbf{r}_N) \right|^2 \mathrm{d}\mathbf{r}_3 \cdots \mathrm{d}\mathbf{r}_N. \tag{1.5}$$

The pair density encapsulates the probability density for one electron at position $\mathbf{r}_1$ and another electron at position $\mathbf{r}_2$ simultaneously. Recall that the electron density is defined as:

$$n(\mathbf{r}_1) = N \int \cdots \int \left|\Psi_{\mathrm{MB}}(\mathbf{r}_1, \mathbf{r}_2, \cdots, \mathbf{r}_N)\right|^2 \mathrm{d}\mathbf{r}_2 \mathrm{d}\mathbf{r}_3 \cdots \mathrm{d}\mathbf{r}_N. \tag{1.6}$$

It is important to note that $\rho_2(\mathbf{r}_1, \mathbf{r}_2) \neq n(\mathbf{r}_1)n(\mathbf{r}_2)$, due to the inherent correlation effects between electrons. However, it is convenient to separate $\rho_2(\mathbf{r}_1, \mathbf{r}_2)$ into two parts, one being $n(\mathbf{r}_1)n(\mathbf{r}_2)$ [4]:

$$\rho_2(\mathbf{r}_1, \mathbf{r}_2) = n(\mathbf{r}_1)n(\mathbf{r}_2)\left(1 + f(\mathbf{r}_1, \mathbf{r}_2)\right), \tag{1.7}$$

where $f(\mathbf{r}_1, \mathbf{r}_2)$ is the correlation factor accounting for the correlation effects. However, expressing E_{ee} as a functional of electron density remains a challenge.

Another term in Eq. 1.3 that is not readily a functional of the electron density is the kinetic energy T. Kohn and Sham proposed [5] the approximation of this kinetic energy, T_s, using a system of noninteracting electrons. This fictitious system should mimic the ground state density $n_0(\mathbf{r})$ of the original interacting system. In sum, the Kohn-Sham (KS) model writes the ground-state energy E_0 as:

$$\mathrm{E}_0 = \int n_0(\mathbf{r})v(\mathbf{r})\mathrm{d}\mathbf{r} + \mathrm{T}_s + \frac{1}{2}\int\int \frac{n(\mathbf{r}_1)n(\mathbf{r}_2)}{|\mathbf{r}_1 - \mathbf{r}_2|}\mathrm{d}\mathbf{r}_1\mathrm{d}\mathbf{r}_2 + \mathrm{E}_{\mathrm{xc}}, \tag{1.8}$$

where E_{xc} is the exchange-correlation energy, which contains all the unaccounted aspects. E_{xc} is the difference between the true total energy E_0 and the combined terms consisting of external potential energy $\int n_0(\mathbf{r})v(\mathbf{r})\mathrm{d}\mathbf{r}$, kinetic energy of the noninteracting system T_s and the classical Coulomb interaction $\frac{1}{2}\int\int \frac{n(\mathbf{r}_1)n(\mathbf{r}_2)}{|\mathbf{r}_1-\mathbf{r}_2|}\mathrm{d}\mathbf{r}_1\mathrm{d}\mathbf{r}_2$. Specifically, E_{xc} contains the exchange, correlation and correction to the kinetic energy.

The KS model introduces a noninteracting reference system required to have identical electron density. In fact, we could solve this noninteracting system instead to get the electron density since calculations are much easier. The Hamiltonian for this noninteracting reference system is written as:

$$\hat{H}_{\mathrm{S}} = -\frac{1}{2}\sum_{i=1}^{N}\nabla_i^2 + \sum_{i=1}^{N} V_{\mathrm{S}}(\mathbf{r}_i),\ i = 1, \cdots, N, \tag{1.9}$$

where $V_{\mathrm{S}}(\mathbf{r})$ is a local potential to be decided later. Note that there are no coupling terms between different electrons in the Hamiltonian. Thus, solving this system is equivalent to resolving a single-particle Schrödinger equation:

$$\left(-\frac{1}{2}\nabla^2 + V_{\mathrm{S}}\right)\psi_i = \epsilon_i\psi_i,\ i = 1, \cdots, N, \tag{1.10}$$

where ϵ_i is the eigen-energy of the i-th particle, and $\{\psi_i\}$ is a set of one-particle wavefunctions or KS orbitals. The electron density is given by:

$$n_{\mathrm{S}}(\mathbf{r}) = \sum_{i=1}^{N} |\psi_i(\mathbf{r})|^2. \tag{1.11}$$

By requiring $n_{\mathrm{S}} = n_0$, it can be shown [5] that the effective local potential V_{S} should satisfy the following:

$$V_{\mathrm{S}}(\mathbf{r}) = v(\mathbf{r}) + \int \frac{n(\mathbf{r}')}{|\mathbf{r} - \mathbf{r}'|}\mathrm{d}\mathbf{r}' + v_{\mathrm{xc}}(\mathbf{r}), \tag{1.12}$$

where the exchange-correlation potential $v_{\mathrm{xc}}(\mathbf{r})$ is defined as $v_{\mathrm{xc}}(\mathbf{r}) = \delta \mathrm{E}_{\mathrm{xc}}[n]/\delta n(\mathbf{r})$. If we know the exact form of v_{xc}, we can solve the one-particle equation 1.10 to determine the orbitals $\{\psi_i\}$ and hence the electron density via Eq. 1.11 and the ground state energy by Eq. 1.8. In reality, of course, the exact form of $v_{\text{xc}}(\mathbf{r})$ is unknown and always approximated. Some commonly used functionals include local density approximation (LDA), generalized gradient approximations (GGAs), screened exchange (sX-LDA), and exact exchange (EXX) [6].

1.1.3 The Hartree-Fock Method

We introduce the Hartree-Fock (HF) method, an alternate computational strategy for many-body systems. Contrasting with the electron density focus of Density Functional Theory (DFT), the HF method directly addresses the many-body wavefunction. Specifically, the method approximates the exact many-body wavefunction by a Slater determinant of N one-particle wavefunctions $\{\psi_i\}$:

$$\Psi_{\text{HF}} = \frac{1}{\sqrt{N!}} \begin{vmatrix} \psi_1(\mathbf{r}_1) & \psi_2(\mathbf{r}_1) & \cdots & \psi_N(\mathbf{r}_1) \\ \psi_1(\mathbf{r}_2) & \psi_2(\mathbf{r}_2) & \cdots & \psi_N(\mathbf{r}_2) \\ \vdots & \vdots & \ddots & \vdots \\ \psi_1(\mathbf{r}_N) & \psi_2(\mathbf{r}_N) & \cdots & \psi_N(\mathbf{r}_N) \end{vmatrix}. \tag{1.13}$$

This formulation ensures the antisymmetry requirement for a fermionic system. The next step involves determining the best forms of the N one-particle wavefunctions $\{\psi_i\}$ (HF orbitals) using the variational principle. The total energy is defined as:

$$\begin{aligned}\mathrm{E}_{\mathrm{HF}} &= \langle \Psi_{\mathrm{HF}} | \hat{H}_{\mathrm{HF}} | \Psi_{\mathrm{HF}} \rangle \\ &= \langle \Psi_{\mathrm{HF}} \left| -\frac{1}{2} \sum_{i=1}^{N} \nabla_i^2 + \sum_{i=1}^{N} \sum_{j>i} \frac{1}{|\mathbf{r}_i - \mathbf{r}_j|} \right| \Psi_{\mathrm{HF}} \rangle.\end{aligned} \tag{1.14}$$

The objective is to vary $\{\psi_i\}$ to minimize the energy E_{HF}. It can be derived [7] that the HF orbitals should satisfy the following Hartree-Fock equations:

$$\hat{F}\psi_i = \varepsilon_i \psi_i. \tag{1.15}$$

The Hartree-Fock operator $\hat{F}$ is defined as:

$$\hat{F} = -\frac{1}{2}\nabla^2 + \sum_{j=1}^{N} \left(\hat{J}_j - \hat{K}_j \right). \tag{1.16}$$

The Coulomb operator $\hat{J}_j$ is given by:

$$\hat{J}_j(\mathbf{r}) = \int \psi_j^*(\mathbf{r}') \frac{1}{|\mathbf{r} - \mathbf{r}'|} \psi_j(\mathbf{r}') \mathrm{d}\mathbf{r}', \tag{1.17}$$

which corresponds to the classical Coulomb interaction between electrons. The exchange operator $\hat{K}_j$ is defined through its application upon an orbital ψ_i:

$$\hat{K}_j(\mathbf{r})\psi_i(\mathbf{r}) = \int \psi_j^*(\mathbf{r}') \frac{1}{|\mathbf{r} - \mathbf{r}'|} \psi_i(\mathbf{r}') \psi_j(\mathbf{r}) \mathrm{d}\mathbf{r}'. \tag{1.18}$$

This exchange term has no corresponding classical interpretation and is a purely quantum effect resulting from the antisymmetry of fermionic wavefunctions. In addition, $\hat{K}_j$ is a nonlocal operator since the operation of $\hat{K}_j$ on ψ_i depends on the value of ψ_i throughout the entire space. It is also noteworthy that the orbital energy ε_i in Eq. 1.15 carries physical meaning as per Koopmans' theorem [8, 4]: the energy corresponding to the highest occupied orbital is equal to the negative of the first ionization energy of the system.

The HF approach, as delineated in Eq. 1.15, effectively transforms the complex many-body equation into a more tractable one-particle Schrödinger equation. This transformation bears a formal resemblance to the approach in DFT (refer Eq. 1.10). However, a crucial distinction must be underscored: the wavefunction Ψ_{HF} in the HF method does not represent the true many-body wavefunction. Consequently, the electron density computed from $|\Psi_{\mathrm{HF}}|^2$ does not match the actual density. In contrast, within the DFT framework, the electron density calculated from Eq. 1.11 *is* the real density by definition. The disparity arises when approximating the unknown exchange-correlation potential v_{xc} in Eq. 1.12, leading to approximations in KS orbitals and, hence, the electron density. In HF, the discrepancy between the calculated density $|\Psi_{\mathrm{HF}}|^2$ and the real density stems from the assumption that Ψ_{HF} is the many-body wavefunction. However, in DFT, the difference originates from the approximation of v_{xc}. Furthermore, the HF method does not account for electron correlation effects, although it does offer an exact formulation of the exchange operator. It is also pertinent to note that, unlike in the HF framework, the eigenvalues of the KS orbitals in DFT lack strict physical interpretations. Detailed discussions on the practical solutions to Eqs 1.10 and 1.15 will be provided in Chapters 2 and 3, focusing on their computational aspects.

1.2 Quantum Optimal Control: The Inverse Problem

In the preceding section, we explored the Kohn-Sham (KS) formalism, an instrumental approach for calculating electron density in many-body systems and understanding their evolution under external influences such as electromagnetic fields. This methodology has significantly advanced our comprehension of complex condensed matter systems and their interactions with external fields. In recent years, there has been a growing interest in the inverse problem: Given a desired target configuration for a system, can we design an external field to achieve this objective, and if so, how? Addressing such inverse problems is crucial, as it enables us to convert scientific knowledge into practical technological applications and enhance productivity.

Quantum Optimal Control (QOC) emerges as a framework designed to craft the temporal profiles of external fields, aiming to manipulate atomic or molecular system dynamics and accomplish specific tasks efficiently. QOC is an interdisciplinary field encompassing elements from mathematics, physics, and computer science. Significant theoretical and experimental advancements have been made in QOC, particularly concerning the controllability and optimization of control methods, especially in finite-dimensional open quantum systems [9]. This dissertation focuses on the application of QOC to interacting many-body systems, which are, in principle, infinite-dimensional. This area of research gained prominence about a decade ago, marked by A. Castro et al. (2012) [10], who proposed a scheme for QOC calculations in many-electron systems. Subsequently, A. Borzì et al. (2017) [11] gave a rigorous discussion on the existence of solutions. Building upon these foundational works, this dissertation presents a novel computational scheme to perform QOC calculations for many-electron systems. This scheme is distinctive in its ability to handle systems characterized by spatially varying effective mass on arbitrary two-dimensional cross-sectional geometries within the effective mass formulation. The details of this approach and its implications are elaborated in Chapter 3.

Chapter 2

SHORYUKEN: An Open-Source Software Package for Calculating Nonlocal Exchange Interactions in Nanowires

This chapter incorporates the effect of nonlocal exchange when calculating electrons' properties in nanowires. The work in this chapter resulted from a collaboration with Simon N. Sandhofer and was published as an article in *Computer Physics Communications* [12]. The full paper is presented below, with the supplementary information in Appendix A, B, C and D.

2.1 Abstract

We present the open-source software package, SHORYUKEN (Streamlined High-level Operations in Real-space to Yield, Understand, and Keep Exchange in Nanowires), for calculating nonlocal exchange interactions in nanowires with arbitrary geometries, sizes, doping densities, and compositions. In addition to enabling new calculations of nonlocal exchange, the SHORYUKEN software package is a significant enhancement of our previous HADOKEN code and includes new algorithmic improvements as well as an improved treatment of surface states for nanowires with intrinsic polarization. Our calculations show that the inclusion of nonlocal exchange can have significant effects on the eigenenergy spectrum, number of occupied states, and distribution of electrons within these nanosystems. The open-source SHORYUKEN software package is the first open-source code for calculating nonlocal exchange to predict electron gas formation in nanowire systems with arbitrary cross-sectional geometries.

2.2 Introduction

Semiconducting nanowires have enabled a variety of applications in physics, chemistry, and materials science due to the novel electronic properties that emerge from their reduced dimensionality. Understanding and predicting these electronic properties provides the fundamental knowledge to design and further improve next-generation electronic and optoelectronic devices with these unique nanoscale materials. In particular, semiconducting nanowires have already shown immense potential in high-power devices and electronics due to their tailorable bandgaps and enhanced electron mobilities [13, 14, 15]. Specifically, the emergence of a two-dimensional electron gas (2DEG) at the heterojunction interface in core–shell nanowires [16, 17] can be further manipulated to enable unique quantum properties in these nanostructures. By modulating the doping density and geometry of the nanowire, a sheet of high-density electrons or a quasi-one-dimensional electron gas (Q1DEG) can form at the interface [18, 19]. However, experimentally probing the large parameter space of doping densities, core-shell compositions, and cross-section geometries/sizes is a formidable endeavor. Computational approaches for predicting the properties of these semiconducting core-shell nanowires can play a central role in accelerating future technological developments with these promising nanoscale systems.

The conventional approach for calculating electronic properties of large core-shell nanowires (and bulk heterostructure junctions in general) is via a coupled Schrödinger-Poisson treatment within the effective mass approximation [20, 21], which produces band-bending diagrams, wavefunctions, and electron densities. However, this simplistic approach neglects important quantum mechanical electron-electron exchange interactions, resulting in well-known self-interaction errors [22, 23, 24] that yield inaccurate bandgap/quasiparticle energies [25, 26], overestimation of charge-transfer effects [27], and inaccurate excited-state properties [27, 28, 29]. Previous studies have approximated these electron-electron exchange interactions in nanowires using a simplistic local density approximation (LDA) [19, 30]. However, studies by us and others have shown that *local* exchange-correlation effects have negligible effects on the results [19, 21], and the calculation of electronic properties in molecules and bulk systems can be significantly improved with nonlocal exchange. In addition, there has been recent work on one-dimensional nanotube systems that have utilized their intrinsic geometric symmetry to enable efficient *ab initio* simulations of large nanostructures [31, 32]. It is worth mentioning that our group was the first to implement nonlocal exchange in cylindrically symmetric nanowires, which reduces the electronic structure calculation to a significantly simpler one-dimensional form [33]. While this greatly simplifies the calculations, it severely limits the types of systems that can be explored since (1) many nanowires do not have cylindrical symmetry and, more importantly, (2) geometric effects have been shown to play a critical role in electron localization in nanowire systems [19, 30]. Although the implementation of nonlocal exchange in atomistic calculations is well known, previous work on assessing nonlocal exchange effects in large nanowires (which can have complex geometries) in the effective mass approximation is nonexistent.

In this work, we present the open-source software package, SHORYUKEN (Streamlined High-level Operations in Real-space to Yield, Understand, and Keep Exchange in Nanowires), for calculating nonlocal exchange interactions in nanowires with arbitrary geometries, sizes, doping densities, and compositions. The SHORYUKEN code is written in the high-level MATLAB programming environment for enhanced readability and accessibility to both experimentalists and theorists. By solving the modified nonlocal exchange equations on a flexible finite-element grid, the SHORYUKEN software package is a significant enhancement of our previous HADOKEN code, which is only capable of carrying out conventional Schrödinger-Poisson calculations. To highlight the new capabilities of the SHORYUKEN code, Section 2.3 gives a brief derivation of how the integro-differential nonlocal exchange equations are reduced to simultaneous, coupled partial differential equations. Section 2.4 provides additional numerical implementation details for solving the coupled nonlocal exchange equations on a finite element grid. Section 2.5 presents calculations for several nanowire systems and highlights specific situations where nonlocal exchange gives qualitatively different results than the conventional Schrödinger-Poisson treatment. In addition, Section 2.5.2 presents an improved model for treating surface states in nanowires possessing an intrinsic polarization. Finally, Section 2.6 concludes with a summary and future perspective on situations where many-body nonlocal exchange effects can play a significant role in electron gas formation in these heterostructure nanowires.

2.3 Theory and Methodology

To understand the new nonlocal exchange and algorithmic enhancements in the SHORYUKEN code, we briefly summarize the GaN/AlGaN core-shell nanowire systems used in our calculations and point the reader to our previous work on 2DEG formation in GaN/AlGaN nanowires for further details [19, 30]. Fig. 2.1 depicts the hexagonal and triangular GaN/AlGaN core-shell nanowires that support 2DEG formation and have been synthesized in several previous studies [34, 35, 36, 37, 38, 39, 40, 41]. In our work, each nanowire is composed of an $Al_{0.3}Ga_{0.7}N$ shell with uniform thickness, t, that fully surrounds a GaN core of side length c. The shell side length, s, is related to t and c via the expressions $s = 2t/\sqrt{3} + c$ and $s = 2\sqrt{3}t + c$ for hexagonal and triangular cross-sections, respectively. For the hexagonal nanowire, the longitudinal axis is aligned in the [0001]-direction, and the cross-section is bounded by the $\{10\bar{1}0\}$ planes. For nanowires with a triangular cross-section, the axis is aligned in the $[11\bar{2}0]$-direction, and the cross-section is bounded by two equivalent $(\bar{1}10\bar{1})$ and $(\bar{1}101)$ planes, and the (0001) plane. As shown in Fig. 2.1,

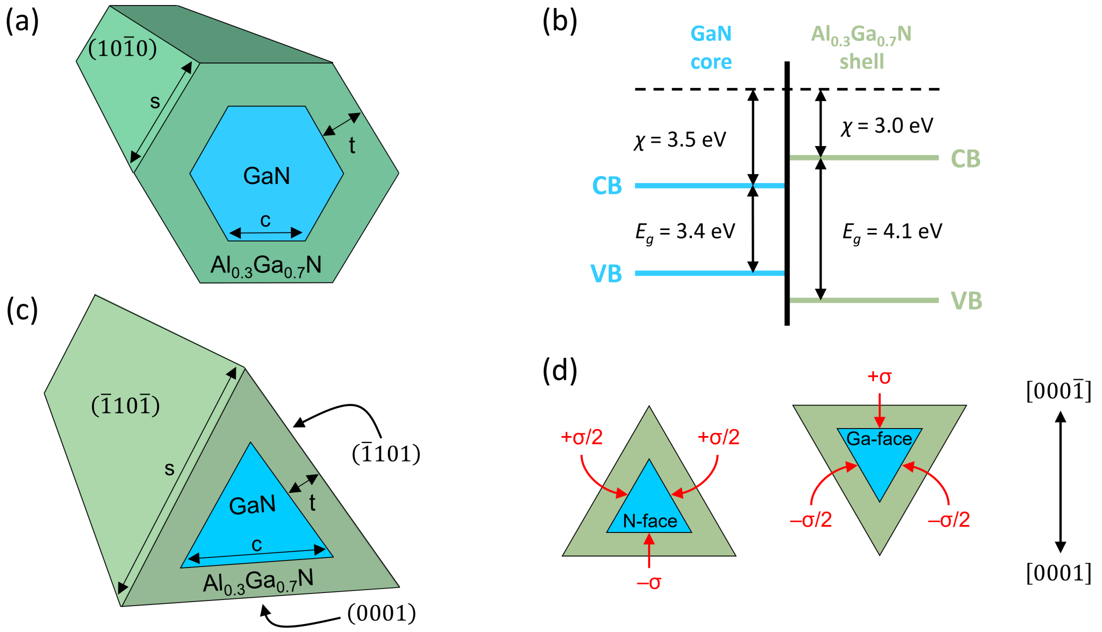

Figure 2.1: Schematics of the (a) hexagonal and (c) triangular GaN/$Al_{0.3}Ga_{0.7}N$ core-shell nanowires considered in this work. The longitudinal axes of the hexagonal and triangular nanowires are aligned in the [0001] and $[11\bar{2}0]$ directions, respectively. (b) Valence band (VB) and conduction band (CB) alignment at the core-shell interface with a $\Delta E_c = 0.5\,\text{eV}$ conduction band discontinuity between the GaN core and $Al_{0.3}Ga_{0.7}N$ shell. (d) Two possible crystallographic orientations of the triangular heterostructure: the (0001) Ga-face and $(000\bar{1})$ N-face orientations. Each orientation has one polar interface with a charge density of $\pm\sigma$ and two semi-polar interfaces with a charge density of $\mp\sigma/2$.

the triangular nanowires have two possible orientations of the (0001) plane, either in the $[000\bar{1}]$ or [0001] direction, which correspond to physically distinct configurations. In the scientific literature, the $[000\bar{1}]$-configuration is referred to as the N-terminated face, and the [0001]-configuration is known as the Ga-terminated face.

To incorporate nonlocal exchange in our nanowire systems, the SHORYUKEN code uses a modified Hartree-Fock formalism to enable efficient calculations in the finite element basis. In this study, we focus solely on closed-shell systems with an even number of electrons where each of the occupied spatial orbitals of the nanowire, Ψ_i, are doubly occupied. Accordingly, the fully antisymmetric wavefunction has the form $|\Psi_1, \bar{\Psi}_1, \Psi_2, \bar{\Psi}_2, ..., \Psi_N, \bar{\Psi}_N|$, where an overbar (lack of an overbar) denotes a spatial wavefunction with a spin-down (spin-up) electron. Using this antisymmetric form of the wavefunction, the generalized Hartree-Fock equation [42, 43, 33] for the envelope wavefunction becomes

$$\begin{split}\left[-\frac{\hbar^2}{2}\nabla_i \cdot \frac{1}{m^*(\mathbf{r}_i)}\nabla_i + V_{\mathrm{n}}(\mathbf{r}_i) + V_{\mathrm{CB}}(\mathbf{r}_i) + 2\sum_{j=1}^{N}\hat{v}_{\mathrm{D},j}(\mathbf{r}_i) - \sum_{j=1}^{N}\hat{v}_{\mathrm{EXX},j}(\mathbf{r}_i)\right]\Psi_i(\mathbf{r}_i) \\ = E_i\Psi_i(\mathbf{r}_i),\end{split} \tag{2.1}$$

where $\hbar$ is the reduced Planck constant, $m^*(\mathbf{r}_i)$ is the spatially-dependent effective mass of the electron, $V_{\mathrm{n}}(\mathbf{r}_i)$ is the potential introduced by the ionized dopants, and $V_{\mathrm{CB}}(\mathbf{r}_i)$ is the potential of the conduction band edge. $\hat{v}_{\mathrm{D},j}(\mathbf{r}_i)$ (the prefactor of 2 accounts for spin degeneracy) is the direct potential energy due to electron-electron repulsion, and $\hat{v}_{\mathrm{EXX},j}(\mathbf{r}_i)$ is the nonlocal exchange operator resulting from the antisymmetrization requirement of the total wavefunction. $\Psi_i(\mathbf{r}_i)$ is the envelope wavefunction for state i with energy E_i, and N is the number of doubly-occupied spatial wavefunctions. The envelope wavefunction represents the slowly varying component of the total wavefunction in the presence of a periodic arrangement of atoms (see Chapter 6 of Ref. [44]).

The direct interaction term in Eq.2.1 takes the following form:

$$\hat{v}_{\mathrm{D},j}(\mathbf{r}_i)\Psi_i(\mathbf{r}_i) = \left[\int \Psi_j^*(\mathbf{r}_j)G(\mathbf{r}_i, \mathbf{r}_j)\Psi_j(\mathbf{r}_j)\mathrm{d}^3\mathbf{r}_j\right]\Psi_i(\mathbf{r}_i), \tag{2.2}$$

where $G(\mathbf{r}_i, \mathbf{r}_j)$ is the Green's function satisfying the following Poisson equation:

$$-\nabla_i \cdot \varepsilon^*(\mathbf{r}_i)\nabla_i G(\mathbf{r}_i, \mathbf{r}_j) = \frac{e^2}{\varepsilon_0}\delta(\mathbf{r}_i - \mathbf{r}_j), \tag{2.3}$$

where ε_0 is the vacuum permittivity, and $\varepsilon^*(\mathbf{r}_i)$ is the position-dependent relative permittivity. The nonlocal exchange interaction term is given by swapping the indexes of Ψ_j and Ψ_i in Eq. 2.2:

$$\hat{v}_{\mathrm{EXX},j}(\mathbf{r}_i)\Psi_i(\mathbf{r}_i) = \left[\int \Psi_j^*(\mathbf{r}_j)G(\mathbf{r}_i, \mathbf{r}_j)\Psi_i(\mathbf{r}_j)\mathrm{d}^3\mathbf{r}_j\right]\Psi_j(\mathbf{r}_i). \tag{2.4}$$

$\hat{v}_{\mathrm{EXX},j}(\mathbf{r}_i)$ is a nonlocal operator in the sense that the result of $\hat{v}_{\mathrm{EXX},j}$ acting on $\Psi_i(\mathbf{r}_i)$ not only depends on the local value of Ψ_i near $\mathbf{r}_i$ but also its integral over all space, as shown in Eq. 2.4.

Assuming translational invariance of the nanowire along the z-axis, the wavefunction, Ψ_i, can be written as

$$\Psi_i(\mathbf{r}_i) = \frac{e^{ik_i z_i}}{\sqrt{L}}\psi_{n_i}(x_i, y_i), \tag{2.5}$$

where L is a normalization factor along the axis of the nanowire, k_i is the wavevector along the z-axis, $\psi_{n_i}(x_i, y_i)$ is the two-dimensional wavefunction across the nanowire cross-section, and n_i denotes different quantum states for $\psi_{n_i}(x_i, y_i)$.

Substituting Eq. 2.5 into Eq. 2.1 and restricting our calculations to the Gamma point (i.e., $k = 0$), we obtain (see A for further details) the following two-dimensional Schrödinger equation:

$$\left[-\frac{\hbar^2}{2}\nabla_{x_i,\,y_i}\cdot\frac{1}{m^*(x_i,y_i)}\nabla_{x_i,\,y_i}+V_{\mathrm{n}}(x_i,y_i)+V_{\mathrm{CB}}(x_i,y_i)\right]\psi_{n_i}(x_i,y_i)$$
$$+2\sum_{n_j}V_{\mathrm{D},\,n_j}(x_i,y_i)\;\psi_{n_i}(x_i,y_i)\;-\sum_{n_j}V_{\mathrm{EXX},\,n_j}(x_i,y_i)\;\psi_{n_j}(x_i,y_i)\;=\epsilon_i\,\psi_{n_i}(x_i,y_i), \tag{2.6}$$

where ∇_{x_i,y_i} is the two-dimensional gradient operator, and ϵ_i is the eigenenergy for the cross-sectional wavefunction $\psi_{n_i}(x_i,y_i)$. $V_{\mathrm{D},\,n_j}(x_i,y_i)$ and $V_{\mathrm{EXX},\,n_j}(x_i,y_i)$ are the two-dimensional direct Coulomb and exchange potentials, defined in Eq. A.14 and A.15 respectively, which are obtained by solving the following two-dimensional Poisson equations at $T = 0$ K (cf. A):

$$\nabla_{x_i,y_i}\cdot\varepsilon^*(x_i,y_i)\nabla_{x_i,y_i}V_{\mathrm{D},n_j}(x_i,y_i)=-\frac{1}{\pi\hbar}\frac{e^2}{\varepsilon_0}\sqrt{\frac{m^*(x_i,y_i)(E_F-\epsilon_j)}{2}}\;\left|\psi_{n_j}(x_i,y_i)\right|^2, \tag{2.7}$$

$$\nabla_{x_i,y_i}\cdot\varepsilon^*(x_i,y_i)\nabla_{x_i,y_i}V_{\mathrm{EXX},n_j}(x_i,y_i)=-\frac{1}{\pi\hbar}\frac{e^2}{\varepsilon_0}\sqrt{\frac{m^*(x_i,y_i)(E_F-\epsilon_j)}{2}}\;\psi^*_{n_j}(x_i,y_i)\psi_{n_i}(x_i,y_i), \tag{2.8}$$

where E_F is the Fermi level of the system.

The expressions in Eqs. 2.6, 2.7, and 2.8 must be solved simultaneously and iteratively until the solutions are self-consistent (i.e., the potential used to compute the wavefunctions is the same as the potential that those wavefunctions generate within numerical precision). At the same time, we enforce the charge neutrality condition:

$$\iint \mathrm{d}x\mathrm{d}y\ n_{\mathrm{e}}(x,y) = \iint \mathrm{d}x\mathrm{d}y\ n_{\mathrm{D}}(x,y), \tag{2.9}$$

where n_{e} and n_{D} are the electron and donor number densities, respectively, which are discussed further below. The solution to Eq. 2.9 determines the Fermi level, E_F, by requiring that the total amount of negative and positive charges are equal. The source of positive charges comes from the density of ionized dopants in the nanowire, $n_{\mathrm{D}}(x,y)$, which is a parameter that can be inputted in the SHORYUKEN code by the user. The potential energy, $V_{\mathrm{n}}(x,y)$, due to these ionized dopants (if present) can be obtained by solving another Poisson equation:

$$\nabla_{x,y} \cdot \varepsilon(x,y)\nabla_{x,y}V_{\mathrm{n}}(x,y) = |e|\rho_{\mathrm{n}}(x,y)/\varepsilon_0, \tag{2.10}$$

where ρ_{n} is the charge density of the ionized dopants. Finally, the electron density n_{e} is calculated as:

$$n_{\mathrm{e}}(x,y) = \frac{1}{\pi\hbar}\sum_{n_i} |\psi_{n_i}(x_i,y_i)|^2 \sqrt{2m^*(x_i,y_i)(E_F-\epsilon_i)}. \tag{2.11}$$

The derivation of the above equation is given in Eq. A.21 in A.

2.4 Numerical Implementation

2.4.1 Numerical Implementation of the Nonlocal Exchange Operator

As discussed in Section 2.3, the coupled expressions in Eqs. 2.6, 2.7, and 2.8 must be solved iteratively until self-consistency is reached. To obtain numerical solutions to these coupled partial differential equations, we use a finite element method to approximate functions at nodal values of a 2-D mesh. When solving the Schrödinger and Poisson equations, we constructed functions (such as m^* and $\left|\psi_{n_j}\right|^2$) that were used as inputs to the built-in MATLAB routines for solving the finite element equations. This results in the constructed functions being approximated as piecewise linear between nodal points, which can result in small integration errors. However, numerical tests by our group have shown that these integration errors are small when sufficiently dense finite element meshes are used to discretize the geometric domain. The finite element procedure in the SHORYUKEN program generates a Delaunay-triangulated grid of points to discretize the geometry and uses a set of "hat" basis functions, ϕ_i, that are linear on each element and take nonzero values only at the x_i node. In other words, all functions and operators in Eq. 2.6, 2.7, and 2.8, are cast to matrices expanded by the basis functions defined on finite element grids, including the Laplacian operator $\nabla_{x_i,y_i} \cdot \varepsilon^*(x_i, y_i)\nabla_{x_i,y_i}$. As such, the matrix representation of the two-dimensional Laplacian operator in Eq. 2.8 can be numerically inverted to obtain the following expression for the nonlocal exchange interaction:

$$\begin{aligned} &V_{\mathrm{EXX},n_j}(x_i, y_i) \\ &= -\frac{1}{\pi\hbar}\left[\nabla_{x_i,y_i} \cdot \varepsilon^*(x_i, y_i)\nabla_{x_i,y_i}\right]^{-1}\left[\frac{e^2}{\varepsilon_0}\sqrt{\frac{m^*(x_i, y_i)(E_F - \epsilon_j)}{2}}\psi^*_{n_j}(x_i, y_i)\psi_{n_i}(x_i, y_i)\right]. \end{aligned} \tag{2.12}$$

The exchange term, $\sum_{n_j} V_{\mathrm{EXX},n_j}(x_i, y_i)\psi_{n_j}(x_i, y_i)$, in Eq. 2.6 can be written as

$$\begin{aligned}\sum_{n_j} V_{\mathrm{EXX},n_j}(x_i, y_i)\psi_{n_j}(x_i, y_i) = -\frac{1}{\pi\hbar}\sum_{n_j}\psi_{n_j}(x_i, y_i)\left[\nabla_{x_i,y_i}\cdot\varepsilon^*(x_i, y_i)\nabla_{x_i,y_i}\right]^{-1}\\ \left[\frac{e^2}{\varepsilon_0}\sqrt{\frac{m^*(x_i, y_i)(E_F-\epsilon_j)}{2}}\psi^*_{n_j}(x_i, y_i)\psi_{n_i}(x_i, y_i)\right].\end{aligned} \tag{2.13}$$

All of the operators in Eq. 2.13 are matrices, and the total exchange interaction, V_{EXX}, can be defined in matrix form [33, 45] as

$$\begin{aligned}V_{\mathrm{EXX}}(x_i, y_i) = -\frac{1}{\pi\hbar}\sum_{n_j}\psi_{n_j}(x_i, y_i)\left[\nabla_{x_i,y_i}\cdot\varepsilon^*(x_i, y_i)\nabla_{x_i,y_i}\right]^{-1}\\ \frac{e^2}{\varepsilon_0}\sqrt{\frac{m^*(x_i, y_i)(E_F-\epsilon_j)}{2}}\psi^*_{n_j}(x_i, y_i).\end{aligned} \tag{2.14}$$

The Schrödinger equation in Eq. 2.6 can now be rewritten as

$$\begin{aligned}\left[-\frac{\hbar^2}{2}\nabla_{x_i,y_i}\cdot\frac{1}{m^*(x_i, y_i)}\nabla_{x_i,y_i}+V_{\mathrm{n}}(x_i, y_i)+V_{\mathrm{CB}}(x_i, y_i)\right]\psi_{n_i}(x_i, y_i)\\ +2\sum_{n_j}V_{\mathrm{D},n_j}(x_i, y_i)\psi_{n_i}(x_i, y_i)-V_{\mathrm{EXX}}(x_i, y_i)\psi_{n_i}(x_i, y_i)=\epsilon_i\psi_{n_i}(x_i, y_i).\end{aligned} \tag{2.15}$$

It is worth noting that the total exchange interaction, V_{EXX}, as written in Eq. 2.15 acts on $\psi_{n_i}(x_i, y_i)$ instead of $\psi_{n_j}(x_i, y_i)$ as in Eq. 2.6. Most importantly, our approach reduces the integro-differential exact-exchange equations to simultaneous (coupled) partial differential equations amenable to a finite element solution *without any nonlocal integral terms.*

2.4.2 Weak Formulation of the Finite Element Equations in the Code

In this section, we present weak formulations of the finite element equations used in the SHORYUKEN code. Given a set of basis functions $\{\phi_q(x, y)\}_{q=1}^{N_p}$ that span the domain

Ω, a weak formulation [46, 47] of the Schrödinger equation given in Eq. 2.6 takes the form:

$$\begin{aligned}\int\limits_\Omega \left(-\nabla \frac{\hbar^2}{2m^*}\cdot\nabla\,\psi_{n_i}\right)\phi_q\,\mathrm{d}x\,\mathrm{d}y + \int\limits_\Omega \left[V_\mathrm{n}+V_\mathrm{CB}+2\sum_{n_j}V_{\mathrm{D},n_j}\right]\psi_{n_i}\,\phi_q\,\mathrm{d}x\,\mathrm{d}y \\ -\sum_{n_j}\int\limits_\Omega V_{\mathrm{EXX},n_j}\,\psi_{n_j}\phi_q\,\mathrm{d}x\,\mathrm{d}y = \int\limits_\Omega \epsilon_i\,\psi_{n_i}\,\phi_q\,\mathrm{d}x\,\mathrm{d}y, \quad q=1,\cdots,N_p,\end{aligned} \tag{2.16}$$

where we have suppressed the dependence on x and y in the functions m^*, ϕ_q, V_n, V_CB, V_EXX, V_{D,n_j}, and ψ_{n_i} for notational simplicity. Similarly, the weak formulations of the Poisson equations in Eqs. 2.7 - 2.8 are given by:

$$\int\limits_\Omega \left(\nabla\varepsilon^*\cdot\nabla V_{\mathrm{D},j}\right)\phi_q\,\mathrm{d}x\,\mathrm{d}y = -\frac{e^2}{\pi\hbar\varepsilon_0}\int\limits_\Omega \sqrt{\frac{m^*(E_F-\epsilon_j)}{2}}\left|\psi_{n_j}\right|^2\phi_q\,\mathrm{d}x\,\mathrm{d}y, \quad q=1,\cdots,N_p, \tag{2.17}$$

$$\int\limits_\Omega \left(\nabla\varepsilon^*\cdot\nabla V_{\mathrm{Exx},n_j}\right)\phi_q\,\mathrm{d}x\,\mathrm{d}y = -\frac{e^2}{\pi\hbar\varepsilon_0}\int\limits_\Omega \sqrt{\frac{m^*(E_F-\epsilon_j)}{2}}\psi^*_{n_j}\psi_{n_i}\phi_q\,\mathrm{d}x\,\mathrm{d}y, \quad q=1,\cdots,N_p. \tag{2.18}$$

Since the set of basis functions, $\{\phi_k(x,y)\}_{k=1}^{N_p}$, span the domain, any scalar function ϑ in the domain can be represented by a linear combination of the basis functions:

$$\vartheta(x,y)=\sum_{k=1}^{N_p}c_k^\vartheta\phi_k(x,y), \tag{2.19}$$

where $\{c_k^{\vartheta}\}$ is a set of scalar coefficients that determine the contribution of each basis function towards the overall form of ϑ. Substituting Eq. 2.19 into the weak formulations given in Eqs. 2.16 - 2.18 and applying Green's first identity (see Appendix D) gives:

$$\begin{aligned}&\sum_{k}^{N_p} c_k^{\psi_i} \int\limits_{\Omega} \frac{\hbar^2}{2m^*} \left(\nabla\phi_k \cdot \nabla\phi_q\right) \mathrm{d}x\,\mathrm{d}y + \sum_{k}^{N_p} c_k^{\psi_i} \int\limits_{\Omega} \left[V_{\mathrm{n}} + V_{\mathrm{CB}} + 2\sum_{n_j} V_{\mathrm{D},n_j}\right] \phi_k\,\phi_q\,\mathrm{d}x\,\mathrm{d}y \\ &\quad -\sum_{n_j}\sum_{k} c_k^{V_{\mathrm{EXX},n_j}} \int\limits_{\Omega} \psi_{n_j}\,\phi_k\,\phi_q\,\mathrm{d}x\,\mathrm{d}y = \epsilon_i \sum_{k}^{N_p} c_k^{\psi_i} \int\limits_{\Omega} \phi_k\,\phi_q\,\mathrm{d}x\,\mathrm{d}y, \quad q = 1, \cdots, N_p,\end{aligned} \tag{2.20}$$

and

$$\begin{aligned}&\sum_{k}^{N_p} c_k^{V_{\mathrm{D},j}} \int\limits_{\Omega} \varepsilon^* \left(\nabla\phi_k \cdot \nabla\phi_q\right) \mathrm{d}x\,\mathrm{d}y \\ =&\frac{e^2}{\pi\hbar\varepsilon_0} \int\limits_{\Omega} \sqrt{\frac{m^*(E_F - \epsilon_j)}{2}} \left|\psi_{n_j}\right|^2 \phi_q\,\mathrm{d}x\,\mathrm{d}y, \quad q = 1, \cdots, N_p,\end{aligned} \tag{2.21}$$

$$\begin{aligned}&\sum_{k}^{N_p} c_k^{V_{\mathrm{EXX},j}} \int\limits_{\Omega} \varepsilon^* \left(\nabla\phi_k \cdot \nabla\phi_q\right) \mathrm{d}x\,\mathrm{d}y \\ =&\frac{e^2}{\pi\hbar\varepsilon_0} \sum_{m}^{N_p} c_m^{\psi_{n_i}} \int\limits_{\Omega} \sqrt{\frac{m^*(E_F - \epsilon_j)}{2}}\, \psi_{n_j}^*\,\phi_m\,\phi_q\,\mathrm{d}x\,\mathrm{d}y, \quad q = 1, \cdots, N_p.\end{aligned} \tag{2.22}$$

We can obtain $c_k^{V_{\mathrm{D},j}}$ and $c_k^{V_{\mathrm{EXX},j}}$ by solving the following two systems of linear equations:

$$\mathbf{L}\,\mathbf{c}^{V_{\mathrm{D},j}} = \mathbf{f}^{n_j}, \tag{2.23}$$

$$\mathbf{L}\,\mathbf{c}^{V_{\mathrm{EXX},j}} = \mathbf{A}^{n_j}\,\mathbf{c}^{\psi_i}, \tag{2.24}$$

where the matrix elements of $\mathbf{L}$, $\mathbf{f}^{n_j}$, and $\mathbf{A}^{n_j}$ are given by:

$$L_{qk} = \int\limits_{\Omega} \varepsilon^* \left(\nabla\phi_k \cdot \nabla\phi_q\right) \mathrm{d}x\,\mathrm{d}y, \tag{2.25}$$

$$f_q^{n_j} = \frac{e^2}{\pi\hbar\varepsilon_0} \int\limits_{\Omega} \sqrt{\frac{m^*(E_F - \epsilon_j)}{2}} \left|\psi_{n_j}\right|^2 \phi_q\,\mathrm{d}x\,\mathrm{d}y, \tag{2.26}$$

$$A_{qm}^{n_j} = \frac{e^2}{\pi\hbar\varepsilon_0} \int\limits_{\Omega} \sqrt{\frac{m^*(E_F - \epsilon_j)}{2}}\,\psi_{n_j}^*\,\phi_m\,\phi_q\,\mathrm{d}x\,\mathrm{d}y. \tag{2.27}$$

Substituting Eq. 2.24 back into Eq. 2.20 yields:

$$\begin{aligned}\sum_{k}^{N_p} c_k^{\psi_i} \int\limits_{\Omega} \frac{\hbar^2}{2m^*} \left(\nabla\phi_k \cdot \nabla\phi_q\right) \mathrm{d}x\,\mathrm{d}y \;+\; \sum_{k}^{N_p} c_k^{\psi_i} \int\limits_{\Omega} \left[V_{\mathrm{n}} + V_{\mathrm{CB}} + 2\sum_{n_j} V_{\mathrm{D},n_j}\right] \phi_k\,\phi_q\,\mathrm{d}x\,\mathrm{d}y \\ -\sum_{n_j}\sum_{k} \int\limits_{\Omega} \left(\mathbf{L}^{-1}\mathbf{A}^{n_j}\mathbf{c}^{\psi_i}\right)_k \psi_{n_j}\,\phi_k\,\phi_q\,\mathrm{d}x\,\mathrm{d}y \;=\; \epsilon_i \sum_{k}^{N_p} c_k^{\psi_i} \int\limits_{\Omega} \phi_k\,\phi_q\,\mathrm{d}x\,\mathrm{d}y, \quad q = 1,\cdots,N_p.\end{aligned} \tag{2.28}$$

We next define the following matrix elements:

$$K_{qk} = \int\limits_{\Omega} \frac{\hbar^2}{2m^*} \left(\nabla\phi_k \cdot \nabla\phi_q\right) \mathrm{d}x\,\mathrm{d}y, \tag{2.29}$$

$$U_{qk} = \int\limits_{\Omega} \left[V_{\mathrm{n}} + V_{\mathrm{CB}} + 2\sum_{n_j} V_{\mathrm{D},n_j}\right] \phi_k\,\phi_q\,\mathrm{d}x\,\mathrm{d}y, \tag{2.30}$$

$$X_{qk}^{n_j} = \int\limits_{\Omega} \psi_{n_j}\, \phi_q\, \phi_k \, \mathrm{d}x\, \mathrm{d}y, \tag{2.31}$$

$$M_{qk} = \int\limits_{\Omega} \phi_q\, \phi_k \, \mathrm{d}x\, \mathrm{d}y, \tag{2.32}$$

which allows the matrix form of Eq. 2.28 to be written as:

$$(\mathbf{K} + \mathbf{U})\, \mathbf{c}^{\psi_i} - \Bigg(\sum_{n_j} \mathbf{X}^{n_j} \mathbf{L}^{-1} \mathbf{A}^{n_j}\Bigg) \mathbf{c}^{\psi_i} = \epsilon_i \mathbf{M} \mathbf{c}^{\psi_i}. \tag{2.33}$$

It is important to note that, unlike a local potential whose matrix form is typically sparse in a finite element basis, the nonlocal exchange term, on the other hand, is generally a dense matrix and requires solving a large system of linear equations. In B, we compare the performance of two different approaches for computing this system of linear equations.

2.4.3 Nanowire Description

While Fig. 2.1 depicts a few GaN/AlGaN core-shell configurations for simplicity, the SHORYUKEN program can be easily configured to compute nonlocal exchange effects for core-multishell nanowires with arbitrary cross-sections and material compositions. For the specific examples in this work, we take the electronic properties of the core and shell to be those of their respective bulk systems. Specifically, the bandgap, electron affinity, dielectric constant and effective mass for $\mathrm{Al}_x\mathrm{Ga}_{1-x}\mathrm{N}$ are given by the relations: $E_g(x) = [3.42 + 2.86x - x(1-x)]$ eV, $\chi = [5.88 - 0.7E_g(x)]$ eV, $\varepsilon^*(x) = 9.28 - 0.61x$, and $m^*(x) = (0.2 - 0.12x)m_0$ respectively, where m_0 is the electron rest mass. Setting x to 0 and 0.3 gives rise to a conduction band discontinuity of $\Delta E_c = 0.5$ eV at the core-shell interface, which is used in this paper and shown in Fig. 2.1(a). In addition, the polarization, $\mathbf{P}(\mathbf{r})$, consists of two sources: (1) spontaneous polarization $\mathbf{P}^{\mathrm{sp}}$ due to the difference in electronegativity between GaN/AlGaN; and (2) piezoelectric polarization $\mathbf{P}^{\mathrm{pz}}$ due to the lattice constant mismatch when AlGaN is grown on the GaN layer [48]. The spontaneous polarization is along the [0001] direction and can be written as $\mathbf{P}^{\mathrm{sp}} = P^{\mathrm{sp}}\hat{\mathbf{z}}'$, where $\hat{\mathbf{z}}'$ is a unit vector along the [0001] direction. Specifically, the spontaneous polarization for $\mathrm{Al}_x\mathrm{Ga}_{1-x}\mathrm{N}$ is given by $P^{\mathrm{sp}}_{\mathrm{Al}_x\mathrm{Ga}_{1-x}\mathrm{N}} = (1-x)P^{\mathrm{sp}}_{\mathrm{GaN}} + xP^{\mathrm{sp}}_{\mathrm{AlN}}$ with $P^{\mathrm{sp}}_{\mathrm{GaN}} = -0.029\ C/\mathrm{m}^2$ and $P^{\mathrm{sp}}_{\mathrm{AlN}} = -0.081\ C/\mathrm{m}^2$ [49, 50]. From electrostatics, the surface charge due to the spontaneous polarization at the GaN/$\mathrm{Al}_{0.3}\mathrm{Ga}_{0.7}\mathrm{N}$ interface is $\sigma^{\mathrm{sp}} = -\nabla \cdot \mathbf{P}^{\mathrm{sp}} = \left(P^{\mathrm{sp}}_{\mathrm{GaN}} - P^{\mathrm{sp}}_{\mathrm{Al}_{0.3}\mathrm{Ga}_{0.7}\mathrm{N}}\right)\cos\theta = 0.0156\cos\theta\ \mathrm{C/m^2}$ where θ is the angle of the interface relative to the [0001] direction. The piezoelectric polarization at the interface is given by $\mathbf{P}^{\mathrm{pz}} = [e_{15}\varepsilon_{xz}, e_{15}\varepsilon_{yz}, e_{31}(\varepsilon_{xx} + \varepsilon_{yy}) + e_{33}\varepsilon_{zz}]^{\mathrm{T}}$ where e_{ij} is the piezoelectric tensor and ε_{ij} is the strain tensor [50]. The surface charge density due to the piezoelectric polarization can then be computed from $\sigma^{\mathrm{pz}} = -\nabla \cdot \mathbf{P}^{\mathrm{pz}}$. In addition, prior studies have shown that the strain gradients in the shell are negligible compared to those near the interface [50], and the effects of strain on bandgaps and effective masses are small and can be ignored [19, 30, 51]. In the presence of the polarization surface charges ($\sigma = \sigma^{\mathrm{sp}} + \sigma^{\mathrm{pz}}$), the corresponding electrostatic potential energy V_{P} must be added to the Schrödinger equation in Eq. 2.1 and computed by the expression

$$\nabla_{x,y} \cdot \varepsilon^*(x,y)\nabla_{x,y}V_{\mathrm{P}}(x,y) = |e|\sigma(x,y)/\varepsilon_0. \tag{2.34}$$

The coupled expressions in Eqs. 2.7, 2.8, 2.10, 2.15, and 2.34, are solved with Dirichlet boundary conditions such that the solutions vanish at all boundaries. In contrast to our previous study in Ref. [30], we set the zero of the potential at the outer-shell boundary in this work.

2.4.4 Workflow of the SHORYUKEN Code

In this section, we briefly describe the various functions in the SHORYUKEN code, excluding portions that have not been altered from the original HADOKEN code. We point the reader to the HADOKEN paper [30] for further details on the algorithms that were left unmodified. To run the SHORYUKEN code, a user needs to inspect the `input_parameters.m` m-file, which contains parameters governing the shape of the nanowire cross-section, the size of each layer, doping density, bandgap alignment, surface donor model parameters (see Section 2.5.2), toggling of the exchange-potential, and material composition. The SHORYUKEN code is then executed by calling the `main.m` function with the desired `input_parameters.m` file as an input. The geometry will be discretized as specified in the parameter file using the `generate_mesh.m` function. The `generate_mesh.m` routine makes use of a symmetric mesh generation, which avoids the necessity to spatially symmetrize the electron density, an approach used in our previous work [30]. The symmetric mesh generation first constructs a mesh of the most compact sub-symmetric section of the polygon and uses a series of reflections and rotations to create a full mesh, as shown in Fig. 2.2.

With all of these pre-processing steps completed, the program executes `initiate_system.m` to initialize the system by solving the Schrödinger equation with a seed potential to find wavefunctions, from which the Fermi level and electrostatic potential energy are calculated. Specifically, the seed potential is set as the bare conduction band edge profile,

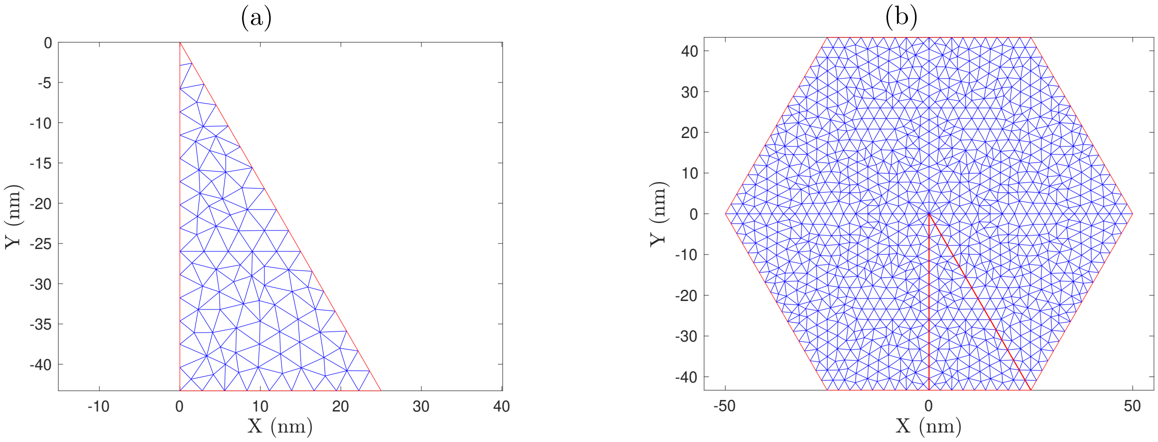

Figure 2.2: (a) Mesh grids generated by the `initmesh` function on one of the symmetrically-equivalent triangles that comprise a hexagon. (b) Mesh grids on the entire hexagon domain obtained by reflecting grids in panel (a) along each symmetry axis.

V_{CB}, for the hexagonal geometry, which is provided in the `V_conduction_band.m` m-file. For the triangular nanowires, the potential energy, V_{P}, due to the spontaneous and piezoelectric polarization is also considered and computed according to Eq. 2.34. The seed potential is thus the sum of the conduction band profile and polarization potential, V_{P}. With the seed potential properly calculated, the Schrödinger equation can be solved to find the eigenstates of the system. At the same time, the Fermi level E_F is determined such that the charge neutrality condition in Eq. 2.11 is satisfied, which is implemented in the `find_epsilon_F.m` file. All computed wavefunctions with energies less than E_F are designated as occupied states, which are used to compute the Coulombic potential energy, V_{D}, as obtained from Eq. 2.7. The potential energy, V_{D}, is used as input for the next iteration.

The `iterate_run.m` m-file carries out the calculations successively until self-consistency is achieved. In each iteration, the program takes the updated potential energy from the previous iteration as input and solves coupled Schrödinger-Poisson equations. When the nonlocal exchange option is enabled in the input file, the nonlocal exchange operator is computed in `assem_pde.m` with Eq. 2.14. The matrix $\mathbf{L}$ in Eq. 2.25 is outputted when the "`c`" coefficient in the `assema` function in the MATLAB PDE toolbox [52] is set to the spatially varying dielectric constant $\epsilon^*(x, y)$. Similarly, the matrix $\mathbf{M}$ in Eq. 2.32 is given by the outputted mass matrix from `assema` when the "`a`" coefficient is set to one. This same methodology can be used for all the other coefficients to obtain the full set of matrices required to solve all of the linear systems in the SHORYUKEN code. The exchange Hamiltonian can be assembled by the multiplication of these matrices according to Eq. 2.14. Eq. 2.15 (including the exchange interaction) can then be solved using the MATLAB `sptarn` sparse eigenvalue solver. The Fermi and electrostatic energy are then recomputed as described previously.

After each iteration, the potential is updated using the following formula:

$$V_{\text{poiss\_updated}} = V_{\text{poiss\_old}} + \texttt{damping\_factor} \times (V_{\text{poiss}} - V_{\text{poiss\_old}}).$$

The $V_{\text{poiss\_old}}$ and V_{poiss} terms are the potentials obtained during the previous and current iteration, respectively. The `damping_factor` coefficient is the learning rate of the algorithm and typically ranges from 0.08 to 0.02. To allow the potential to converge without significant oscillations, the learning rate decreases linearly with the number of iterations. In contrast to our previous HADOKEN code [30], the SHORYUKEN code uses more stringent requirements for convergence. Specifically, the SHORYUKEN code designates an iteration to be "successful" if the previous and current iteration satisfies the following criteria: (1) the number of occupied states should be equal, (2) the average potential energy difference is less than 0.01 eV: `average`$(|V_{\text{poiss}} - V_{\text{poiss\_old}}|) < 0.01$ eV, and (3) the ratio of the average potential energy difference to the average potential energy is less than 0.1: `average`$(|V_{\text{poiss}} - V_{\text{poiss\_old}}|)$/`average`$(|V_{\text{poiss}}|) < 0.1$. We find that requirement 3 is more impactful for smaller systems (with fewer electrons) since these configurations readily meet requirement 2. In contrast, larger systems tend to be more restricted by the second requirement. The SHORYUKEN program considers the entire calculation to be converged and terminates the loop when three successful iterations are obtained in a row. Upon convergence, all of the results are saved in a `.mat` file, and figures of the wavefunctions, eigenvalues, Fermi level, number of occupied states, and potential energy are plotted. Additional quantities/results can be post-processed from the saved `.mat` file.

2.5 Results and Discussions

2.5.1 Hexagonal Nanowire

Since the axis of the hexagonal GaN/AlGaN nanowire is along the spontaneous polarization direction (cf. Fig. 2.1(a)), the surface charge is zero at the interface of the cross-section. In addition, the piezoelectric polarization does not contribute to the surface charge since the polarization field is orthogonal to the direction of the interface plane [48]. To understand the effects of nonlocal exchange, Fig. 2.3 compares the electron occupancy of several hexagonal GaN/AlGaN nanowires with and without nonlocal exchange. The plotted results are for nanowires with core side lengths of 30, 40, and 50 nm, and doping densities, n_{D}, ranging from 0.02 to 1.2×10^{18} cm^{-3}. In all of these calculations, the width of the shell region t was fixed at $10\sqrt{3}$ nm. As can be seen in Fig. 2.3, the omission of the

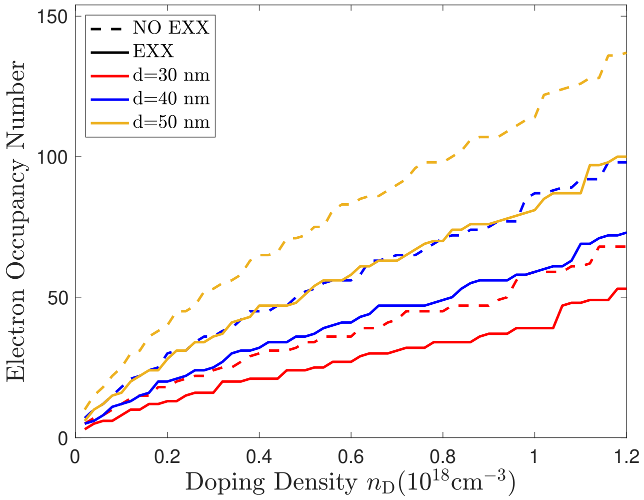

Figure 2.3: Electron occupancy number in hexagonal GaN/AlGaN nanowires with different core side lengths denoted by different colors, as a function of the doping density n_{D}. The solid lines represent results with nonlocal exchange, whereas dashed lines indicate calculations using the conventional Schrödinger-Poisson treatment without exchange.

exchange term leads to a substantial overestimation of the number of occupied states. This discrepancy increases with larger core sizes and higher doping densities, which is anticipated since exchange effects become more pronounced in systems with more electrons and many-body interactions.

Fig. 2.4 depicts the eigenvalues of the first several occupied electronic states as a function of doping density for systems with and without nonlocal exchange. As seen in Fig. 2.4, the inclusion of nonlocal exchange in the calculations typically produces more negative (i.e., energetically lower) energy eigenvalues. This is due to the antisymmetry requirement arising from the exchange interaction that prohibits two electrons with identical spins from occupying the same spatial orbital, which diminishes the Coulombic repulsion between electrons. This concept is underscored by the positive expectation value of the nonlocal exchange operator $\langle \Psi_i(\mathbf{r}_i)|\hat{V}_{\mathrm{EXX},j}(\mathbf{r}_i)|\Psi_i(\mathbf{r}_i)\rangle$ [43]. Consequently, the total energy is lowered

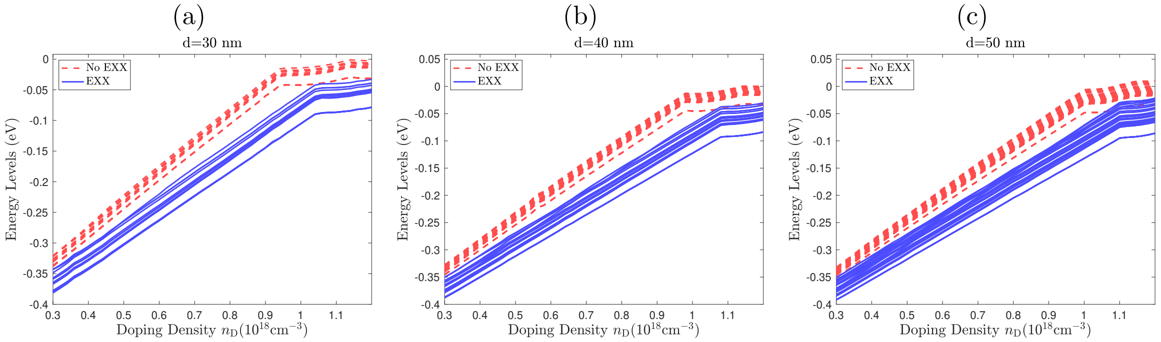

Figure 2.4: Energies of the first 16, 24, and 36 occupied states as a function of doping density with core side lengths of (a) 30, (b) 40, and (c) 50 nm. Results with nonlocal exchange are denoted by solid blue lines, whereas calculations using the conventional Schrödinger-Poisson treatment without exchange are shown in dashed red lines. All plots were generated for hexagonal GaN/AlGaN nanowires with a shell thickness of $t = 10\sqrt{3}$ nm.

as delineated in Eq. 2.1. In addition, Fig. 2.4 shows that the spacing between adjacent energy eigenvalues widens upon inclusion of nonlocal exchange, in line with previous work [33, 25]. These increased energy gaps can account for the reduced number of occupied states shown in Fig. 2.3. Given the charge neutrality condition in Eq. 2.9, the electron number remains consistent with or without exchange. From the electron density expression in Eq. 2.11, $n_{\mathrm{e}}(x,y) \propto \sum_{n_i} \sqrt{(E_F - \epsilon_i)}$, larger energy gaps indicate greater values for $\sqrt{(E_F - \epsilon_i)}$, resulting in fewer summation terms or occupied states required to maintain charge neutrality. The energy eigenvalues increase linearly with doping density until an inflection point is reached around $n_{\mathrm{D}} = 1.0 \times 10^{18}$ cm^{-3}. Beyond this threshold, the increase in eigenvalues saturates, which can be attributed to electron tunneling into the shell layer, which we discuss later.

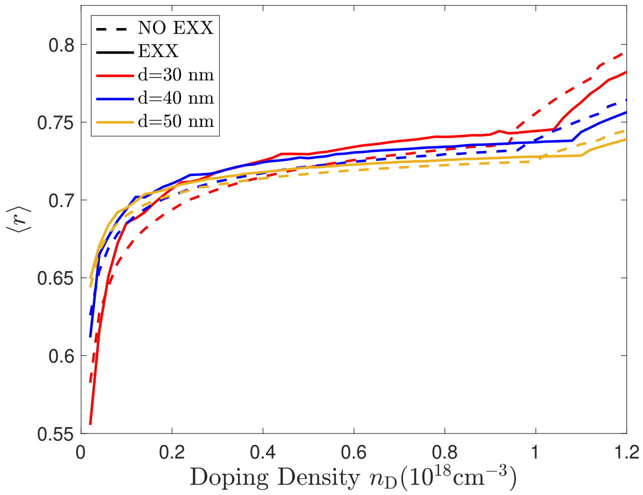

Figure 2.5: Normalized mean distance of the electron distribution in hexagonal GaN/AlGaN nanowires as a function of doping density, n_{D}. The different core side lengths are denoted by different colors; solid lines represent results with nonlocal exchange, whereas dashed lines indicate calculations using the conventional Schrödinger-Poisson treatment without exchange.

Next, we examined the spatial distribution of the electron gas by introducing a core-normalized average distance:

$$\langle r \rangle = \frac{\int \mathrm{d}x\mathrm{d}y \; \sqrt{x^2+y^2} n_{\mathrm{e}}(x,y)}{c \cdot \int \mathrm{d}x\mathrm{d}y \; n_{\mathrm{e}}(x,y)}. \tag{2.35}$$

By construction, $\langle r \rangle$ represents the average displacement of the electron density from the nanowire center and is bounded between 0 and s/c. Fig. 2.5 plots $\langle r \rangle$ as a function of doping density, n_{D}, for systems with and without nonlocal exchange. Three distinct regimes are shown in Fig. 2.5: At low doping densities ($n_{\mathrm{D}} < 0.2 \times 10^{18}$ cm^{-3}), $\langle r \rangle$ rises rapidly with n_{D}, as stronger Coulombic repulsion causes electrons to congregate at the core-shell interface. For intermediate doping densities (0.2×10^{18} cm^{-3} $< n_{\mathrm{D}} < 1 \times 10^{18}$ cm^{-3}), $\langle r \rangle$ remains relatively stable. In this region, the majority of electrons are localized at the interface, and

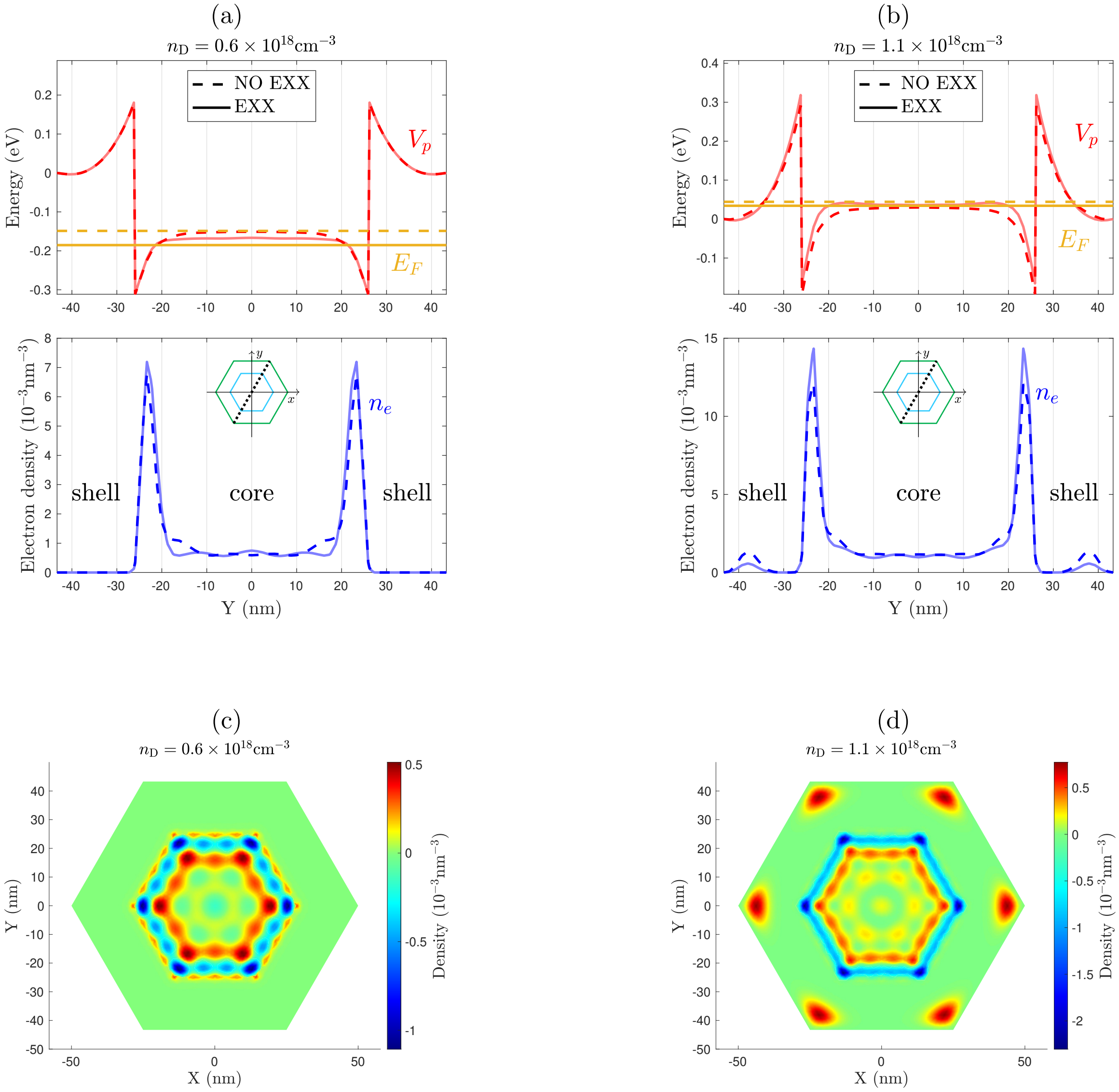

Figure 2.6: (upper panels) Potential energy (red lines) and Fermi level (orange lines); (lower panels) electron density (blue lines) for a hexagonal GaN/AlGaN nanowire with core side length $c = 30$ nm and shell thickness $t = 10\sqrt{3}$ nm with a doping density of (a) 0.6×10^{18} cm^{-3} and (b) 1.1×10^{18} cm^{-3}. Results with nonlocal exchange are denoted by solid lines, whereas calculations using the conventional Schrödinger-Poisson treatment without exchange are shown in dashed lines. The potential energy and electron density were calculated along the dashed line across the diagonal of the hexagon nanowire diagram in the inset. The corresponding electron density differences, $n_{e,\text{ no EXX}} - n_{e,\text{ EXX}}$, are shown in panels (c) and (d), respectively.

further doping simply results in additional confined states around the interface. At high doping densities ($n_{\mathrm{D}} > 1 \times 10^{18}$ cm^{-3}), $\langle r \rangle$ begins to rise once again. Here, the potential energy of the shell drops below the Fermi level, and electrons begin tunneling out of the core into the shell region. This bending of the potential energy surface can be seen in Figs. 2.6(a) and (b), which depicts the potential energy, electron density, and Fermi level for nanowires with doping densities of 0.6×10^{18} and 1.1×10^{18} cm^{-3}. As the doping density increases, the potential energy (indicated by the red line) bends more acutely in the shell, causing the electron distribution (blue line) to peak near the interface and eventually penetrate the shell in the high-doping regime.

Fig. 2.5 shows that the conventional Schrödinger-Poisson treatment predicts $\langle r \rangle$ to be generally smaller compared to the nonlocal exchange calculation at lower doping densities ($n_{\mathrm{D}} < 1 \times 10^{18}$ cm^{-3}); conversely, $\langle r \rangle$ is larger in the higher doping regime ($n_{\mathrm{D}} > 1 \times 10^{18}$ cm^{-3}). As previously mentioned, systems without nonlocal exchange exhibit a reduced one-dimensional density of states along the z-axis for a given eigenstate ψ_{n_i} (cf. Eq. 2.11). This results in a greater occupancy in higher-energy wavefunctions, predominantly manifesting on the shell at high doping densities (e.g., $n_{\mathrm{D}} = 1.1 \times 10^{18}$ cm^{-3}), which yields a broader average distance. However, in the lower doping regime (e.g., $n_{\mathrm{D}} = 0.6 \times 10^{18}$ cm^{-3}), in the absence of tunneling effects, electrons initially populate lower-energy states near the interface before progressively occupying states closer to the center of the core. Consequently, the absence of nonlocal exchange causes electrons to be more centrally concentrated, resulting in a smaller $\langle r \rangle$. To better visualize these disparities, Figs. 2.6(c) and (d) show electron density differences, $n_{e,\text{ no EXX}} - n_{e,\text{ EXX}}$, between systems with and without exchange at low ($n_{\mathrm{D}} = 0.6 \times 10^{18}$ cm^{-3}) and high doping ($n_{\mathrm{D}} = 1.1 \times 10^{18}$ cm^{-3}). By construction, red-colored (positively valued) regions denote areas that the conventional Schrödinger-Poisson treatment predicts to have a higher electron density than the nonlocal exchange calculation; conversely, blue-colored (negatively valued) regions represent areas that the nonlocal exchange calculation predicts to have a higher electron density than the Schrödinger-Poisson treatment. At low doping densities, Fig. 2.6(c) shows that the conventional Schrödinger-Poisson treatment predicts a more delocalized electron density throughout the core region compared to the nonlocal exchange calculation. At higher doping densities, Fig. 2.6(d) shows a more dramatic delocalization pattern with the Schrödinger-Poisson treatment predicting more electron density tunneling into the shell region compared to the nonlocal exchange formalism. Regardless of doping density, the nonlocal exchange calculations consistently predict the electron density to be more localized near the core-shell interface in both Figs. 2.6(c) and (d).

An example of the `input_parameters.m` MATLAB code settings for calculating nonlocal exchange in a hexagonal GaN/AlGaN nanowire to plot Fig. 2.6c is given below:

```
include_ex = true;
degree_of_polygon = 6;
n_D = 0.6;
vector_of_side_lengths = [5 3];
vector_of_V0 = [0.5 0.0];
vector_of_masses = [0.2-0.12*0.3 0.2];
vector_of_eps = [9.28-0.61*0.3 9.28];
number_of_triangles = 10000;
```

The variables specific to the hexagonal GaN/AlGaN nanowire are described below:

- `include_ex`: indicates whether nonlocal exchange is included

- `degree_of_polygon`: sets the shape of nanowire cross-section: 6 produces a hexagon, 3 (-3) gives a Ga-face (N-face) triangular system.
- `n_D`: doping density in units of 10^{18} cm^{-3}
- `vector_of_side_lengths`: vector of side lengths of each layer going inward in units of 10 nm
- `vector_of_V0`: band-edge energy for each layer in units of eV
- `vector_of_masses`: effective mass of electrons in each layer in units of the electron rest mass m_0
- `vector_of_eps`: dielectric constant in each layer
- `number_of_triangles`: number of elements in the finite element discretization

2.5.2 Triangular GaN/AlGaN Nanowires

For GaN/AlGaN core-shell nanowires with triangular cross-sections, both spontaneous and piezoelectric polarization contributions must be considered. Furthermore, as shown in Fig. 2.1(d), the triangular cross sections can have two orientations: (1) in the Ga-face orientation, the polarization creates positive charges at the (0001) interface and negative charges at the other two semipolar planes; (2) in contrast, the N-face system has negative charges at the $(000\bar{1})$ interface and positive charges at the other two faces. More interestingly, it has been observed that a high-mobility two-dimensional electron gas is present at the (0001) interface even in the absence of doping for nitride heterostructures grown in the [0001] orientation [49, 53, 54]. The most commonly accepted mechanism to explain the origin of the 2DEG is the single-energy surface donor model [54]. This model assumes that a high density of surface donor states exists at a certain energy level at the AlGaN surface and can donate electrons to the core once the shell thickness, t, reaches a critical value, t_{cr}, resulting in the fixed Fermi level. Later studies have found that the Fermi level increases with increasing t [55], due to a low density of surface states, n_0, distributed over a range of energies below a particular energy level, E_{cr} [13, 55].

Ga-face Triangular Nanowire and Improved Surface-State Model

The surface donor model for the Ga-face nanowire uses two parameters: the surface state density, n_0, and a critical energy level, E_{cr}, below which surface donor states exist. Generally, n_0 can be a function of the energy; for simplicity, we assume that surface states are uniformly distributed so that n_0 is a constant. For the Ga-face configuration, we set the doping density to zero ($n_{\text{D}} = 0$) such that the 2DEG comes entirely from the surface donors. In this case, when applying the charge neutral requirement in Eq. 2.9, the positive charges are the emptied donors at the shell surface, and the total number is computed as $\int_{E_F}^{E_{\text{cr}}} n_0 \mathrm{d}E = n_0(E_{\text{cr}} - E_F)$. Our findings are illustrated in Fig. 2.7, which depicts both the electron occupancy number and energy eigenvalues of the first 15 eigenstates as functions of the shell thickness, t. As previously discussed in Section 2.5.1 for the hexagonal Gan/AlGaN nanowire, we observe similar trends: the conventional Schrödinger-Poisson treatment overestimates the number of occupied electron levels and energy eigenvalues but underestimates the energy spacings. Fig. 2.8 depicts the total electron density distribution for a Ga-face triangular nanowire with nonlocal exchange and the electron density differences, $n_{e,\text{ no EXX}} - n_{e,\text{ EXX}}$, between results with and without exchange. Fig. 2.8(a) shows

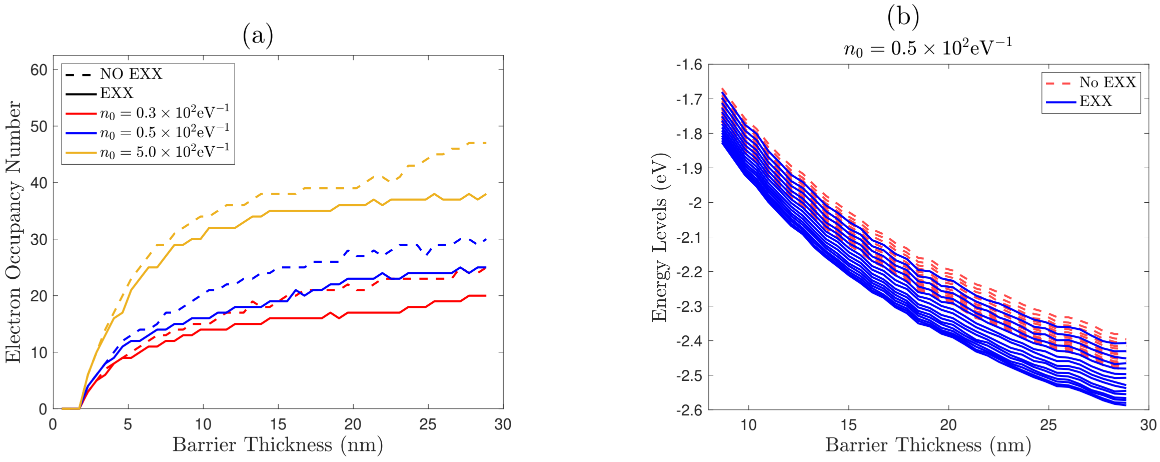

Figure 2.7: (a) Electron occupancy number for different densities of surface states n_0 and (b) calculated energies of the first 15 occupied states at $n_0 = 0.5 \times 10^2$ eV^{-1}, as a function of the shell thickness t. All plots are for the Ga-face orientation with zero doping density and the critical energy level, E_{cr}, set to -1 eV. The solid lines represent results with nonlocal exchange, whereas dashed lines indicate calculations using the conventional Schrödinger-Poisson treatment without exchange.

that electrons distribute similarly to a 2DEG in a bulk heterojunction and are attracted by the positive polarization surface charges at the interface. The first few wavefunctions resemble one-dimensional particle-in-a-box eigenstates with higher-energy states having more nodes and delocalization. As a result, calculations with nonlocal exchange have a more localized electron distribution since they have fewer occupied states (cf. Fig. 2.7(a)). The electron density difference plotted in Fig. 2.8(b) shows that calculations with nonlocal exchange result in electrons being more localized near the interface.

Fig. 2.9 plots surface barrier heights and 2DEG numbers for various n_0 as a function of the shell thickness t. The surface barrier height is defined as the energy difference between the Fermi level and the conduction-band minimum of the AlGaN shell [56]. Since

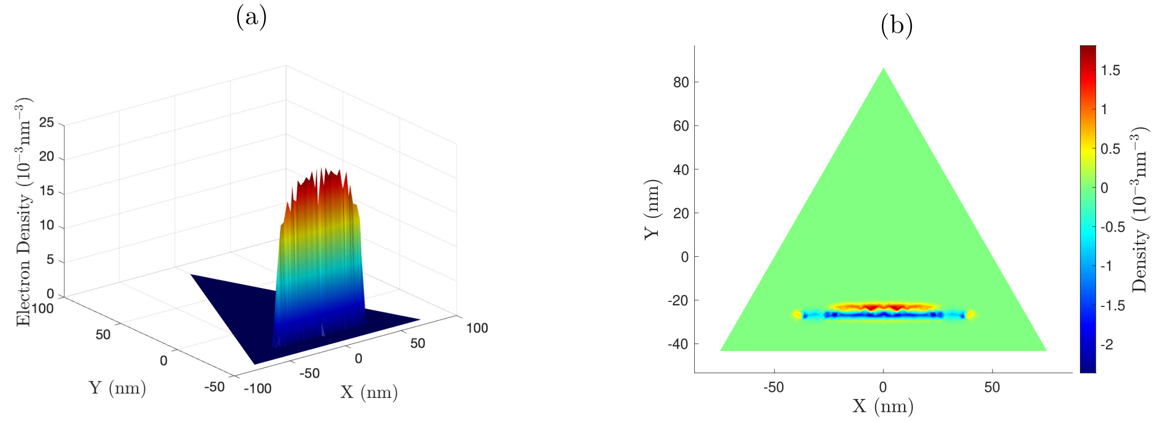

Figure 2.8: (a) 2DEG distribution at the interface for a Ga-face triangular nanowire with core side length c = 100 nm and shell side length s = 150 nm with $n_0 = 0.5 \times 10^2$ eV^{-1} and (b) Electron density difference, $n_{e,\text{ no EXX}} - n_{e,\text{ EXX}}$, for the same nanowire in (a) with nonlocal exchange. All plots have a zero doping density with the critical energy level, E_{cr}, set to -1 eV.

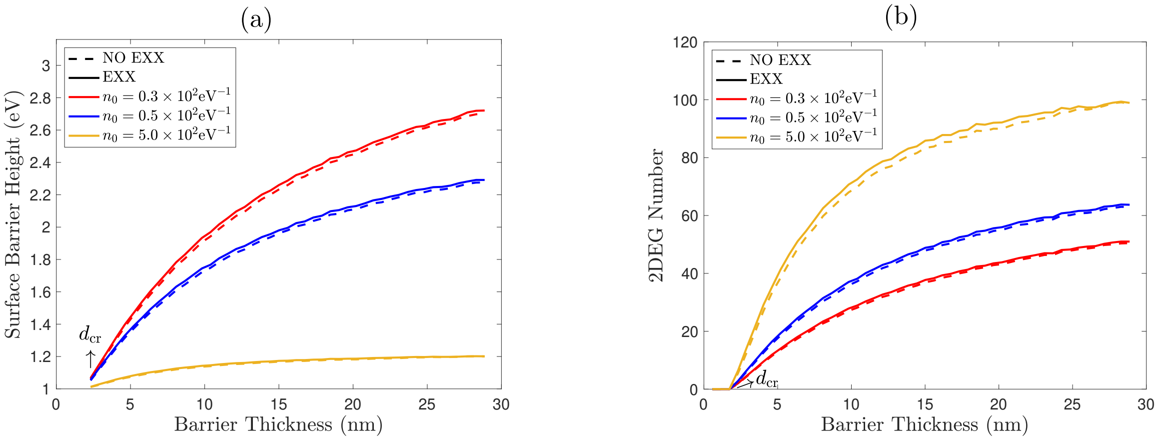

Figure 2.9: (a) Surface barrier heights and (b) 2DEG numbers as a function of AlGaN barrier thickness for different surface state densities, n_0. The solid lines represent results with nonlocal exchange, whereas dashed lines indicate calculations using the conventional Schrödinger-Poisson treatment without exchange. All plots are for the Ga-face orientation with zero doping density with the critical energy level, E_{cr}, set to -1 eV.

the edge of the outer shell is set as the zero reference potential, the surface barrier height is the numeric value of the Fermi level. Fig. 2.9(a) shows that the surface barrier height increases with the barrier thickness, t, at low surface state densities (blue and red lines) once t reaches the critical thickness, t_{cr}. When $t < t_{\mathrm{cr}}$, the critical energy level, E_{cr} (which is set to -1 eV in this work), is lower than the minimum potential energy, and, therefore, no electrons are donated. When t increases, the potential energy of the interface decreases (since the shell has a constant electric field), eventually crossing E_{cr}. At that moment, electrons start transferring from surface donors to the core, forming a 2DEG to mitigate the electric field or decelerate the decrease in the potential energy. Nevertheless, at lower surface state densities, there are not enough donated electrons to fully counterbalance the potential energy reduction as t grows, leading to a rising surface barrier height. Conversely, with higher surface state densities (depicted by the yellow line), there is a continuous transfer of electrons to the core until all states beneath the Fermi level are occupied, resulting in a relatively stable or constant Fermi level, irrespective of barrier thickness. Fig. 2.9(b) plots 2DEG numbers as a function of the barrier thickness, which clearly shows the critical shell thickness, t_{cr}, below which the 2DEG number vanishes.

An example of the `input_parameters.m` MATLAB code settings for calculating nonlocal exchange in a Ga-face triangular nanowire to plot Fig. 2.8a is given below:

```
include_ex = true;
degree_of_polygon = 3;
n_D = 0;
vector_of_side_lengths = [15 10];
vector_of_V0 = [0.5 0.0];
vector_of_masses = [0.2-0.12*0.3 0.2];
vector_of_eps = [9.28-0.61*0.3 9.28];
dos = 50 / (exp((x+1)*10000 ) + 1);
pol_spont = [-0.0446, -0.029];
```

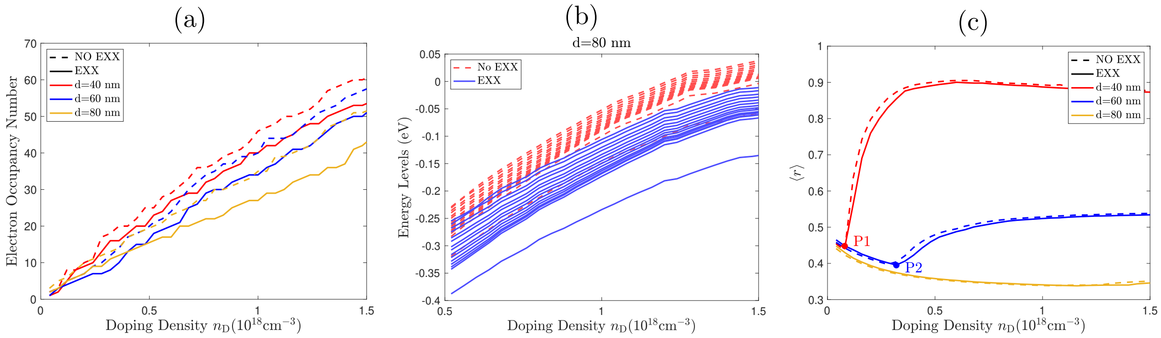

Figure 2.10: (a) Electron occupancy number, (b) calculated energies of the first 15 occupied states, and (c) normalized average distance $\langle r\rangle$ as a function of doping density, n_D. The solid lines represent results with nonlocal exchange, whereas dashed lines indicate calculations using the conventional Schrödinger-Poisson treatment without exchange. All plots are for N-face GaN/AlGaN triangular nanowires with a shell side length, s set to 110 nm.

```
pol_piezo = ["piezo_analytic"];
number_of_triangles = 5000;
```

The variables specific to the Ga-face triangular GaN/AlGaN nanowire are described below:

- `dos`: surface state density n_0, in units of eV^{-1}
- `pol_spont`: spontaneous polarization P^{sp} in each layer, in units of C/m^2
- `pol_piezo`: piezoelectric polarization P^{pz} at the interface, in units of C/m^2

N-face Triangular Nanowire

Figs. 2.10(a) and (b) plot the electron occupancy number and energy eigenvalues, respectively, for various N-face nanowire sizes as a function of doping density (the shell side length, s, is kept constant at 110 nm for all of the calculations). As observed previously, including nonlocal exchange results in reduced occupancy numbers and lower energy values,

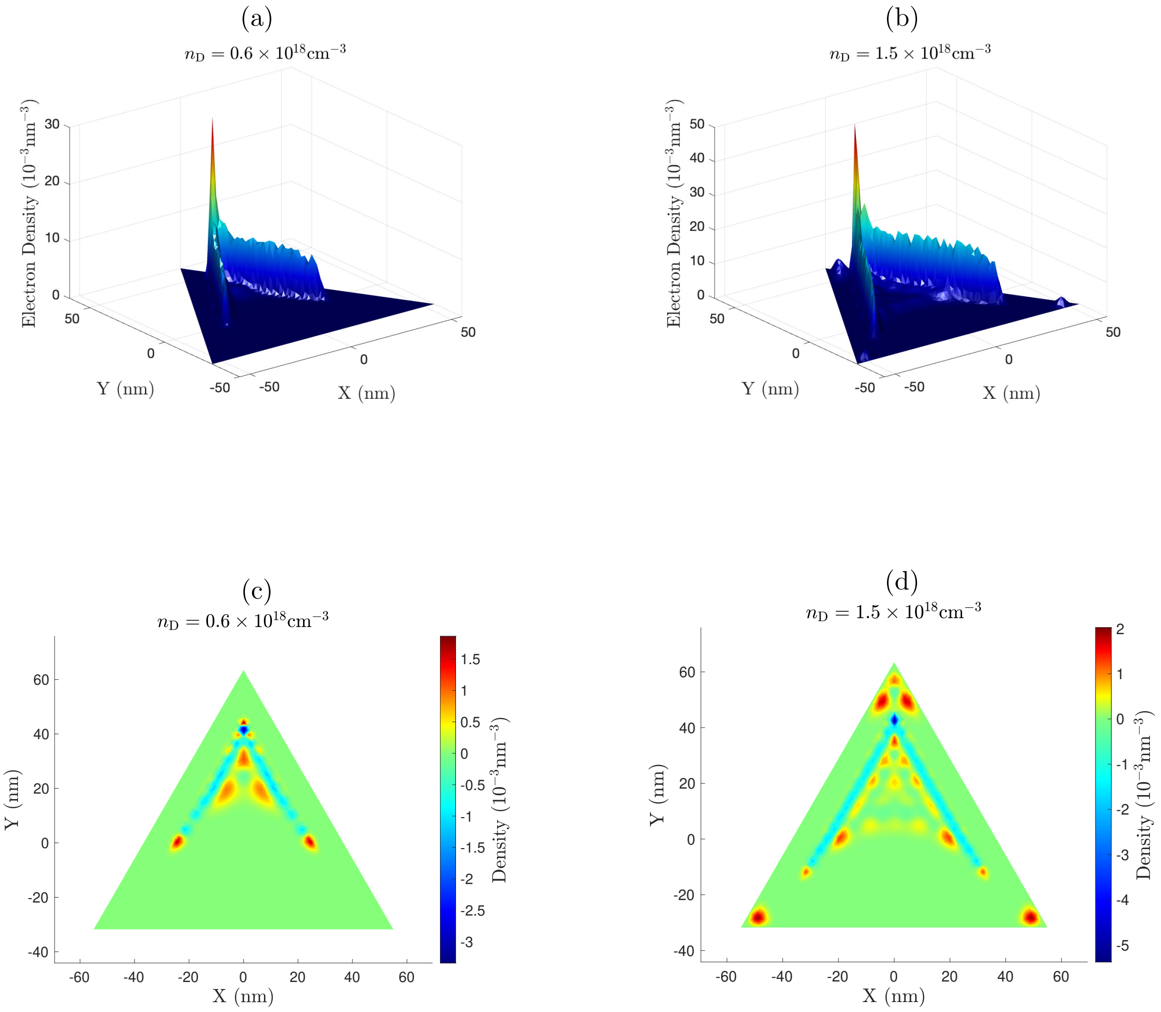

Figure 2.11: 2DEG distributions for an N-face triangular GaN/AlGaN nanowire including nonlocal exchange with (a) $n_{\mathrm{D}} = 0.6 \times 10^{18}$ cm^{-3} and (b) $n_{\mathrm{D}} = 1.5 \times 10^{18}$ cm^{-3}. The core and shell side lengths used in both panels are 80 and 110 nm, respectively. Panels (c) and (d) show electron density differences, $n_{e,\text{ no EXX}} - n_{e,\text{ EXX}}$, for the corresponding nanowires in panels (a) and (b).

but with expanded energy gaps, as described in Section 2.5.1. Fig. 2.10(c) plots the normalized average distance $\langle r \rangle$ as a function of doping density for nanowires with various core sizes. Notably, the value of $\langle r \rangle$ increases abruptly for the 40 and 60 nm systems near the points labeled P1 and P2. This rapid increase can be attributed to the tunneling of electrons from the inner core region into the outer shell. Furthermore, configurations with smaller core dimensions show increased tunneling effects at lower doping densities. This behavior can be attributed to the localization of electrons around the upper corner of the core region, as illustrated in Figs. 2.11(a) and (b). In nanowires with smaller core sizes, localization of the polarization-induced surface charges results in higher repulsive forces on the 2DEG. As a result, the electrons in these small-core nanowires more readily tunnel into the shell regions. In other words, nanowires with constrained dimensions exhibit larger energy gaps between their eigenenergies; to minimize this energetically unfavorable situation, electrons in these small-core nanowires will populate the outer shell. Figs. 2.11(c) and (d) plot the difference in electron distributions for systems with and without nonlocal exchange. These differences reveal a pronounced electron concentration along the two semi-polar interfaces in systems with nonlocal exchange, as highlighted by the blue-colored regions. This localization trend aligns with the observations made for hexagonal nanowires in Section 2.5.1 and for Ga-face triangular nanowires in Section 2.5.2.

An example of the `input_parameters.m` MATLAB code settings for calculating nonlocal exchange in an N-face triangular nanowire to plot Fig. 2.11a is given below:

```
include_ex = true;
degree_of_polygon = -3;
n_D = 0.6;
vector_of_side_lengths = [11 8];
vector_of_V0 = [0.5 0.0];
```

```
vector_of_masses = [0.2-0.12*0.3 0.2];
vector_of_eps = [9.28-0.61*0.3 9.28];
pol_spont = [-0.0446, -0.029];
pol_piezo = ["piezo_analytic"];
number_of_triangles = 5000;
```

2.6 Conclusions

In this contribution, we have constructed and documented the open-source SHORYUKEN software package for the efficient calculation of nonlocal exchange in heterostructure core-shell nanowires with arbitrary cross-sections. The SHORYUKEN code is written in the high-level MATLAB programming environment for enhanced readability/accessibility to solve the coupled nonlocal exchange equations on a flexible finite element grid. In addition to enabling new calculations of nonlocal exchange, the SHORYUKEN software package includes new algorithmic improvements in addition to an improved treatment of surface states for nanowires with intrinsic polarization. The capabilities of the SHORYUKEN software package can be used by both experimentalists and theorists to explore the effects of bandgap alignment, material composition, cross-sectional geometry, doping density, and many-body nonlocal exchange on electron gas formation in these nanowire systems.

Using the SHORYUKEN code, we find that the inclusion of nonlocal exchange has a crucial effect on the localization of electrons in GaN/AlGaN core/shell nanowires, with more pronounced effects in the hexagonal geometry, which does not have a net intrinsic polarization. Nevertheless, for all the nanowire geometries examined in this work, we find that the inclusion of nonlocal exchange leads to much larger energy separations between electronic subbands compared to the conventional Schrödinger-Poisson treatment. Looking forward, we anticipate that the SHORYUKEN software package could be used in a variety of other applications that require a higher-level treatment of electronic properties in these nanoscale systems. For example, electronic structure calculations with nonlocal exchange are usually the initial reference state for higher-level treatments of electron correlation. Consequently, the formalism used in this work serves as a starting point for more complex treatments of strong correlation effects in nanowires. Similarly, since electron/hole energies for predicting optical properties are sensitive to the energy separation between electronic subbands, nonlocal exchange effects, such as those enabled by the SHORYUKEN code, are expected to be essential for accurately predicting these excitations. The open-source SHORYUKEN code enables a path forward to explore these other properties and provides an accessible tool to understand many-body nonlocal exchange effects in these unique nanoscale systems.

Chapter 3

MISTER-T: An Open-Source Software Package for Quantum Optimal Control of Multi-Electron Systems on Arbitrary Geometries

This chapter proposes a generalized framework to solve multi-electron quantum optimal control problems in 2D within effective mass formulation. The work in this chapter resulted from a collaboration with Dr. Mahmut Sait Okyay and was published as an article in *Computer Physics Communications* [57]. The full paper is presented below, with the supplementary information in Appendix F, G and H.

3.1 Abstract

We present an open-source software package, MISTER-T (Manipulating an Interacting System of Total Electrons in Real-Time), for the quantum optimal control of interacting electrons within a time-dependent Kohn-Sham formalism. In contrast to other implementations restricted to simple models on rectangular domains, our method enables quantum optimal control calculations for multi-electron systems (in the effective mass formulation) on nonuniform meshes with arbitrary two-dimensional cross-sectional geometries. Our approach is enabled by forward and backward propagator integration methods to evolve the Kohn-Sham equations with a pseudoskeleton decomposition algorithm for enhanced computational efficiency. We provide several examples of the versatility and efficiency of the MISTER-T code in handling complex geometries and quantum control mechanisms. The capabilities of the MISTER-T code provide insight into the implications of varying propagation times and local control mechanisms to understand a variety of strategies for manipulating electron dynamics in these complex systems.

3.2 Introduction

The control of quantum dynamical systems at the electronic level continues to garner increasing attention in applications such as optically-induced chemical reactions [58, 59, 60], magnetic resonance devices [61, 62, 63, 64], quantum computing [65, 66], quantum simulation [67, 68], and enhanced sensing modalities [69, 70]. Recent advances in both theory and experiment [71, 72, 9, 73, 74] have demonstrated the power of quantum optimal control (QOC) [75] for constructing tailored control fields to enable desired quantum processes in these systems. QOC provides a set of rigorous algorithms and mathematical techniques to formalize a quantum control problem, approach the controllability of the system, and ultimately solve the optimal problem [76, 77]. However, when QOC is applied to an interacting multi-electron system, it is prohibitively expensive to calculate the propagation of wavefunctions due to the non-separability of the Coulomb repulsion and many-body quantum effects. A formally exact but more computationally feasible methodology to describe the same quantum dynamics is time-dependent density-functional theory (TDDFT) [5, 78]. Instead of tackling the original many-body wavefunction, TDDFT introduces a Kohn-Sham system of non-interacting particles moving in a time-dependent effective potential, which yields the same electron density [78]. Since the expectation value of any operator is a functional of the density, one can solve this auxiliary non-interacting system to compute observables, which is significantly less demanding compared to the original many-body problem. The combination of QOC and TDDFT is a promising approach for efficiently controlling electron dynamics in quantum chemistry [79, 80, 81, 82, 83, 84, 85, 86], excited-state preparation [87, 88], and charge-transfer processes [89, 90].

A mathematical framework for QOC within a Kohn-Sham formalism has been previously proposed [10] and implemented in the COKOSNUT code [91]. However, the COKOSNUT code can only handle QOC computations on two-dimensional rectangular-shaped domains and cannot handle irregular geometries or curved boundaries due to its use of rectangular meshes. To address this limitation, we present a general approach in the open-source software package, MISTER-T (Manipulating an Interacting System of Total Electrons in Real-Time), for QOC calculations on arbitrary two-dimensional geometric domains with nonuniform meshes constructed through a finite-element method. QOC calculations require the real-time propagation of Kohn-Sham orbitals, which has been extensively explored in prior TDDFT studies using finite-element bases. For example, Lehtovaara *et al.* [92] presented an all-electron TDDFT calculation using nonuniform finite-element bases, and subsequent research introduced an adaptive finite element method tailored for these applications [93]. Later, Kanungo *et al.* [94] proposed an *a priori* mesh adaption technique by minimizing the semi-discrete and full-discrete error estimates on higher-order finite elements. More recently, a mixed basis was presented to carry out all-electron, real-time TDDFT calculations by augmenting a finite element basis with numerical atomic functions [95]. The MISTER-T code is written in the MATLAB programming environment in a class-oriented fashion to aid in its readability, reusability, and general accessibility to both users and practitioners. The main advantages of the MISTER-T code include its versatility to handle diverse geometries and the capacity to accommodate a range of boundary conditions. Furthermore, we employ advanced propagator integration techniques to evolve wavefunctions in solid-state heterostructure systems characterized by a spatially varying effective mass. We first provide a short overview of the QOC formalism, followed by validation tests and numerical examples of the MISTER-T code for complex geometries and quantum control mechanisms. We conclude by discussing the implications of our QOC calculations to understand and compare strategies for manipulating electron dynamics in these complex systems.

3.3 Theory and Formalism

To calculate the electron dynamics of a many-body interacting system, we commence with the time-dependent Kohn-Sham equations:

$$i\frac{\partial\Psi_j(\mathbf{r},t)}{\partial t} = \left[-\frac{\nabla^2}{2} + \upsilon_{\mathrm{KS}}[\rho(\mathbf{r},t)]\right]\Psi_j(\mathbf{r},t)\ , \tag{3.1}$$

$$\rho(\mathbf{r},t) = \sum_j |\Psi_j(\mathbf{r},t)|^2\,, \tag{3.2}$$

where the one-body effective Kohn-Sham potential $\upsilon_{\mathrm{KS}}(\mathbf{r},t)$ is defined as:

$$\upsilon_{\mathrm{KS}}(\mathbf{r},t) = \upsilon_{\mathrm{ext}}(\mathbf{r},t) + \upsilon_{\mathrm{H}}(\mathbf{r},t) + \upsilon_{\mathrm{xc}}(\mathbf{r},t), \tag{3.3}$$

such that the density computed in Eq. 3.2 is exactly equal to that of the original interacting system by virtue of the one-to-one correspondence requirement [96]. The external potential, υ_{ext}, includes, for example, external control fields and the confining potential. The Hartree term, υ_{H}, takes the usual form $\upsilon_{\mathrm{H}}(\mathbf{r},t) = \int \frac{\rho(\mathbf{r},t)}{|\mathbf{r}-\mathbf{r}'|}\mathrm{d}^3r'$, and the exchange-correlation term υ_{xc} is the effective potential, whose exact form is analytically unknown. In this paper and many practical cases, the adiabatic local density approximation is assumed [96], and the exchange-correlation potential can be approximated as a functional of the instantaneous density [97]. We use Hartree atomic units throughout this paper unless otherwise specified.

In this work, we focus on two-dimensional material systems with diverse cross-sectional geometries within the effective mass formulation. A few examples of realistic 2D material systems include quantum-well nanowires [98], two-dimensional quantum strips [99], and monolayer materials [100]. In addition, certain systems also have quasi-2D geometries, including (1) nanosystems having translational symmetry in one direction with small two-dimensional cross-sections that exhibit quantum confinement effects [12] or (2) large two-dimensional flakes that are too large to calculate with *ab initio* atomistic approaches but can be treated in the effective mass approximation. The effective mass formulation [101, 102, 103] approximates the electronic effects of the material environment by calculating the envelope wavefunction of the electrons using the effective mass m^* and dielectric constant ϵ^*. This formulation, integrated within the Kohn-Sham framework, has been widely applied across various fields, including the study of semiconductor quantum wells [104, 105], coupled electron-photon systems [106], nuclear physics [107, 108], and thermoelectric properties where the effective mass is correlated with local temperature variations [109]. As such, these various applications highlight the versatility and efficacy of the effective mass formulation for capturing complex physical phenomena within 2D material systems. In addition, we focus on closed-shell electronic configurations where each spatial orbital is doubly occupied with a spin-up and spin-down electron. However, all of the approaches presented here can be generalized to accommodate spin-polarized systems as well. The cross-sectional wavefunction, ψ_j, satisfies the two-dimensional equations:

$$\begin{aligned} i\frac{\partial \psi_j(x,y,t)}{\partial t} &= \hat{H}_{\text{KS}}[\underline{\psi}, \underline{u}, t]\psi_j(x,y,t) \\ &= \left[-\nabla_{x,y}\cdot \frac{1}{2m^*(x,y)}\nabla_{x,y} + \upsilon_0(x,y) + \upsilon_{\text{H}}[\rho(x,y,t)] + \upsilon_{\text{xc}}[\rho(x,y,t)] \right. \\ &\quad \left. + \upsilon_{\text{ctr}}(x,y,t)\right]\psi_j(x,y,t), \end{aligned} \tag{3.4}$$

$$\rho(x,y,t) = \sum_{j=1}^{M} g_j \left|\psi_j(x,y,t)\right|^2, \tag{3.5}$$

where $\underline{\psi} = (\psi_1, \cdots, \psi_M)$ are time-dependent cross-sectional Kohn-Sham wavefunctions, $\underline{u} = (u_1, \cdots, u_C)$ are control functions, υ_0 is the time-independent constant potential, υ_{xc} is the exchange-correlation functional, and $m^*(x, y)$ is the effective mass. The υ_{ctr} term is the time-dependent control Hamiltonian modulated by the control amplitudes, $\upsilon_{\mathrm{ctr}}(x, y, t) = \sum_{k=1}^{C} u_k(t) V_k(x, y)$, where V_k is the spatial dependence of the k-th control potential. Typical control fields can be laser pulses, electric gates, or magnetic fields [90]. The g_j factor in Eq. 3.5 accounts for the spin degeneracy of state ψ_j in the system. The Hartree potential, υ_{H}, is determined by solving the Poisson equation:

$$\nabla_{x,y} \cdot \epsilon^*(x, y) \nabla_{x,y} \upsilon_{\mathrm{H}}(x, y, t) = -\rho(x, y, t), \tag{3.6}$$

where $\epsilon^*(x, y)$ is the spatially-dependent dielectric. In this study, the domain of the 2D system was chosen to be large enough such that the electron density decays to zero on the domain boundary, allowing Dirichlet boundary conditions to be enforced on the time-dependent wavefunctions and Hartree potential.

In a QOC problem, the main goal is to find the time-dependent control fields that enable a transition from a given initial quantum state to a target final quantum state. In other words, we seek to minimize a loss functional, $\mathcal{J}[u]$, with respect to the control functions $\underline{u}$ subject to physical constraints, such as the differential equations given in Eqs. 3.4-3.6. In general, the loss functional $\mathcal{J}[u]$ contains objective terms that quantify the difference between the quantum dynamics and the target. Those objective terms are themselves functionals of the density within the TDDFT formalism. In addition, the $\mathcal{J}[u]$ contains the cost term that imposes some constraints on the control field $u(t)$. For example, minimizing the term $\int_0^T u^2(t)\mathrm{d}t$ physically results in the control field expending less energy during the control process. From a mathematical perspective, the cost term is necessary for the existence of solutions to the optimal control problem [110].

We consider a loss functional of the following form:

$$\begin{aligned}\mathcal{J}[\rho,\underline{u}] = &\frac{\beta}{2}\int_0^T \int_\Omega \left(\rho(x,y,t)-\rho_p(x,y,t)\right)^2 \mathrm{d}x\mathrm{d}y\mathrm{d}t \\ &+ \frac{\gamma}{2}\int_\Omega \left(\rho(x,y,T)-\rho_d(x,y)\right)^2 \mathrm{d}x\mathrm{d}y + \frac{\eta}{2}\int_\Omega \chi(x,y)\rho(x,y,T)\mathrm{d}x\mathrm{d}y \\ &+ \frac{\nu}{2}\sum_{k=1}^{C} ||u_k||^2_{H^1(0,T)},\end{aligned} \tag{3.7}$$

where Ω denotes the two-dimensional cross-section of the material under study. The first two lines in Eq. 3.7 are the objective terms, $\mathcal{J}_{\text{obj}}$, and the last line is the cost term, $\mathcal{J}_{\text{cost}}$. $\mathcal{J}_{\text{obj}}$ can be furthermore separated into two parts: (1) a time-dependent part, $\mathcal{J}_{\text{td}}$ (the first line), that forces the density to evolve along a given trajectory, ρ_p, and (2) a terminal part, $\mathcal{J}_{\text{term}}$ (the two terms in the second line), that imposes constraints on the density at the end of propagation. The first term with the $\gamma/2$ pre-factor requires the final density, $\rho(x,y,T)$, to be mathematically close to the target distribution, ρ_d. In the second term with the $\eta/2$ pre-factor, χ is a non-negative characteristic function defined on Ω. Minimizing this term effectively forces the final density to the region where χ takes smaller values. The cost term, $\mathcal{J}_{\text{cost}}$, is the regularization term on all control functions with the H^1 norm definition: $\|f\|_{H^1(0,T)} = \left(\int_0^T (f^2+\dot{f}^2)\mathrm{d}t\right)^{1/2}$, where $\dot{f}$ denotes the time derivative that penalizes the high-frequency components of the control field. It is worth noting that the requirement of controls in $H^1(0,T)$ spaces enables the iterative algorithm to converge faster under some circumstances [91]. The weights of the objective terms β, γ, and η must be non-negative, and the contribution of the cost term must be positive ($\nu > 0$). It is worth mentioning that setting ρ_p to some constant time-independent distribution, ρ_D, and including only the first and last term in Eq. 3.7 will enable the system to approach ρ_D as fast as possible and remain in that state, which can be helpful to find the minimum time to reach the target.

We again emphasize that our ultimate goal is to find a set of control fields, $\underline{u}$, such that the loss functional, $\mathcal{J}[\rho[\underline{u}], \underline{u}]$, is minimized subject to the constraint of satisfying the time-dependent Kohn-Sham equations in Eqs. 3.4 - 3.6 (the existence of solutions to the optimal control problem is discussed more rigorously in Refs. [11, 110]). Regarding numerical algorithms, several gradient-free and gradient-based methods exist to solve optimization problems [77], but the former takes many more iterations to converge compared to the latter. Therefore, we adopt a gradient-based method and derive the functional derivative of $\mathcal{J}$ with respect to $\underline{u}$.

To find the minimum of $\mathcal{J}[\rho[\underline{u}], \underline{u}]$ subject to the constraints, we utilize a Lagrange multiplier by introducing a set of adjoint states, $\underline{\lambda} = (\lambda_1, \cdots, \lambda_M)$, and define the following Lagrange functional:

$$\mathcal{L}[\underline{\psi}, \underline{\lambda}, \underline{u}] = \mathcal{J}[\rho[\underline{\psi}], \underline{u}] + \mathrm{Re} \sum_{j=1}^{M} \int_0^T \left\langle \lambda_j, \left(i\frac{\partial}{\partial t} - \hat{H}_{\mathrm{KS}}[\underline{\psi}, \underline{u}, t] \right) \psi_j \right\rangle \mathrm{d}t, \tag{3.8}$$

where $\langle \cdot, \cdot \rangle$ is the usual inner product defined in the Hilbert space. The necessary first-order optimality conditions state that the Fréchet derivative of $\mathcal{L}$ with respect to $(\underline{\psi}, \underline{\lambda}, \underline{u})$ equals zero [11]. Setting the functional derivative of $\mathcal{L}$ with respect to $\underline{\lambda}$ recovers the time-dependent Kohn-Sham equation (Eq. 3.4). Similarly, taking the derivative with respect to

$\underline{\psi}$ gives the backward propagation equation for adjoint states:

$$i\frac{\partial \lambda_j}{\partial t} = \hat{H}_{\mathrm{KS}}[\underline{\psi}, \underline{u}, t]\lambda_j + G_{\mathrm{KS}_j}[\underline{\psi}, \underline{\lambda}] - \nabla_{\psi_j}\mathcal{J}_{\mathrm{td}}[\underline{\psi}], \tag{3.9}$$

$$\lambda_j(T) = -i\nabla_{\psi_j}\mathcal{J}_{\mathrm{term}}. \tag{3.10}$$

The G_{KS_j} term comes from the nonlinear dependence of $\hat{H}_{\mathrm{KS}}$ with respect to ψ_j, specifically the Hartree, $\upsilon_{\mathrm{H}}[\rho]$, and exchange-correlation, $\upsilon_{xc}[\rho]$, potentials through the density, ρ. We subsequently have:

$$G_{\mathrm{KS}_j}[\underline{\psi}, \underline{\lambda}] = 2g_j\psi_j \sum_{l=1}^{M} \upsilon_{\mathrm{H}}\left[\mathrm{Re}\left(\psi_l\bar{\lambda}_l\right)\right] + 2g_j\psi_j\frac{\partial \upsilon_{\mathrm{xc}}}{\partial \rho}(\rho[\underline{\psi}])\sum_{l=1}^{M}\mathrm{Re}\left(\psi_l\bar{\lambda}_l\right), \tag{3.11}$$

$$\nabla_{x,y}\cdot\epsilon^*(x,y)\nabla_{x,y}\upsilon_{\mathrm{H}}\left[\mathrm{Re}\left(\psi_l\bar{\lambda}_l\right)\right] = -\mathrm{Re}\left(\psi_l\bar{\lambda}_l\right), \tag{3.12}$$

where $\bar{\lambda}_l$ denotes the complex conjugate of λ_l. The $\nabla_{\psi_j}\mathcal{J}_{\mathrm{td}}$ term is the gradient representation of the functional derivative, $D_{\psi_j}\mathcal{J}_{\mathrm{td}}\delta\psi_j$, and is given by:

$$\nabla_{\psi_j}\mathcal{J}_{\mathrm{td}}[\underline{\psi}] = 2\beta\left(\rho[\underline{\psi}(t)] - \rho_p(t)\right)g_j\psi_j. \tag{3.13}$$

Eq. 3.10 sets the final condition for adjoint states, and $\nabla_{\psi_j}\mathcal{J}_{\mathrm{term}}$ is determined by:

$$\nabla_{\psi_j}\mathcal{J}_{\mathrm{term}} = 2\gamma\left(\rho(T) - \rho_d\right)g_j\psi_j(T) + \eta\chi g_j\psi_j(T). \tag{3.14}$$

We proceed by taking the functional derivative with respect to u_k, and the gradient, $\nabla_{u_k}\mathcal{L}$, is given by $D_{u_k}\mathcal{L}\delta u_k = \langle\nabla_{u_k}\mathcal{L}, \delta u_k\rangle_{H^1(0,T)}$ where $\langle\cdot\,,\cdot\rangle_{H^1(0,T)}$ is the scalar product on the

$H^1(0,T)$ space[111]. Assuming $u_k(0) = u_k(T) = 0$ gives:

$$\nabla_{u_k}\mathcal{L} = \nu u_k + f_k, \tag{3.15}$$

where f_k is determined by:

$$f_k - \ddot{f}_k = -\mathrm{Re}\sum_{l=1}^{M} \langle \lambda_l(t), V_k\psi_l(t)\rangle\,,\ f_k(0) = f_k(T) = 0, \tag{3.16}$$

where $\ddot{f}$ denotes the second time derivative. If the regularization term in Eq. 3.7 uses the L^2 norm, $\|f\|_{L^2(0,T)} = \left(\int_0^T f^2 \mathrm{d}t\right)^{1/2}$, the gradient can be simplified to:

$$\nabla_{u_k}\mathcal{L} = \nu u_k - \mathrm{Re}\sum_{l=1}^{M} \langle \lambda_l, V_k\psi_l\rangle\,. \tag{3.17}$$

Calculating $\nabla_{u_k}\mathcal{L}$ requires knowledge of the wavefunctions $\underline{\psi}$ and adjoint variables $\underline{\lambda}$; however, the propagation of $\underline{\lambda}$ depends simultaneously on $\underline{\psi}$. Therefore, the forward (Eq. 3.4) and backward equation (Eq. 3.9) must be solved before computing the gradient. We can then employ efficient gradient-based algorithms to update the control fields iteratively. The next section discusses the optimization scheme and numerical implementations used in our MISTER-T program.

3.4 Algorithm and Numerical Implementation

In our MISTER-T program, the finite element method is used to spatially discretize the geometric domain, and the propagation time, T, is divided into L uniform intervals with

$\Delta t = T/L$. As mentioned above, we propagate $\underline{\psi}$ forward and $\underline{\lambda}$ backward to compute the gradient. To evolve the wavefunctions, we use a Strang operator splitting method [11], which splits the Hamiltonian into kinetic and potential parts and calculates the time evolution for each. We start with the time-dependent Kohn-Sham equation (Eq. 3.4) and apply Strang splitting to compute $\psi_j(t + \Delta t)$ from $\psi_j(t)$:

$$\begin{aligned} \psi_j(t+\Delta t) &= \exp\left(-i\frac{\Delta t}{2}\upsilon(\rho', t+\Delta t)\right)\psi_j', \\ \psi_j' &= \exp\left(i\Delta t\nabla\cdot\frac{1}{2m^*}\nabla\right)\exp\left(-i\frac{\Delta t}{2}\upsilon(\rho,t)\right)\psi_j(t), \end{aligned} \tag{3.18}$$

where $\upsilon(\rho, t)$ is the total potential: $\upsilon = \upsilon_0 + \upsilon_{\mathrm{H}} + \upsilon_{\mathrm{xc}} + \upsilon_{\mathrm{ctr}}$, computed with the value of ρ used for υ_{H}, υ_{xc}, and the control fields at time t. In addition, ρ' is the density calculated with $\underline{\psi}'$. We have omitted the (x, y) coordinates in the expressions above for notational simplicity.

The backward equation (Eq. 3.9) is an inhomogeneous Schrödinger-like equation. The extension of the Strang splitting approach can be applied to compute $\lambda_j(t - \Delta t)$ from $\lambda_j(t)$:

$$\begin{aligned} \lambda_j(t-\Delta t) &= \exp\left(i\frac{\Delta t}{2}\upsilon(\rho(t-\Delta t), t-\Delta t)\right)\lambda_j', \\ \lambda_j' &= \exp\left(-i\frac{\Delta t}{2}\nabla\cdot\frac{1}{2m^*}\nabla\right)\left(\lambda_j'' + i\Delta t q_j[\underline{\psi}(t-\Delta t/2), \underline{\lambda}'']\right), \\ \lambda_j'' &= \exp\left(-i\frac{\Delta t}{2}\nabla\cdot\frac{1}{2m^*}\nabla\right)\exp\left(i\frac{\Delta t}{2}\upsilon(\rho(t),t)\right)\lambda_j(t), \end{aligned} \tag{3.19}$$

where $\underline{\psi}(t-\Delta t/2)$ is approximated by $(\underline{\psi}(t-\Delta t)+\underline{\psi}(t))/2$, and q_j is defined as:

$$q_j[\underline{\psi},\underline{\lambda}] = G_{\mathrm{KS}_j}[\underline{\psi},\underline{\lambda}] - \nabla_{\psi_j}\mathcal{J}_{td}[\underline{\psi}]. \tag{3.20}$$

The time evolution for the potential part is simple to compute since $v(\rho, t)$ is a diagonal matrix. However, it is not straightforward to efficiently compute the kinetic part with a position-dependent mass on nonuniform mesh grids.

In our work on solid-state material systems, we propagate wavefunctions with a position-dependent kinetic term:

$$i\frac{\partial\psi(\mathbf{r},t)}{\partial t} = -\frac{1}{2}\nabla\cdot\left(\frac{1}{m^*(\mathbf{r})}\nabla\psi(\mathbf{r},t)\right). \tag{3.21}$$

The above differential equation does not have an analytical solution due to the spatially varying mass. In this work, we use a Green's function method (a propagator method) and a WKB approximation to derive a solution. Details of the derivation are given in F. The approximated solution is given by:

$$\psi(\mathbf{r},t_0+\Delta t) \approx \int \exp\left(i\mathbf{k}\cdot\mathbf{r}\right)\mathcal{K}(\mathbf{r},\mathbf{k})\psi(\mathbf{k},t_0)\mathrm{d}^2\mathbf{k}, \tag{3.22}$$

where $\psi(\mathbf{k},t_0)$ is the Fourier transform of the wavefunction defined by

$$\psi(\mathbf{k},t_0) = \left(\frac{1}{2\pi}\right)^2 \int \exp\left(-i\mathbf{k}\cdot\mathbf{r}_0\right)\psi(\mathbf{r}_0,t_0)\mathrm{d}^2\mathbf{r}_0, \tag{3.23}$$

and $\mathcal{K}(\mathbf{r}, \mathbf{k})$ is the kernel, with the first-order expression determined as:

$$\mathcal{K}(\mathbf{r}, \mathbf{k}) = \exp\left(-i\frac{\mathbf{k}^2}{2m^*}\Delta t\right) \exp\left(\frac{\mathbf{k}\cdot \nabla m^*}{2m^{*2}}\Delta t\right). \tag{3.24}$$

In the MISTER-T package, we implement the second-order approximation for the kernel, which is given in Eq. F.13.

The WKB approach is a "semiclassical" approximation in the sense that it is valid when the mass is "slowly varying" compared to the de Broglie wavelength. More quantitatively, the following condition has to be satisfied:

$$\frac{m^*}{|\nabla m^*|} \gg D, \tag{3.25}$$

where D denotes the size of the system. The above inequality requires that the characteristic distance, $m^*/|\nabla m^*|$, over which the mass varies appreciably, must be large compared to D. In addition, the time step Δt has to be sufficiently small to obey Eqs. F.16 and F.17.

It is important to note that Eq. 3.22 *cannot* be computed fast with the inverse Fourier transform due to the position dependence of the kernel. Specifically, the complexity of direct summation is $\mathcal{O}(N^2)$, where N is the number of mesh nodes. To compute this integral efficiently, we build a pseudoskeleton decomposition [112, 113, 114] of the kernel:

$$\mathcal{K}(\tilde{\mathbf{r}}, \tilde{\mathbf{k}}) \approx \mathcal{K}(\tilde{\mathbf{r}}, \tilde{\mathbf{k}}_D) G \mathcal{K}(\tilde{\mathbf{r}}_D, \tilde{\mathbf{k}}), \tag{3.26}$$

where $\tilde{\mathbf{r}}$ and $\tilde{\mathbf{k}}$ are the discretized position and momentum points, respectively, with a cardinality on the order of N: $|\tilde{\mathbf{r}}| = N$ and $|\tilde{\mathbf{k}}| = \mathcal{O}(N)$. $\tilde{\mathbf{k}}_D(\tilde{\mathbf{r}}_D)$ is a set of r_ε columns (rows) with rank r_ε depending on the prescribed error ε of this decomposition. We require that the paralleleloid spanned by $\tilde{\mathbf{k}}_D(\tilde{\mathbf{r}}_D)$ has the maximum volume among all paralleleloids spanned by a set of columns (rows) of $\mathcal{K}(\tilde{\mathbf{r}}, \tilde{\mathbf{k}})$ in the r_ε dimensional space. G is a $r_\varepsilon \times r_\varepsilon$ matrix, which minimizes the Frobenius norm:

$$\left\| \mathcal{K}(\tilde{\mathbf{r}}, \tilde{\mathbf{k}}) - \mathcal{K}(\tilde{\mathbf{r}}, \tilde{\mathbf{k}}_D) G \mathcal{K}(\tilde{\mathbf{r}}_D, \tilde{\mathbf{k}}) \right\|_F . \tag{3.27}$$

For the case of large N, it is computationally costly (both in time and memory) to choose $\tilde{\mathbf{k}}_D$, $\tilde{\mathbf{r}}_D$, and calculate G directly. Instead, we use the algorithm by Engquist et al. [113] based on the random projection and pivoted QR factorization, which can generate the decomposition with much fewer operations and is easy to implement. The procedures are summarized in Algorithm 1; the accuracy of Algorithm 1 is discussed in detail in G.

Using the decomposition of the kernel, the integral in Eq. 3.22 can be computed as:

$$\psi(\mathbf{r}, t_0 + \Delta t) \approx \mathcal{K}(\mathbf{r}, \tilde{\mathbf{k}}_D) G \int \exp\left(i \frac{\mathbf{k} \cdot \mathbf{r}}{\hbar} \right) \mathcal{K}(\tilde{\mathbf{r}}_D, \mathbf{k}) \psi(\mathbf{k}, t_0) \mathrm{d}^2\mathbf{k}, \tag{3.28}$$

where the integration can be evaluated by the inverse Fourier transform. To perform calculations efficiently on nonuniform nodes, we utilize the FINUFFT library [115, 116], which computes the nonuniform fast Fourier transform efficiently and easily. The complexity of calculating Eq. 3.28 is $\mathcal{O}(r_\varepsilon N \log N)$.

After propagating the forward and backward equations, it is straightforward to compute the gradient via Eqs. 3.15 and 3.16. We then use the nonlinear conjugate gradient (NCG) scheme to find the search direction, which generally takes fewer iterations than the

Algorithm 1 Pseudoskeleton decomposition based on pivoted QR factorization and random projection, implemented in `pre_optimization.m`

```
Input: kernel defined by Eq. 3.24, $\tilde{\mathbf{r}}$, $\tilde{\mathbf{k}}$, rank $r_\varepsilon$ (full matrix $\mathcal{K}(\tilde{\mathbf{r}}, \tilde{\mathbf{k}})$ is not necessarily needed)
Output: Column set $\tilde{\mathbf{k}}_D$, row set $\tilde{\mathbf{r}}_D$, matrix $G$
randomly pick a set of row $\Omega_1 \subset \tilde{\mathbf{r}}$ of size $M_1 r_\varepsilon$
apply pivoted QR decomposition on matrix $\mathcal{K}(\Omega_1, :)$ to have $\mathcal{K}(\Omega_1, P_1) = Q_1 R_1$, where $P_1$ is a permutation of $N$ columns such that the diagonal entries of the upper triangular matrix $R_1$ decrease in magnitude
set $\tilde{\mathbf{k}}_D$ to be the first $r_\varepsilon$ members of $P_1$
randomly pick a set of column $\Pi_1 \subset \tilde{\mathbf{k}}$ of size $M_1 r_\varepsilon$
apply pivoted QR decomposition on matrix $\mathcal{K}(:, \Pi_1)^T$ to have $\mathcal{K}(P_2, \Pi_1)^T = Q_2 R_2$, where $P_2$ is a permutation of $N$ rows such that the diagonal entries of the upper triangular matrix $R_2$ decrease in magnitude, and $(\cdot)^T$ denotes the transpose
set $\tilde{\mathbf{r}}_D$ to be the first $r_\varepsilon$ members of $P_2$
randomly pick a set of row $\Omega_2$ and a set of column $\Pi_2$ , both of size $M_2 r_\varepsilon$
$G$ is chosen such that $\mathcal{K}(\Omega_2, \Pi_2) = \mathcal{K}(\Omega_2, \tilde{\mathbf{k}}_D) G \mathcal{K}(\tilde{\mathbf{r}}_D, \Pi_2)$, or $G = \left(\mathcal{K}(\Omega_2, \tilde{\mathbf{k}}_D)\right)^+ \mathcal{K}(\Omega_2, \Pi_2) \left(\mathcal{K}(\tilde{\mathbf{r}}_D, \Pi_2)\right)^+$, where $(\cdot)^+$ denotes the pseudo-inverse
```

steepest descent method [11]. A bisection algorithm [91] is then implemented to find the largest step size to decrease the value of $\mathcal{J}$ along the descent direction. The optimization logic of the program is described in Algorithm 2.

The MISTER-T code is written in MATLAB for its easy readability, powerful matrix multiplication ability, and user-friendly implementation of the finite element discretization. At the same time, the program is coded in a class-oriented style for reusability, flexibility, productivity, and simplicity. To initiate the MISTER-T program, the user specifies details of the setup for the QOC problem in the `input_parameters.m` file, including geometry, material parameters of the system, confining potential, propagation time, weights in the loss functional, and control potential (see Section 3.5). Passing this filename as an argument of the constructor for the class `controlSystem` can initialize an object: `model=controlSystem('input_parameters.m')`. The file `controlSystem.m` contains the definition of this class template. During the initialization, the program loads the user's specified parameters, initializes variables, and generates a finite element mesh grid. For the initial wavefunction, the user can set the variable `model.psi0` manually, or let the program calculate eigenstates of the system by solving time-independent Schrödinger and Poisson equations with self-consistent iterations [30], which is implemented in `solve_initial_states.m`. Before solving the optimization problem, `pre_optimization.m` has to be called to initialize various calculations, most of which decompose the kernel as stated in Algorithm 1. Once this is done, the code is ready to run Algorithm 2 by calling `optimize(model)`. Control fields are updated iteratively, in which the forward (Eqs. 3.4 and 3.6) and backward equations (Eqs. 3.9 and 3.10) are solved in the `solve_forward_se.m` and `solve_backward_se.m` files, according to Eqs. 3.18 and 3.19, respectively.

The time propagation for the kinetic part is performed in the `apply_exp_kinetic.m` m-file using Eq. 3.28 and a nonuniform fast Fourier transform. In H, we examine the convergence rates of propagating Kohn-Sham orbitals with respect to the finite-element mesh size and timestep. It is worth mentioning that filters are necessary to remove the high-frequency noise after transforming the wavefunctions to momentum space on a nonregular mesh. We provide a filtering mechanism in the `filter_high_frequency.m` file to detect and retain signals while eliminating undesired noise. This process involves locating the frequency component with the highest amplitude and designating it as the initial seed of the peak. Subsequently, we iteratively expand the peak by including its neighboring frequencies. This expansion continues until neighboring frequencies have amplitudes that fall below a certain threshold, at which point they are classified as noise and excluded from the peak. We then repeat this peak-finding process for the remaining frequency space until all signal peaks are identified, and the remaining noise is discarded. With both forward and backward equations solved, the gradient can be evaluated in `grad_lagrange.m` using Eqs. 3.15 and 3.16. The new descent direction can then be computed with Hager-Zhang formulas [117] from the NCG method. To find the stepsize along this direction, the `linesearch.m` m-file uses the bisection line search method (Algorithm 5 in [91]). This part involves repetitive propagations of the forward equation to compute the value of the loss functional at different stepsizes (and its gradient with respect to stepsize), which is the most computationally costly calculation. The MISTER-T program contains the `linesearch_p.m` m-file that can compute the gradient in parallel to effectively reduce the overall execution time using the parallel computing toolbox in MATLAB. Users can enable this by setting `model.par_enable = true` if the toolbox is installed. At the end of each iteration, the control field is updated. The program stops when the max iteration is reached or certain variables are below the given tolerance values, as shown in Algorithm 2. The results of the optimization are saved in a `results.mat` file, including the optimal control field, history of loss values, stepsizes, and gradients at each iteration.

3.5 Results and Discussions

We commence this section with a simple optimal control system with known numerical results, which allows us to validate our new implementation. We then present two examples highlighting the capability and versatility of the MISTER-T program for other nonuniform, complex geometries and potentials. These examples simulate charge transfer controlled by laser pulses and electric gates on irregularly shaped geometries. Our last example further explores varying effective masses across different domains.

3.5.1 Validation Test

To validate our implementation, we test the output of the MISTER-T code against known numerical results from recent work in Ref. [91]. In this example, we first carry out a simple forward propagation by inputting a prescribed control field, $u_{\text{pre}}(t)$, to propagate the wavefunctions for some time T and record its density trajectory, $\rho_{\text{pre}}(t)$. With the previous

Algorithm 2 Optimal minimization of the loss functional, $\mathcal{J}[\rho[\underline{u}], \underline{u}]$, as implemented in `optimize.m`

Input: Quantum dynamics equations (Eqs. 3.4 and 3.6) and loss functional (Eq. 3.7)

Output: Optimal control fields $\underline{u}(t)$

```
set $k$ to 0, set initial wavefunctions $\underline{\psi}^0$, and initial control fields $\underline{u}^0$
while $k < k_{\text{max}}$ do
    compute $\underline{\psi}^{k+1}$ by evolving forward Eqs. 3.4 and 3.6 with $\underline{u}^k$
    compute $\underline{\lambda}^{k+1}$ by evolving backward Eqs. 3.9 and 3.10 with $\underline{u}^k$ and $\underline{\psi}^{k+1}$
    calculate the gradient $\nabla_{\underline{u}^k}\mathcal{L}$ according to Eqs. 3.15 and 3.16 with $\underline{u}^k$, $\underline{\lambda}^{k+1}$ and $\underline{\psi}^{k+1}$
    if $||\nabla_{\underline{u}^k}\mathcal{L}||_{H^1(0,T)} < \tau_g$(tolerance of the gradient norm) then
        break
    end if
    find the descent direction $\underline{d}^k$ with the Hager-Zhang formulas [117]
    calculate the stepsize $\alpha^k$ along $\underline{d}^k$ with the bisection linesearch method
    if $\alpha^k < \tau_\alpha$(tolerance of the stepsize) then
        break
    end if
    update control fields $\underline{u}^{k+1} = \underline{u}^k + \alpha^k \underline{d}^k$
    set $k = k + 1$
end while
return $\underline{u}^k$
```

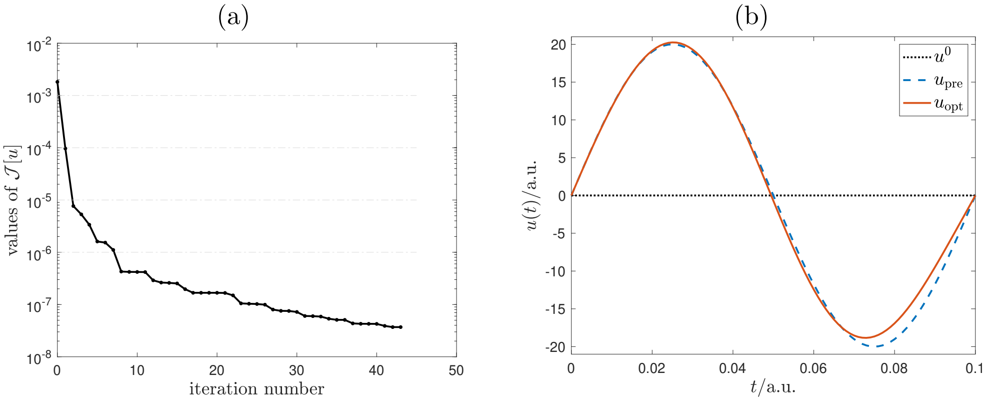

Figure 3.1: (a) Loss functional as a function of iteration number. (b) Comparison of the prescribed field, $u_{\text{pre}}(t)$, initial control field, $u^0(t) = 0$, and resultant optimal control field, $u_{\text{opt}}(t)$, as functions of time.

quantities calculated, we then carry out a QOC calculation and set ρ_{pre} as ρ_p in the loss functional (Eq. 3.7), and run the optimization in Algorithm 2 to find the optimal control $u_{\text{opt}}(t)$, which can be compared to the original input, $u_{\text{pre}}(t)$. The MATLAB code to set up this control problem is given below:

```
degree_of_polygon = 4;
vector_of_side_lengths = [0.4];
number_of_triangles = 2e5;
T = .1;
Nt = 100;
vector_of_masses = [1];
vector_of_eps = [1];
beta = 1; gam = 0; eta = 0; nu = 1e-10;
rho_p = rho_pre;
omega=sqrt(100);
iwf= @(x) exp(-4+(2*sqrt(2*omega)*x)-(1/2)*omega*x.^2)
        *(omega/pi)^(1/4);
iwfrtd= @(x) exp(-4-(2*sqrt(2*omega)*x)-(1/2)*omega*x.^2)
        *(omega/pi)^(1/4);
psi0(:,1) = iwf(x).*iwf(y);
psi0(:,2) = iwfrtd(x).*iwf(y);
psi_wgt = ones( size(psi0) );
V_ctr = @(x,y) [x.^2;y.^2];
```

The variables in the MATLAB code above are further described below:

- `degree_of_polygon`: indicates the shape of the nanowire's cross-section. For example, 4 and 6 denote a square and hexagon, respectively.
- `vector_of_side_lengths`: side lengths of the domain, in units of nm
- `number_of_triangles`: number of elements in the finite-element discretization
- `T`: propagation time in atomic units (a.u.)
- `Nt`: number of time intervals
- `vector_of_masses`: effective mass, in electron rest mass units
- `vector_of_eps`: permittivity, in units of the vacuum permittivity
- `beta,gam,eta,nu`: weights in loss functional given by Eq. 3.7
- `rho_p`: target density trajectory, ρ_p, in loss functional given by Eq. 3.7
- `psi0`: initial wavefunctions
- `psi_wgt`: prefactors $\underline{g}$ by Eq. 3.5
- `V_ctr`: control potential

In short, this example models two wavefunctions governed by a harmonic potential within a square domain. Fig. 3.1a shows the monotonic decrease and convergence of the loss functional as a function of iterations. Fig. 3.1b compares the optimal control, $u_{\text{opt}}(t)$ (solid red line), with the prescribed field, $u_{\text{pre}}(t)$ (dashed blue line), which we pre-selected as a sinusoidal function. It is worth mentioning that even when the guess field, $u^0(t)$ (dotted black line), is initialized to zero, the program converges to a solution that is numerically close to the prescribed one, achieving a low loss value of 3.7×10^{-8}. By adjusting the tolerances for τ_g and τ_α and increasing the number of iterations, one can further decrease the loss value and obtain an optimal field even more similar to u_{pre}. It is worth mentioning that the weight, ν, for the cost term, $\mathcal{J}_{\text{cost}}$, in Eq. 3.7 should be kept small. A large value of ν would steer the program to prioritize minimizing the cost term, resulting in a control field with a reduced norm but diminished resemblance to the prescribed field, u_{pre}. These numerical results of our finite-element-based code are consistent with those given by the rectangular-domain simulation in Ref. [91] and provide a validation of the implementation in the MISTER-T code.

3.5.2 Asymmetric Double-Well Potential

In this second example, we consider the control of charge transfer between two asymmetric potential wells on a hexagonal cross-section, which can be considered as a simple model of 2D quantum dots/defects in a semiconductor material. The confining potential in atomic units is given by:

$$v_0(x, y) = x^4/32 + x^3/16 - x^2/2 + y^2. \tag{3.29}$$

The `solve_initial_states.m` m-file is used to compute the eigenstates of the system, and the ground state is chosen as the initial wavefunction, ψ^0. Fig. 3.2 depicts the confining potential, $v_0(x, y)$, and initial density, $\rho(t = 0)$, trapped in the left potential well. Our objective is to maximize charge transfer to the right well using an x-polarized field with a linear control potential, $V(x, y) = x$. The MATLAB code to set up this control problem is given below:

```
degree_of_polygon = 6;
vector_of_side_lengths = [0.5];
number_of_triangles = 2e5; % 2e4
T = .2; % 40
Nt = 100; % 1000
vector_of_masses = [0.2];
vector_of_eps = [9.28];
beta = 0; gam = 0; eta = 1; nu = 1e-10;
% solve time-independent schrödinger equation
psi0 =  solve_initial_states();
psi_wgt = ones( size(psi0) )*2;
V_ctr = @(x,y) [x;0];
% set the characteristic function
chi = (x<0) | (x>0.3);
% set the constant confining potential
V_cst = x^4/32 + x^3/16 - x^2/2 + y^2;
```

We set the characteristic function, χ, in the $\mathcal{J}_{\text{term}}$ term given in Eq. 3.7 as

$$\chi(x, y) = \begin{cases} 0 & 0 < x < 0.3 \\ 1 & \text{otherwise} \end{cases}, \tag{3.30}$$

which will direct electrons to the potential well on the right. To demonstrate the robustness of our code, we consider the optimization problem for both short ($T = 0.2$ a.u.) and long ($T = 40$ a.u.) propagation times. Fig. 3.3 illustrates the evolution of the loss functional with the optimal pulse shape for both scenarios.

Fig. 3.3 clearly shows that the convergence of our implementation varies with the number of iterations being executed. Specifically, the system with $T = 40$ needs longer

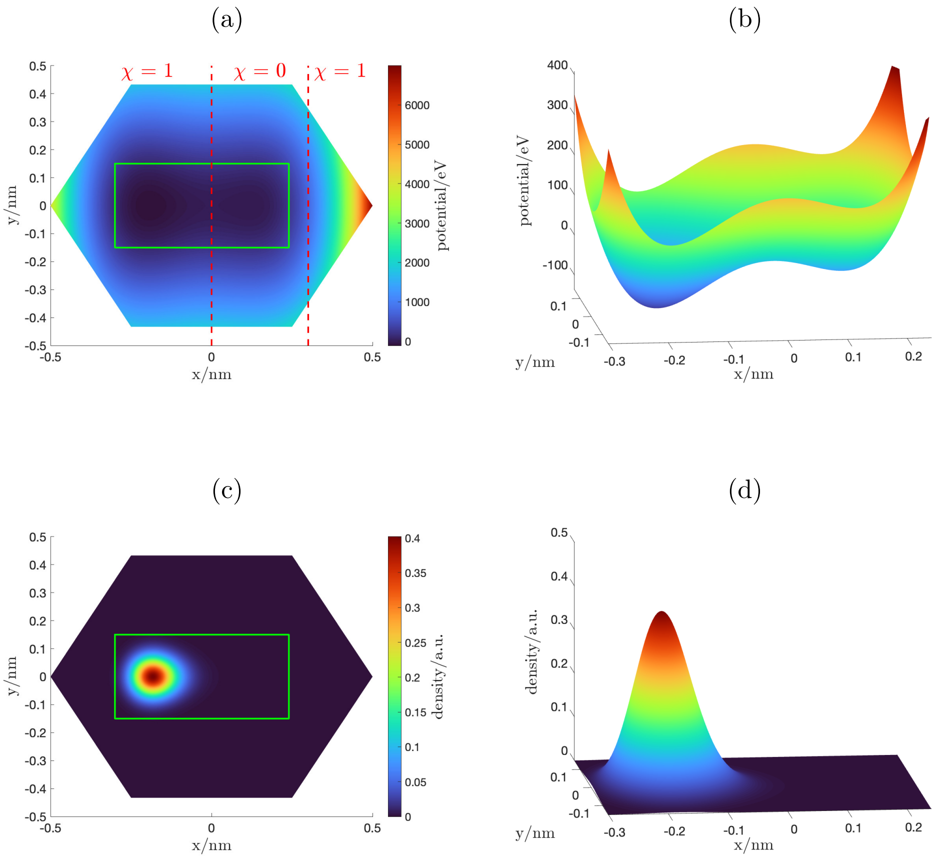

Figure 3.2: Confining potential, υ_0, (a) and the initial electron density, $\rho(t = 0)$ (c) a magnified view of the potential and electron density within the enclosed green rectangle is shown in panels (b) and (d), respectively. The red dashed lines in (a) represent the borders of the characteristic function.

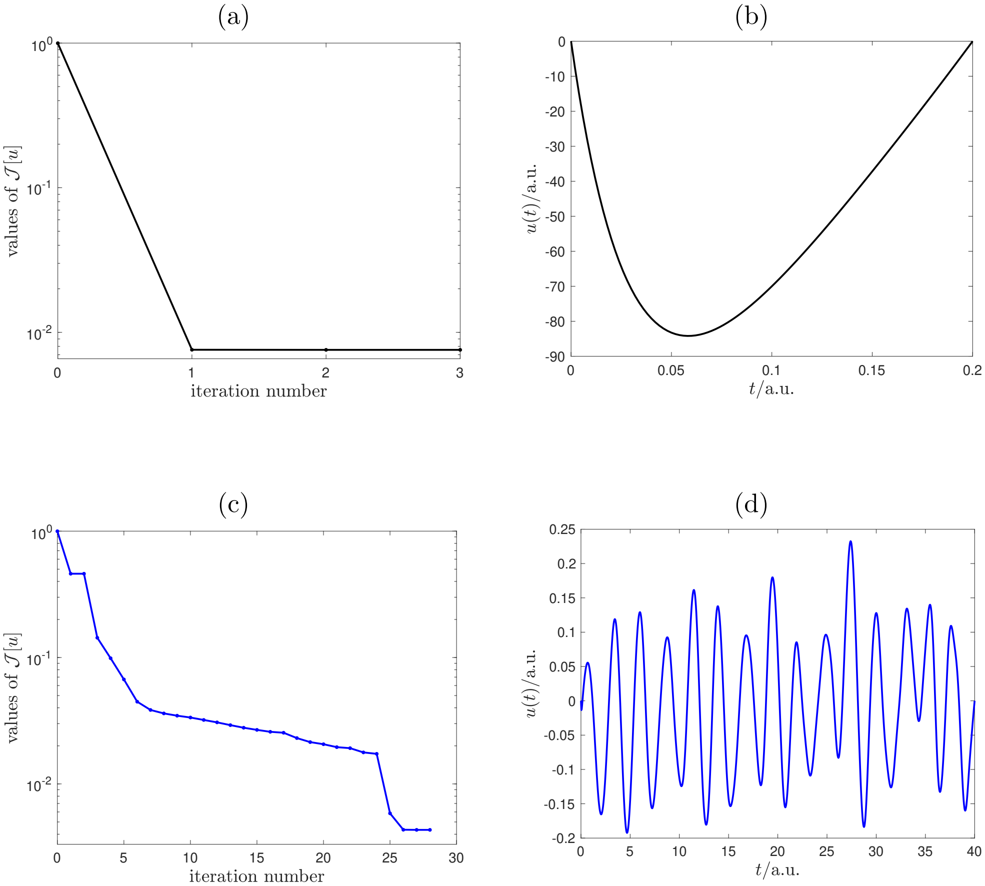

Figure 3.3: Loss functional as a function of iteration number for (a) short and (c) long propagation times, respectively. Converged optimal control, $u_{\text{opt}}(t)$, as a function of time for (b) short and (d) long propagation times, respectively.

steps, while the one with $T = 0.2$ obtains a low loss value in just one step. Even though the physical system is the same, the difference in propagation time creates a distinct optimization problem in both scenarios. This also manifests itself in the optimal control fields: a stronger laser pulse is required to drive electrons rightward within a shorter time. The disparity becomes even more pronounced when comparing the energy of the control field, $\epsilon = \int u^2(t)\mathrm{d}t$, used during each process: $\epsilon_{T=0.2} = 684.83$ a.u. and $\epsilon_{T=40} = 0.39$ a.u..

The electron dynamics controlled by the laser pulses in Figs. 3.3b and 3.3d represent distinct electron transfer strategies. Fig. 3.4 provides a few selected snapshots of the electron density with the total confining and control potentials, $\upsilon_0 + \upsilon_{\text{ctr}}$, for both processes. The Supplementary Material provides video animation files for the entire simulation time for both the short and long propagation examples studied in this section. It is worth noting that the strong pulse (Figs. 3.4a - 3.4d) contributes a large field and essentially changes the potential to a linearly varying profile such that all the electrons move to the right (similar to a classical object sliding downhill). In contrast, the weaker field (Figs. 3.4e - 3.4h) leaves the overall potential shape unchanged and subtly modulates the electron dynamics to give a more refined final density distribution and superior yield. We can estimate the kinetic energy of the final state at the end of the propagation by calculating the expectation of the kinetic operator, $\langle K \rangle = \langle \psi(T)| - \frac{\nabla^2}{2m^*} |\psi(T)\rangle$, which gives $\langle K \rangle_{T=0.2} \approx 6.96 \times 10^3$ eV and $\langle K \rangle_{T=40} \approx 48.20$ eV. This indicates that the strong field in Fig. 3.3b pushes electrons rightward in a short span with most of its energy transferred to their momentum; i.e., the final state in Fig. 3.4d will continue moving after time T when no control field is applied. To analyze how the weak field in Fig. 3.3d controls the electron density, Fig. 3.5a plots the frequency spectrum of the control field. A prominent peak is clearly observed at a frequency of $\omega = 0.375$ a.u., which corresponds to the energy difference (ΔE) between the ground and first excited state of the system, $\Delta E = 2\pi\omega$, as shown in Fig. 3.5b. This suggests that one propagation channel involves the evolution of the initial state (dotted blue line) to the first excited state (dashed red line).

3.5.3 Triple-Well Potential with Local Control

In this last example, we demonstrate the capability of the MISTER-T code to handle complex geometries with a position-dependent effective mass, $m^*(x, y)$. Fig. 3.6a shows the geometry under study, which consists of three fused hexagons, denoted by A1, A2, and A3, with three interior points, P1 $(-l/2, 0)$, P2 $(l/4, -\sqrt{3}l/4)$, and P3 $(l/4, \sqrt{3}l/4)$, where l is the side length of the hexagon. This example is more challenging since we consider a local control potential that takes a Gaussian shape, $V(x, y) = \exp\left[-(x + l/2)^2/(l/30)\right] \cdot \exp\left[-y^2/(l/30)\right]$. The control potential is centered around point P1, shown as a blue dot in Fig. 3.6a. This setup simulates the effect of an electric gate, where the control field is the applied voltage. To highlight the flexibility of the MISTER-T code, we have allowed the effective mass to vary slowly across the domain such that Eq. 3.25 is satisfied, as shown in Fig. 3.6b.

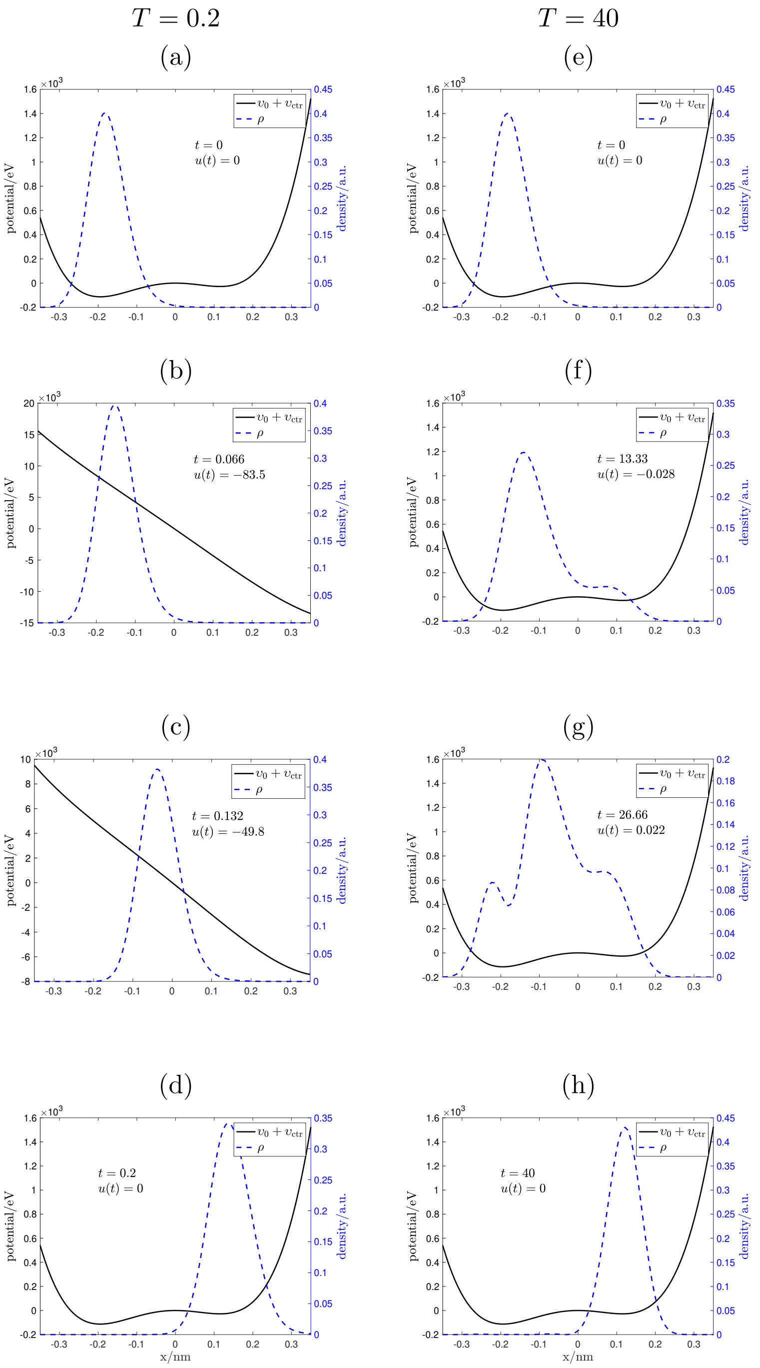

Figure 3.4: Snapshots of the electron density, ρ, and potential, $v_0 + v_{\mathrm{ctr}}$, along the line $y = 0$ at (a,e) $t = 0$, (b,f) $t = T/3$, (c,g) $t = 2T/3$, and (d,h) $t = T$ (d,h) for short and long propagation times, in the left and right columns, respectively.

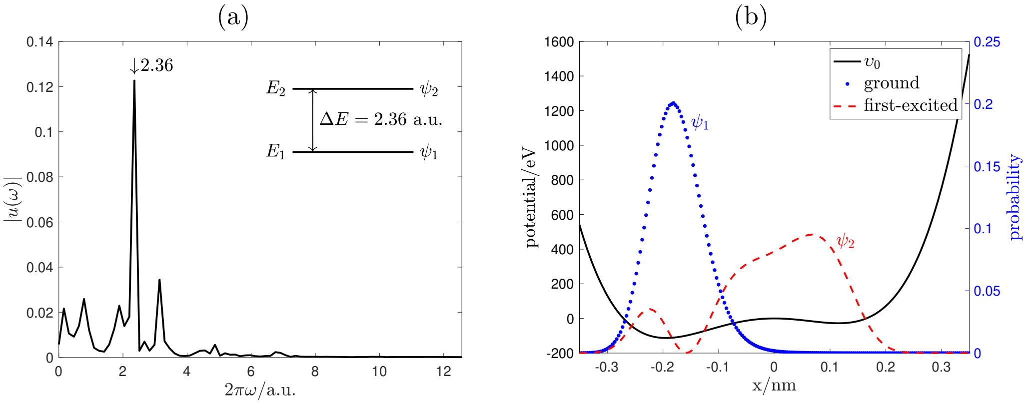

Figure 3.5: (a) Frequency spectrum of the optimal field for $T = 40$, which shows a prominent peak at $2\pi\omega = 2.36$ a.u., which corresponds to the energy difference ($\Delta E = E_2 - E_1$) between the first-excited and ground states. (b) Confining potential (solid black line), ground state (dotted blue line), and first-excited state (dashed red line).

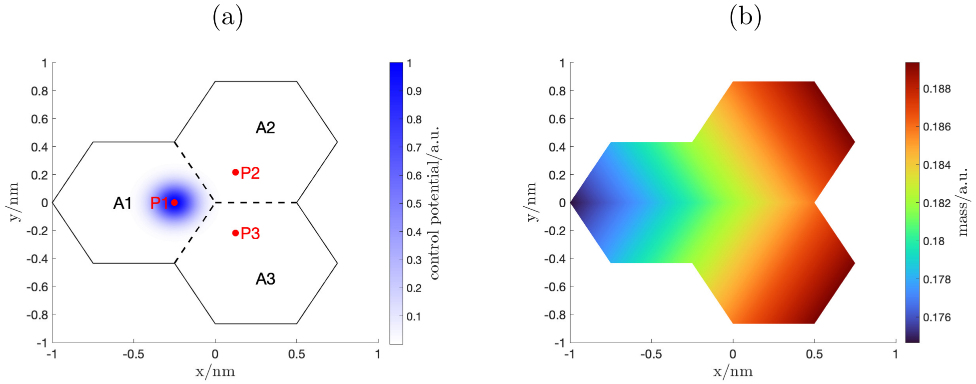

Figure 3.6: (a) Geometry of the domain consisting of three fused hexagons denoted by A1, A2, and A3. The control potential denoted by the blue color is localized around P1. (b) Plot of the varying effective mass across the geometric domain.

We consider a symmetric triple-well-confining potential, v_0, with its three minima located at points P1, P2, and P3, which takes the form:

$$v_0(x,y) = \min\left\{ \left(x+\frac{l}{2}\right)^2 + y^2, \left(x-\frac{l}{4}\right)^2 + \left(y+\frac{\sqrt{3}}{4}l\right)^2, \right. \\ \left. \left(x-\frac{l}{4}\right)^2 + \left(y-\frac{\sqrt{3}}{4}l\right)^2 \right\}, \tag{3.31}$$

which is depicted in Fig. 3.7a. With v_0 defined, we computed the eigenstates of the system and selected the ground state as the initial state, $\psi(0)$. Since the two A2 and A3 hexagons have a larger m^* compared to A1, the initial state $\psi(0)$ is not distributed symmetrically but is more localized near P2 and P3, as can be seen in Fig. 3.7b. The objective of this example is to construct a control field that steers electrons toward the left hexagon, A1. Consequently, the characteristic function χ is chosen as a step function (Eq. 3.32) with zeros in A1 and ones elsewhere.

$$\chi(x,y) = \begin{cases} 0 & (x,y) \in \text{A1} \\ 1 & \text{otherwise} \end{cases}. \tag{3.32}$$

The MATLAB code to set up this control problem is given below:

```
% for a nonregular polygon shape, we define the customized geometry
% in a separate .m file, and pass the filename to the variable
% geometry_customized_file and set the degree_of_polygon to 1.
degree_of_polygon = 1;
geometry_customized_file = 'geometry_customized';
vector_of_side_lengths = [0.5];
number_of_triangles = 4e4;
T = 40;
Nt = 1000;
% specify effective mass and permittivity
% as functions of the position in separate files
```

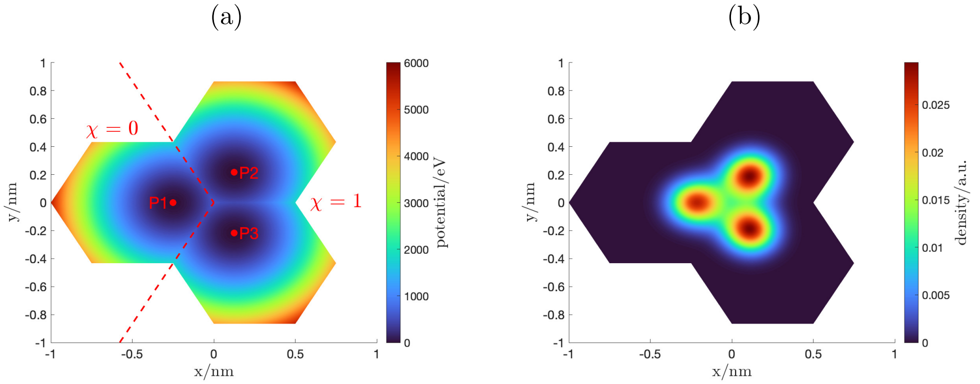

Figure 3.7: (a) Confining potential, υ_0 with its three minima located at points P1, P2, and P3. (b) Initial electron density, $\rho(0)$.

```
vector_of_masses = mass_customized( 1, x, y );
vector_of_eps = eps_customized( 1, x, y );
beta = 0; gam = 0; eta = 1; nu = 1e-4;
psi0 =  solve_initial_states();
psi_wgt = ones( size(psi0) )*2;
% l is the side length of the hexagon
V_ctr = @(x,y) [exp(-(x+l/2)^2/(l/30)).*exp(-y^2/(l/30))];
chi = (y>=-sqrt(3)*x) | (y<=sqrt(3)*x);
V_cst = min(  (x+l/2)^2+y^2;
(x-l/4)^2+(y+sqrt(3)/4*l)^2;
(x-l/4)^2+(y-sqrt(3)/4*l)^2)
```

The results from the QOC algorithm in MISTER-T are shown in Fig. 3.8, which shows the convergence of the loss functional, shape of the optimal control field, and final electron density distribution. Under the influence of the external field shown in Fig. 3.8b, the electrons are directed to the left hexagon, A1, at the end of the propagation. It is interesting to note that we obtain a high yield of 99.8%, even though the control field is only acting on the small region around P1. The video animation file in the Supplementary Material shows that the electron density shifts to the P1 center near the first half of the

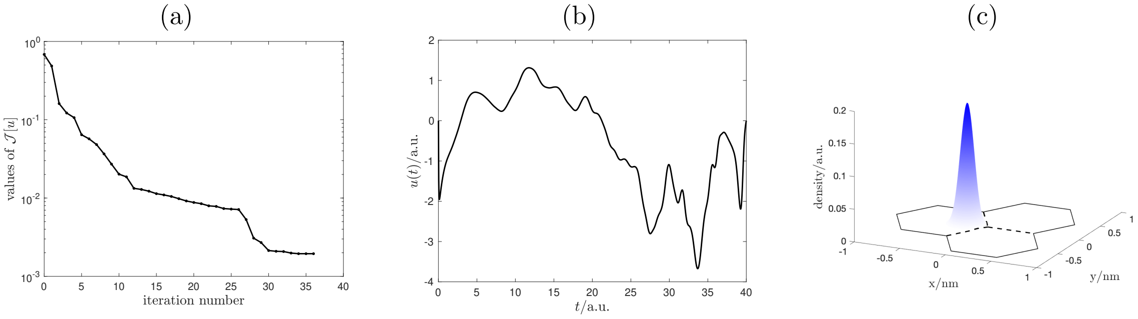

Figure 3.8: (a) Loss functional as a function of iteration number. (b) Converged optimal control, $u_{\text{opt}}(t)$, as a function of time. (c) Final electron density after time propagation.

simulation and remains there with small oscillatory movements in the second half (after $t = 25$ a.u.). Taken together, this example highlights the capabilities of the MISTER-T program for successfully handling a non-uniform mass distribution with an intricate geometry for controlling complex quantum systems. Furthermore, the high yield attained using the local control approach in this specific example suggests that the entire system can be effectively manipulated at one or a few localized regions, which has significant practical implications in manipulating electron dynamics in atoms/molecules and quantum devices.

3.6 Conclusions

In conclusion, we have constructed the user-friendly, open-source MISTER-T software package for carrying out quantum optimal control calculations of effective multi-electron systems on non-standard mesh grids with arbitrary two-dimensional cross-sectional geometries. The MISTER-T program uses a propagator integration to solve the forward and backward equations with a position-dependent mass and pseudoskeleton decomposition for enhanced computational efficiency. To demonstrate the versatility and reliability of our code, we explore various examples with varying geometries, mass distributions, confining potentials, control potentials, and loss functionals. We first tested the accuracy of the MISTER-T code against known numerical results, which allowed us to validate our new implementation. Next, we explored how varying the propagation duration for the same system gave distinct optimal solutions, leading to different control strategies. In our final example, we achieved quantum optimal control of the total electron density in a system characterized by a complex geometry and a nonuniform mass distribution. Taken together, these examples demonstrate the ability of the MISTER-T code to construct optimal control fields in multi-electron systems with non-regular grids, which are essential for confined systems or quantum nanodevices with complex geometries.

Chapter 4

Conclusion

This dissertation has been dedicated to the development of computational methods and numerical algorithms for the advanced calculation and control of quantum many-body systems in real space. This endeavor is grounded in the frameworks of Density Functional Theory (DFT) and Quantum Optimal Control (QOC).

Chapter 1 offers a concise yet thorough introduction to the Hartree-Fock formalism and the Kohn-Sham scheme within DFT, both of which are pivotal in solving the many-body Schrödinger equation. This chapter delineates the connections and distinctions between these two methodologies. Furthermore, it introduces QOC as a means to address the "inverse" problem in quantum systems: determining the external field necessary to achieve a specified target configuration.

In Chapter 2, we present a computational approach that integrates the exact nonlocal exchange operator into the calculation of ground-state properties of multi-shell nanowires with diverse cross-sectional shapes, utilizing the HF formalism. This chapter highlights several key examples that underscore the significance of the nonlocal exchange operator. Its influence on various aspects, such as electron occupancy numbers, energy eigenvalues, energy separations, and electron localization patterns, is critically examined. The inclusion of the nonlocal exchange effect in these calculations enriches our understanding of the interplay between material compositions, doping densities, and geometric shapes in determining electronic properties.

Chapter 3 describes a computational methodology designed to achieve optimal control over quantum many-body interacting systems. This method is applicable to nonstandard mesh grids and arbitrary cross-sectional geometries. Initially, we employ the Lagrangian multiplier method to derive an analytical expression for the gradient of the loss functional. To evolve wavefunctions forward and backward, a propagator integration method (Green's function) is implemented, incorporating the WKB approximation to accommodate spatially-varying effective electron mass. The chapter then proceeds to demonstrate the reliability and effectiveness of our proposed scheme through various examples. Of particular note is our exploration of the impact of different propagation times on control strategies and the feasibility of manipulating the entire system using localized control potentials.

Bibliography

[1] Piers Coleman. *Introduction to many-body physics.* Cambridge University Press, 2015.

[2] Gregg Jaeger. What in the (quantum) world is macroscopic? *American Journal of Physics*, 82(9):896–905, 2014.

[3] Pierre Hohenberg and Walter Kohn. Inhomogeneous electron gas. *Physical review*, 136(3B):B864, 1964.

[4] Wolfram Koch and Max C Holthausen. *A chemist's guide to density functional theory.* John Wiley & Sons, 2015.

[5] Walter Kohn and Lu Jeu Sham. Self-consistent equations including exchange and correlation effects. *Physical review*, 140(4A):A1133, 1965.

[6] Michael Christopher Gibson. *Implementation and application of advanced density functionals.* PhD thesis, Durham University, 2006.

[7] Jos Thijssen. *Computational physics.* Cambridge university press, 2007.

[8] Tjalling Koopmans. Über die zuordnung von wellenfunktionen und eigenwerten zu den einzelnen elektronen eines atoms. *physica*, 1(1-6):104–113, 1934.

[9] Christiane P Koch, Ugo Boscain, Tommaso Calarco, Gunther Dirr, Stefan Filipp, Steffen J Glaser, Ronnie Kosloff, Simone Montangero, Thomas Schulte-Herbrüggen, Dominique Sugny, et al. Quantum optimal control in quantum technologies. strategic report on current status, visions and goals for research in europe. *EPJ Quantum Technology*, 9(1):19, 2022.

[10] Alberto Castro, Jan Werschnik, and Eberhard KU Gross. Controlling the dynamics of many-electron systems from first principles: A combination of optimal control and time-dependent density-functional theory. *Physical review letters*, 109(15):153603, 2012.

[11] Alfio Borzì, Gabriele Ciaramella, and Martin Sprengel. *Formulation and numerical solution of quantum control problems.* SIAM, 2017.

[12] Yuan Chen, Simon N Sandhofer, and Bryan M Wong. Shoryuken: An open-source software package for calculating nonlocal exchange interactions in nanowires. *Computer Physics Communications*, 300:109197, 2024.

[13] Nitin Goyal, Benjamin Iñiguez, and Tor A Fjeldly. Analytical modeling of bare surface barrier height and charge density in algan/gan heterostructures. *Applied Physics Letters*, 101(10):103505, 2012.

[14] Umesh K Mishra, Primit Parikh, and Yi-Feng Wu. Algan/gan hemts-an overview of device operation and applications. *Proceedings of the IEEE*, 90(6):1022–1031, 2002.

[15] Siddharth Rajan, Patrick Waltereit, Christiane Poblenz, Sten J Heikman, Daniel S Green, James S Speck, and Umesh K Mishra. Power performance of algan-gan hemts grown on sic by plasma-assisted mbe. *IEEE Electron Device Letters*, 25(5):247–249, 2004.

[16] Chen Li, Yongfa Cheng, Bang Li, Feng Cheng, Luying Li, Tianyu Qi, Shuangfeng Jia, Xin Yan, Xia Zhang, Jianbo Wang, et al. Study of charge distributions and electrical properties in gaas/algaas single quantum well/nanowire heterostructures. *The Journal of Physical Chemistry C*, 123(44):26888–26894, 2019.

[17] Melodie Fickenscher, Teng Shi, Howard E Jackson, Leigh M Smith, Jan M Yarrison-Rice, Changlin Zheng, Peter Miller, Joanne Etheridge, Bryan M Wong, Qiang Gao, et al. Optical, structural, and numerical investigations of gaas/algaas core–multishell nanowire quantum well tubes. *Nano letters*, 13(3):1016–1022, 2013.

[18] Wei Lu, Jie Xiang, Brian P Timko, Yue Wu, and Charles M Lieber. One-dimensional hole gas in germanium/silicon nanowire heterostructures. *Proceedings of the National Academy of Sciences*, 102(29):10046–10051, 2005.

[19] Bryan M Wong, François Léonard, Qiming Li, and George T Wang. Nanoscale effects on heterojunction electron gases in gan/algan core/shell nanowires. *Nano letters*, 11(8):3074–3079, 2011.

[20] Lingquan Wang, Deli Wang, and Peter M Asbeck. A numerical schrödinger–poisson solver for radially symmetric nanowire core–shell structures. *Solid-state electronics*, 50(11-12):1732–1739, 2006.

[21] Andrea Bertoni, Miquel Royo, Farah Mahawish, and Guido Goldoni. Electron and hole gas in modulation-doped gaas/al 1- x ga x as radial heterojunctions. *Physical Review B*, 84(20):205323, 2011.

[22] Fredy W. Aquino and Bryan M. Wong. Additional insights between fermi–löwdin orbital sic and the localization equation constraints in sic-dft. *The Journal of Physical Chemistry Letters*, 9(22):6456–6462, 2018.

[23] Fredy W. Aquino, Ravindra Shinde, and Bryan M. Wong. Fractional occupation numbers and self-interaction correction-scaling methods with the fermi-löwdin orbital self-interaction correction approach. *Journal of Computational Chemistry*, 41(12):1200–1208, 2020.

[24] Ravindra Shinde, Sharma S R K C Yamijala, and Bryan M Wong. Improved band gaps and structural properties from wannier–fermi–löwdin self-interaction corrections for periodic systems. *Journal of Physics: Condensed Matter*, 33(11):115501, dec 2020.

[25] Michael E. Foster and Bryan M. Wong. Nonempirically tuned range-separated dft accurately predicts both fundamental and excitation gaps in dna and rna nucleobases. *Journal of Chemical Theory and Computation*, 8(8):2682–2687, 2012.

[26] Lindsey N. Anderson, M. Belén Oviedo, and Bryan M. Wong. Accurate electron affinities and orbital energies of anions from a nonempirically tuned range-separated density functional theory approach. *Journal of Chemical Theory and Computation*, 13(4):1656–1666, 2017.

[27] Bryan M. Wong and Joseph G. Cordaro. Coumarin dyes for dye-sensitized solar cells: A long-range-corrected density functional study. *The Journal of Chemical Physics*, 129(21):214703, 12 2008.

[28] Bryan M. Wong, Manuel Piacenza, and Fabio Della Sala. Absorption and fluorescence properties of oligothiophene biomarkers from long-range-corrected time-dependent density functional theory. *Phys. Chem. Chem. Phys.*, 11:4498–4508, 2009.

[29] Bryan M. Wong and Timothy H. Hsieh. Optoelectronic and excitonic properties of oligoacenes: Substantial improvements from range-separated time-dependent density functional theory. *Journal of Chemical Theory and Computation*, 6(12):3704–3712, 2010.

[30] Cameron Chevalier and Bryan M Wong. Hadoken: An open-source software package for predicting electron confinement effects in various nanowire geometries and configurations. *Computer Physics Communications*, 274:108299, 2022.

[31] Abhiraj Sharma and Phanish Suryanarayana. Real-space density functional theory adapted to cyclic and helical symmetry: application to torsional deformation of carbon nanotubes. *Physical Review B*, 103(3):035101, 2021.

[32] Swarnava Ghosh, Amartya S Banerjee, and Phanish Suryanarayana. Symmetry-adapted real-space density functional theory for cylindrical geometries: Application to large group-iv nanotubes. *Physical Review B*, 100(12):125143, 2019.

[33] Andrew W Long and Bryan M Wong. Pamela: An open-source software package for calculating nonlocal exact exchange effects on electron gases in core-shell nanowires. *AIP Advances*, 2(3):032173, 2012.

[34] Fang Qian, Yat Li, Silvija Gradečak, Deli Wang, Carl J. Barrelet, and Charles M. Lieber. Gallium nitride-based nanowire radial heterostructures for nanophotonics. *Nano Letters*, 4(10):1975–1979, 2004.

[35] Fang Qian, Silvija Gradečak, Yat Li, Cheng-Yen Wen, and Charles M. Lieber. Core/multishell nanowire heterostructures as multicolor, high-efficiency light-emitting diodes. *Nano Letters*, 5(11):2287–2291, 2005.

[36] Yat Li, Jie Xiang, Fang Qian, Silvija Gradečak, Yue Wu, Hao Yan, Douglas A. Blom, and Charles M. Lieber. Dopant-free GaN/AlN/AlGaN radial nanowire heterostructures as high electron mobility transistors. *Nano Letters*, 6(7):1468–1473, 2006.

[37] K. Hestroffer, R. Mata, D. Camacho, C. Leclere, G. Tourbot, Y. M. Niquet, A. Cros, C. Bougerol, H. Renevier, and B. Daudin. The structural properties of GaN/AlN core-shell nanocolumn heterostructures. *Nanotechnology*, 21(41):415702, 2010.

[38] Tevye Kuykendall, Peter J. Pauzauskie, Yanfeng Zhang, Joshua Goldberger, Donald Sirbuly, Jonathan Denlinger, and Peidong Yang. Crystallographic alignment of high-density gallium nitride nanowire arrays. *Nature Materials*, 3(8):524–528, 2004.

[39] George T. Wang, A. Alec Talin, Donald J. Werder, J. Randall Creighton, Elaine Lai, Richard J. Anderson, and Ilke Arslan. Highly aligned, template-free growth and characterization of vertical GaN nanowires on sapphire by metal–organic chemical vapour deposition. *Nanotechnology*, 17(23):5773–5780, 2006.

[40] Niklas Sköld, Lisa S. Karlsson, Magnus W. Larsson, Mats-Erik Pistol, Werner Seifert, Johanna Trägårdh, and Lars Samuelson. Growth and optical properties of strained GaAs–$\mathrm{Ga}_x\mathrm{In}_{1-x}\mathrm{P}$ core–shell nanowires. *Nano Letters*, 5(10):1943–1947, 2005.

[41] O. Hayden, A. B. Greytak, and D. C. Bell. Core–shell nanowire light-emitting diodes. *Advanced Materials*, 17(6):701–704, 2005.

[42] Attila Szabo and Neil S Ostlund. *Modern quantum chemistry: introduction to advanced electronic structure theory*. Courier Corporation, 2012.

[43] Leon van Dommelen. Quantum mechanics for engineers., 2012.

[44] L. R. Ram-Mohan. *Finite Element and Boundary Element Applications to Quantum Mechanics*. Oxford University Press, New York, first edition, 2002.

[45] Jeremy S Heyl and Anand Thirumalai. Pseudo-spectral methods for atoms in strong magnetic fields. *Monthly Notices of the Royal Astronomical Society*, 407(1):590–598, 2010.

[46] Phanish Suryanarayana, Vikram Gavini, Thomas Blesgen, Kaushik Bhattacharya, and Michael Ortiz. Non-periodic finite-element formulation of kohn–sham density functional theory. *Journal of the Mechanics and Physics of Solids*, 58(2):256–280, 2010.

[47] John E Pask, Barry M Klein, Philip A Sterne, and Chingyao Y Fong. Finite-element methods in electronic-structure theory. *Computer Physics Communications*, 135(1):1–34, 2001.

[48] Michael A Mastro, Blake Simpkins, George T Wang, Jennifer Hite, Charles R Eddy, Hong-Youl Kim, Jaehui Ahn, and Jihyun Kim. Polarization fields in iii-nitride nanowire devices. *Nanotechnology*, 21(14):145205, 2010.

[49] O Ambacher, J Smart, JR Shealy, NG Weimann, K Chu, M Murphy, WJ Schaff, LF Eastman, R Dimitrov, L Wittmer, et al. Two-dimensional electron gases induced by spontaneous and piezoelectric polarization charges in n-and ga-face algan/gan heterostructures. *Journal of applied physics*, 85(6):3222–3233, 1999.

[50] AE Romanov, TJ Baker, S Nakamura, JS Speck, and ERATO/JST UCSB Group. Strain-induced polarization in wurtzite iii-nitride semipolar layers. *Journal of Applied Physics*, 100(2):023522, 2006.

[51] Duanjun Cai and Guang-Yu Guo. Tuning linear and nonlinear optical properties of wurtzite gan by c-axial stress. *Journal of Physics D: Applied Physics*, 42(18):185107, 2009.

[52] Inc MathWorks. *Partial Differential Equation Toolbox for Use with MATLAB, COMSOL AB: User's Guide, Version 1.* The MathWorks, 2002.

[53] ET Yu, GJ Sullivan, PM Asbeck, CD Wang, D Qiao, and SS Lau. Measurement of piezoelectrically induced charge in gan/algan heterostructure field-effect transistors. *Applied Physics Letters*, 71(19):2794–2796, 1997.

[54] James Paul Ibbetson, PT Fini, KD Ness, SP DenBaars, JS Speck, and UK Mishra. Polarization effects, surface states, and the source of electrons in algan/gan heterostructure field effect transistors. *Applied Physics Letters*, 77(2):250–252, 2000.

[55] G Koley and MG Spencer. On the origin of the two-dimensional electron gas at the al ga n/ ga n heterostructure interface. *Applied Physics Letters*, 86(4):042107, 2005.

[56] Luke Gordon, Mao-Sheng Miao, Srabanti Chowdhury, Masataka Higashiwaki, Umesh K Mishra, and Chris G Van de Walle. Distributed surface donor states and the two-dimensional electron gas at algan/gan heterojunctions. *Journal of Physics D: Applied Physics*, 43(50):505501, 2010.

[57] Yuan Chen, Mahmut Sait Okyay, and Bryan M. Wong. Mister-t: An open-source software package for quantum optimal control of multi-electron systems on arbitrary geometries. *Computer Physics Communications*, 302:109248, 2024.

[58] Marcos Dantus and Vadim V Lozovoy. Experimental coherent laser control of physicochemical processes. *Chemical reviews*, 104(4):1813–1860, 2004.

[59] M Wollenhaupt, V Engel, and T Baumert. Femtosecond laser photoelectron spectroscopy on atoms and small molecules: Prototype studies in quantum control. *Annu. Rev. Phys. Chem.*, 56:25–56, 2005.

[60] Patrick Nuernberger, Gerhard Vogt, Tobias Brixner, and Gustav Gerber. Femtosecond quantum control of molecular dynamics in the condensed phase. *Physical Chemistry Chemical Physics*, 9(20):2470–2497, 2007.

[61] Malcolm H Levitt. *Spin dynamics: basics of nuclear magnetic resonance.* John Wiley & Sons, 2013.

[62] Arthur Schweiger and Gunnar Jeschke. *Principles of pulse electron paramagnetic resonance.* Oxford university press, 2001.

[63] Matt A Bernstein, Kevin F King, and Xiaohong Joe Zhou. *Handbook of MRI pulse sequences.* Elsevier, 2004.

[64] Xian Wang, Mahmut Sait Okyay, Anshuman Kumar, and Bryan M Wong. Accelerating quantum optimal control of multi-qubit systems with symmetry-based hamiltonian transformations. *AVS Quantum Science*, 5(4), 2023.

[65] Frank Verstraete, Michael M Wolf, and J Ignacio Cirac. Quantum computation and quantum-state engineering driven by dissipation. *Nature physics*, 5(9):633–636, 2009.

[66] Reinier W Heeres, Philip Reinhold, Nissim Ofek, Luigi Frunzio, Liang Jiang, Michel H Devoret, and Robert J Schoelkopf. Implementing a universal gate set on a logical qubit encoded in an oscillator. *Nature communications*, 8(1):94, 2017.

[67] Jianming Cai, Alex Retzker, Fedor Jelezko, and Martin B Plenio. A large-scale quantum simulator on a diamond surface at room temperature. *Nature Physics*, 9(3):168–173, 2013.

[68] Christian Kokail, Christine Maier, Rick van Bijnen, Tiff Brydges, Manoj K Joshi, Petar Jurcevic, Christine A Muschik, Pietro Silvi, Rainer Blatt, Christian F Roos, et al. Self-verifying variational quantum simulation of lattice models. *Nature*, 569(7756):355–360, 2019.

[69] Philipp Neumann, Ingmar Jakobi, Florian Dolde, Christian Burk, Rolf Reuter, Gerald Waldherr, Jan Honert, Thomas Wolf, Andreas Brunner, Jeong Hyun Shim, et al. High-precision nanoscale temperature sensing using single defects in diamond. *Nano letters*, 13(6):2738–2742, 2013.

[70] Philipp Konzelmann, Torsten Rendler, Ville Bergholm, Andrea Zappe, Veronika Pfannenstill, Marwa Garsi, Florestan Ziem, Matthias Niethammer, Matthias Widmann, Sang-Yun Lee, et al. Robust and efficient quantum optimal control of spin probes in a complex (biological) environment. towards sensing of fast temperature fluctuations. *New Journal of Physics*, 20(12):123013, 2018.

[71] Akber Raza, Chengkuan Hong, Xian Wang, Anshuman Kumar, Christian R. Shelton, and Bryan M. Wong. Nic-cage: An open-source software package for predicting optimal control fields in photo-excited chemical systems. *Computer Physics Communications*, 258:107541, 2021.

[72] Yuanqi Gao, Xian Wang, Nanpeng Yu, and Bryan M. Wong. Harnessing deep reinforcement learning to construct time-dependent optimal fields for quantum control dynamics. *Phys. Chem. Chem. Phys.*, 24:24012–24020, 2022.

[73] Marjuka F Lazin, Christian R Shelton, Simon N Sandhofer, and Bryan M Wong. High-dimensional multi-fidelity bayesian optimization for quantum control. *Machine Learning: Science and Technology*, 4(4):045014, oct 2023.

[74] José M. Rodríguez-Borbón, Xian Wang, Adrián P. Diéguez, Khaled Z. Ibrahim, and Bryan M. Wong. Travolta: Gpu acceleration and algorithmic improvements for constructing quantum optimal control fields in photo-excited systems. *Computer Physics Communications*, 296:109017, 2024.

[75] Steffen J Glaser, Ugo Boscain, Tommaso Calarco, Christiane P Koch, Walter Köckenberger, Ronnie Kosloff, Ilya Kuprov, Burkhard Luy, Sophie Schirmer, Thomas Schulte-Herbrüggen, et al. Training schrödinger's cat: Quantum optimal control: Strategic report on current status, visions and goals for research in europe. *The European Physical Journal D*, 69:1–24, 2015.

[76] Ugo Boscain, Mario Sigalotti, and Dominique Sugny. Introduction to the pontryagin maximum principle for quantum optimal control. *PRX Quantum*, 2(3):030203, 2021.

[77] Frank K Wilhelm, Susanna Kirchhoff, Shai Machnes, Nicolas Wittler, and Dominique Sugny. An introduction into optimal control for quantum technologies. *arXiv preprint arXiv:2003.10132*, 2020.

[78] Erich Runge and Eberhard KU Gross. Density-functional theory for time-dependent systems. *Physical review letters*, 52(12):997, 1984.

[79] Alberto Castro. Theoretical shaping of femtosecond laser pulses for ultrafast molecular photo-dissociation with control techniques based on time-dependent density functional theory. *ChemPhysChem*, 14(7):1488–1495, 2013.

[80] Wen-Hao Liu, Zhi Wang, Zhang-Hui Chen, Jun-Wei Luo, Shu-Shen Li, and Lin-Wang Wang. Algorithm advances and applications of time-dependent first-principles simulations for ultrafast dynamics. *Wiley Interdisciplinary Reviews: Computational Molecular Science*, 12(3):e1577, 2022.

[81] Alicia B Magann, Matthew D Grace, Herschel A Rabitz, and Mohan Sarovar. Digital quantum simulation of molecular dynamics and control. *Physical Review Research*, 3(2):023165, 2021.

[82] E Irani, A Anvari, and R Sadighi-Bonabi. Selective photo-dissociative ionization of methane molecule with tddft study. *Spectrochimica Acta Part A: Molecular and Biomolecular Spectroscopy*, 171:325–329, 2017.

[83] Maria Hellgren, Esa Räsänen, and EKU Gross. Optimal control of strong-field ionization with time-dependent density-functional theory. *Physical Review A*, 88(1):013414, 2013.

[84] Alberto Castro. Theoretical shaping of femtosecond laser pulses for molecular photodissociation with control techniques based on ehrenfest's dynamics and time-dependent density functional theory. *ChemPhysChem*, 17(11):1601–1607, 2016.

[85] Xavier Andrade, David Strubbe, Umberto De Giovannini, Ask Hjorth Larsen, Micael JT Oliveira, Joseba Alberdi-Rodriguez, Alejandro Varas, Iris Theophilou, Nicole Helbig, Matthieu J Verstraete, et al. Real-space grids and the octopus code as tools for the development of new simulation approaches for electronic systems. *Physical Chemistry Chemical Physics*, 17(47):31371–31396, 2015.

[86] S Rasti, E Irani, and R Sadighi-Bonabi. Efficient photo-dissociation of ch4 and h2co molecules with optimized ultra-short laser pulses. *AIP Advances*, 5(11), 2015.

[87] Tsuyoshi Kato, Katsuyuki Nobusada, and Shinji Saito. Inverse kohn–sham equations derived from the density equation theory. *Journal of the Physical Society of Japan*, 89(2):024301, 2020.

[88] R Vilela Mendes. Quantum control of quantum triple collisions in a maximally symmetric three-body coulomb problem. *International Journal of Modern Physics B*, page 2450143, 2023.

[89] A Putaja and E Räsänen. Ultrafast sequential charge transfer in a double quantum dot. *Physical Review B*, 82(16):165336, 2010.

[90] Esa Räsänen, Antti Putaja, and Yousof Mardoukhi. Optimal control strategies for coupled quantum dots. *Open Physics*, 11(9):1066–1073, 2013.

[91] Martin Sprengel, Gabriele Ciaramella, and Alfio Borzì. A cokosnut code for the control of the time-dependent kohn–sham model. *Computer Physics Communications*, 214:231–238, 2017.

[92] Lauri Lehtovaara, Ville Havu, and Martti Puska. All-electron time-dependent density functional theory with finite elements: Time-propagation approach. *The Journal of chemical physics*, 135(15), 2011.

[93] Gang Bao, Guanghui Hu, and Di Liu. Real-time adaptive finite element solution of time-dependent kohn–sham equation. *Journal of Computational Physics*, 281:743–758, 2015.

[94] Bikash Kanungo and Vikram Gavini. Real time time-dependent density functional theory using higher order finite-element methods. *Physical Review B*, 100(11):115148, 2019.

[95] Bikash Kanungo, Nelson D Rufus, and Vikram Gavini. Efficient all-electron time-dependent density functional theory calculations using an enriched finite element basis. *Journal of Chemical Theory and Computation*, 19(3):978–991, 2023.

[96] Miguel AL Marques and Eberhard KU Gross. Time-dependent density functional theory. In *A Primer in Density Functional Theory*. Springer, 2003.

[97] Olle Gunnarsson and Bengt I Lundqvist. Exchange and correlation in atoms, molecules, and solids by the spin-density-functional formalism. *Physical Review B*, 13(10):4274, 1976.

[98] Stephan Glutsch. *Excitons in low-dimensional semiconductors: theory numerical methods applications*, volume 141. Springer Science & Business Media, 2013.

[99] Carsten A Ullrich. Time-dependent density-functional theory beyond the adiabatic approximation: Insights from a two-electron model system. *The Journal of chemical physics*, 125(23), 2006.

[100] Daniel A Rehn. *Algorithms for Real-Time Time-Dependent Density Functional Theory and Calculation of Phase Diagrams for Two-Dimensional Phase-Change Materials*. Stanford University, 2018.

[101] Zeng-hui Yang and Carsten A Ullrich. Direct calculation of exciton binding energies with time-dependent density-functional theory. *Physical Review B*, 87(19):195204, 2013.

[102] Abdallah Qteish, Patrick Rinke, Matthias Scheffler, and Jörg Neugebauer. Exact-exchange-based quasiparticle energy calculations for the band gap, effective masses, and deformation potentials of scn. *Physical Review B*, 74(24):245208, 2006.

[103] Calvin Yi-Ping Chao and Shun Lien Chuang. Resonant tunneling of holes in the multiband effective-mass approximation. *Physical Review B*, 43(9):7027, 1991.

[104] Harshani Ovamini Wijewardane and Carsten A Ullrich. Real-time electron dynamics with exact-exchange time-dependent density-functional theory. *Physical review letters*, 100(5):056404, 2008.

[105] Harshani O Wijewardane and Carsten A Ullrich. Time-dependent kohn-sham theory with memory. *Physical review letters*, 95(8):086401, 2005.

[106] Johannes Flick, Michael Ruggenthaler, Heiko Appel, and Angel Rubio. Kohn–sham approach to quantum electrodynamical density-functional theory: Exact time-dependent effective potentials in real space. *Proceedings of the National Academy of Sciences*, 112(50):15285–15290, 2015.

[107] Hana Gil, Panagiota Papakonstantinou, Chang Ho Hyun, and Yongseok Oh. From homogeneous matter to finite nuclei: Role of the effective mass. *Physical Review C*, 99(6):064319, 2019.

[108] Anirban Bhattacharyya and R.J. Furnstahl. The kinetic energy density in kohn–sham density functional theory. *Nuclear Physics A*, 747(2):268–294, 2005.

[109] Florian G Eich, M Di Ventra, and G Vignale. Density-functional theory of thermoelectric phenomena. *Physical review letters*, 112(19):196401, 2014.

[110] Martin Sprengel, Gabriele Ciaramella, and Alfio Borzì. Investigation of optimal control problems governed by a time-dependent kohn-sham model. *Journal of Dynamical and Control Systems*, 24:657–679, 2018.

[111] Fredi Tröltzsch. *Optimal control of partial differential equations: theory, methods, and applications*, volume 112. American Mathematical Soc., 2010.

[112] Jiawei Chiu and Laurent Demanet. Sublinear randomized algorithms for skeleton decompositions. *SIAM Journal on Matrix Analysis and Applications*, 34(3):1361–1383, 2013.

[113] Björn Engquist and Lexing Ying. A fast directional algorithm for high frequency acoustic scattering in two dimensions. *Journal of Computational Physics*, 2009.

[114] Yijin Gao, Jay Mayfield, and Songting Luo. A second-order fast huygens sweeping method for time-dependent schrödinger equations with perfectly matched layers. *Journal of Scientific Computing*, 88:1–26, 2021.

[115] Alexander H Barnett, Jeremy Magland, and Ludvig af Klinteberg. A parallel nonuniform fast fourier transform library based on an "exponential of semicircle" kernel. *SIAM Journal on Scientific Computing*, 41(5):C479–C504, 2019.

[116] Alex H Barnett. Aliasing error of the kernel in the nonuniform fast fourier transform. *Applied and Computational Harmonic Analysis*, 51:1–16, 2021.

[117] William W Hager and Hongchao Zhang. A new conjugate gradient method with guaranteed descent and an efficient line search. *SIAM Journal on optimization*, 16(1):170–192, 2005.

[118] Lloyd N. Trefethen. *Spectral Methods in MATLAB*. Society for Industrial and Applied Mathematics, 2000.

[119] Peter J Olver. Complex analysis and conformal mapping. *University of Minnesota*, 806, 2017.

[120] Carl M Bender and Steven A Orszag. *Advanced mathematical methods for scientists and engineers I: Asymptotic methods and perturbation theory*, volume 1. Springer Science & Business Media, 1999.

[121] Sergei A Goreinov, Eugene E Tyrtyshnikov, and Nickolai L Zamarashkin. A theory of pseudoskeleton approximations. *Linear algebra and its applications*, 261(1-3):1–21, 1997.

[122] S. A. Goreinov, N. L. Zamarashkin, and E. E. Tyrtyshnikov. Pseudoskeleton approximations by matrices of maximal volume. *Mathematical Notes*, 62(4):515–519, 1997.

Appendix A

Derivation of the Two-Dimensional Schrödinger-Poisson Equations for Nanowire Systems

In this appendix, we give a detailed derivation of Eqs. 2.6, 2.7, and 2.8. We commence by writing the direct potential, $V_{\mathrm{D},j}(\mathbf{r}_i)$ (see Eq. 2.2), as:

$$V_{\mathrm{D},j}(\mathbf{r}_i) = \int \Psi_j^*(\mathbf{r}_j) G(\mathbf{r}_i, \mathbf{r}_j) \Psi_j(\mathbf{r}_j) \mathrm{d}^3\mathbf{r}_j. \tag{A.1}$$

Applying the $\nabla_i \cdot \varepsilon^*(\mathbf{r}_i)\nabla_i$ operator on both sides of the above equation gives:

$$\begin{aligned}\nabla_i \cdot \varepsilon^*(\mathbf{r}_i)\nabla_i V_{\mathrm{D},j}(\mathbf{r}_i) &= \int \Psi_j^*(\mathbf{r}_j)\left[\nabla_i \cdot \varepsilon^*(\mathbf{r}_i)\nabla_i G(\mathbf{r}_i,\mathbf{r}_j)\right]\Psi_j(\mathbf{r}_j)\mathrm{d}^3\mathbf{r}_j \\ &= -\frac{e^2}{\varepsilon_0}\int \Psi_j^*(\mathbf{r}_j)\delta(\mathbf{r}_i-\mathbf{r}_j)\Psi_j(\mathbf{r}_j)\mathrm{d}^3\mathbf{r}_j \\ &= -\frac{e^2}{\varepsilon_0}\left|\Psi_j(\mathbf{r}_i)\right|^2,\end{aligned} \tag{A.2}$$

where we have used Eq. 2.3 in the second line. Next, substituting the wavefunction in Eq. 2.5 into Eq. A.2 gives:

$$\nabla_i \cdot \varepsilon^*(\mathbf{r}_i)\nabla_i V_{\mathrm{D},j}(\mathbf{r}_i) = -\frac{1}{L}\frac{e^2}{\varepsilon_0}\left|\psi_{n_j}(x_i,y_i)\right|^2. \tag{A.3}$$

Due to the translational invariance of the nanowire, $\varepsilon^*(\mathbf{r}_i)$ and $V_{\mathrm{D},j}(\mathbf{r}_i)$ do not depend on z_i, and the above equation can be re-written as a function of only x_i and y_i:

$$\nabla_{x_i,y_i} \cdot \varepsilon^*(x_i,y_i)\nabla_{x_i,y_i} V_{\mathrm{D},j}(x_i,y_i) = -\frac{1}{L}\frac{e^2}{\varepsilon_0}\left|\psi_{n_j}(x_i,y_i)\right|^2. \tag{A.4}$$

where ∇_{x_i,y_i} is the two-dimensional gradient operator. From Eq. 2.4, the exchange potential is written as:

$$V_{\mathrm{EXX},j}(\mathbf{r}_i) = \int \Psi_j^*(\mathbf{r}_j)G(\mathbf{r}_i,\mathbf{r}_j)\Psi_i(\mathbf{r}_j)\mathrm{d}^3\mathbf{r}_j. \tag{A.5}$$

Applying the $\nabla_i \cdot \varepsilon^*(\mathbf{r}_i)\nabla_i$ operator on the both sides of Eq. A.5 gives:

$$\begin{aligned}
\nabla_i \cdot \varepsilon^*(\mathbf{r}_i)\nabla_i V_{\mathrm{EXX},j}(\mathbf{r}_i) &= \int \Psi_j^*(\mathbf{r}_j)\left[\nabla_i \cdot \varepsilon^*(\mathbf{r}_i)\nabla_i G(\mathbf{r}_i,\mathbf{r}_j)\right]\Psi_i(\mathbf{r}_j)\mathrm{d}^3\mathbf{r}_j \\
&= -\frac{e^2}{\varepsilon_0}\int \Psi_j^*(\mathbf{r}_j)\delta(\mathbf{r}_i-\mathbf{r}_j)\Psi_i(\mathbf{r}_j)\mathrm{d}^3\mathbf{r}_j \\
&= -\frac{e^2}{\varepsilon_0}\Psi_j^*(\mathbf{r}_i)\Psi_i(\mathbf{r}_i) \\
&= -\frac{1}{L}\frac{e^2}{\varepsilon_0}\psi_{n_j}^*(x_i,y_i)\psi_{n_i}(x_i,y_i)e^{iz_i(k_i-k_j)},
\end{aligned} \tag{A.6}$$

where we have used Eq. 2.3 in the second line and Eq. 2.5 in the last line. Restricting our attention to electronic properties at the Gamma point (i.e., $k = 0$) gives:

$$\nabla_i \cdot \varepsilon^*(\mathbf{r}_i)\nabla_i V_{\mathrm{EXX},j}(\mathbf{r}_i) = -\frac{1}{L}\frac{e^2}{\varepsilon_0}\psi_{n_j}^*(x_i,y_i)\psi_{n_i}(x_i,y_i). \tag{A.7}$$

Since $\varepsilon^*(\mathbf{r}_i)$ and $V_{\mathrm{EXX},j}(\mathbf{r}_i)$ are invariant under translation along the z-axis of the nanowire, the above equation reduces to:

$$\nabla_{x_i,y_i} \cdot \varepsilon^*(x_i,y_i)\nabla_{x_i,y_i} V_{\mathrm{EXX},j}(x_i,y_i) = -\frac{1}{L}\frac{e^2}{\varepsilon_0}\psi_{n_j}^*(x_i,y_i)\psi_{n_i}(x_i,y_i). \tag{A.8}$$

For a nanowire with translational symmetry, Eq. 2.1 can be simplified to a two-dimensional form. Substituting Eq. 2.5 into Eq. 2.1 and noting that $m^*(\mathbf{r}_i)$ does not depend on z_i gives:

$$\begin{aligned}&\Bigg[-\frac{\hbar^2}{2}\nabla_{x_i,y_i}\cdot\frac{1}{m^*(x_i,y_i)}\nabla_{x_i,y_i}+\frac{\hbar^2k_i^2}{2m^*(x_i,y_i)}+V_{\mathrm{n}}(\mathbf{r}_i)+V_{\mathrm{CB}}(\mathbf{r}_i)\\&+2\sum_{j=1}^{N}V_{\mathrm{D},j}(\mathbf{r}_i)\Bigg]e^{ik_iz_i}\psi_{n_i}(x_i,y_i)-\sum_{j=1}^{N}V_{\mathrm{EXX},j}(\mathbf{r}_i)e^{ik_jz_i}\psi_{n_j}(x_i,y_i)=E_ie^{ik_iz_i}\psi_{n_i}(x_i,y_i).\end{aligned}\tag{A.9}$$

Note that the following definition of the exchange operator has been applied in Eq. A.9:

$$\hat{V}_{\mathrm{EXX},j}(\mathbf{r}_i)\Psi_i(\mathbf{r}_i)=\int\Psi_j^*(\mathbf{r}_j)G(\mathbf{r}_i,\mathbf{r}_j)\Psi_i(\mathbf{r}_j)\Psi_j(\mathbf{r}_i)\mathrm{d}^3\mathbf{r}_j.\tag{A.10}$$

Invoking translational invariance along the z-axis of the nanowire and restricting our calculations to the Gamma point gives the following two-dimensional equation for the wavefunction $\psi_{n_i}(x_i,y_i)$:

$$\begin{aligned}&\left[-\frac{\hbar^2}{2}\nabla_{x_i,y_i}\cdot\frac{1}{m^*(x_i,y_i)}\nabla_{x_i,y_i}+V_{\mathrm{n}}(x_i,y_i)+V_{\mathrm{CB}}(x_i,y_i)\right]\psi_{n_i}(x_i,y_i)\\&+2\sum_{j=1}^{N}V_{\mathrm{D},j}(x_i,y_i)\psi_{n_i}(x_i,y_i)-\sum_{j=1}^{N}V_{\mathrm{EXX},j}(x_i,y_i)\psi_{n_j}(x_i,y_i)=\epsilon_i\psi_{n_i}(x_i,y_i),\end{aligned}\tag{A.11}$$

where ϵ_i is the eigenenergy for the cross-sectional wavefunction, $\psi_{n_i}(x_i,y_i)$.

Note that the summation over j in Eq. A.11 runs over the quantum numbers for the three-dimensional wavefunction, $\Psi_i(\mathbf{r}_i)$, and can be further decomposed into two summations as follows:

$$\left[-\frac{\hbar^2}{2}\nabla_{x_i,\,y_i}\cdot\frac{1}{m^*(x_i,y_i)}\nabla_{x_i,\,y_i}+V_n(x_i,y_i)+V_{\mathrm{CB}}(x_i,y_i)\right]\psi_{n_i}(x_i,y_i)$$
$$+2\sum_{n_j}\sum_{n_{z_j}}V_{\mathrm{D},\,j}(x_i,y_i)\;\psi_{n_i}(x_i,y_i)\;-\sum_{n_j}\sum_{n_{z_j}}V_{\mathrm{EXX},\,j}(x_i,y_i)\;\psi_{n_j}(x_i,y_i)\;=\epsilon_i\,\psi_{n_i}(x_i,y_i),\tag{A.12}$$

where n_{z_j} and n_j are the quantum numbers associated with the wavefunction along the z-axis and the xy-plane, respectively. Eq. A.12 can be written more succinctly as

$$\begin{aligned}&\left[-\frac{\hbar^2}{2}\nabla_{x_i,\,y_i}\cdot\frac{1}{m^*(x_i,y_i)}\nabla_{x_i,\,y_i}+V_n(x_i,y_i)+V_{\mathrm{CB}}(x_i,y_i)\right]\psi_{n_i}(x_i,y_i)\\&+2\sum_{n_j}V_{\mathrm{D},\,n_j}(x_i,y_i)\;\psi_{n_i}(x_i,y_i)\;-\sum_{n_j}V_{\mathrm{EXX},\,n_j}(x_i,y_i)\;\psi_{n_j}(x_i,y_i)\;=\epsilon_i\,\psi_{n_i}(x_i,y_i),\end{aligned}\tag{A.13}$$

where we have defined the following two quantities:

$$V_{\mathrm{D},n_j}(x_i,y_i)=\sum_{n_{z_j}}V_{\mathrm{D},j}(x_i,y_i),\tag{A.14}$$

and

$$V_{\mathrm{EXX},n_j}(x_i,y_i)=\sum_{n_{z_j}}V_{\mathrm{EXX},j}(x_i,y_i).\tag{A.15}$$

Since the electron has a continuous energy spectrum for motion along the nanowire axis, the sum over n_{z_j} can be rewritten as a continuous integral. Applying the $\nabla_{x_i,y_i}\cdot\varepsilon^*(x_i,y_i)\nabla_{x_i,y_i}$ operator on the both sides of Eq. A.14 , the direct term, $V_{\mathrm{D},n_j}(x_i,y_i)$, satisfies the following equation:

$$\begin{aligned}\nabla_{x_i,y_i}\cdot\varepsilon^*(x_i,y_i)\nabla_{x_i,y_i}V_{\mathrm{D},n_j}(x_i,y_i) &= \sum_{n_{z_j}}\nabla_{x_i,y_i}\cdot\varepsilon^*(x_i,y_i)\nabla_{x_i,y_i}V_{\mathrm{D},j}(x_i,y_i)\\ &= -\frac{1}{L}\frac{e^2}{\varepsilon_0}\int dn_{z_j}\left|\psi_{n_j}(x_i,y_i)\right|^2,\end{aligned} \tag{A.16}$$

where we have used Eq. A.4 in the last line. Using the relation $k_{z_j} = 2\pi n_{z_j}/L$, Eq. A.16 can be converted to an integral over k_{z_j} in momentum-space:

$$\nabla_{x_i,y_i}\cdot\varepsilon^*(x_i,y_i)\nabla_{x_i,y_i}V_{\mathrm{D},n_j}(x_i,y_i) = -\frac{1}{2\pi}\frac{e^2}{\varepsilon_0}\int dk_{z_j}\left|\psi_{n_j}(x_i,y_i)\right|^2 \tag{A.17}$$

Applying the Fermi distribution at $T = 0$ K with the relations $E_j = E_{z_j} + \epsilon_j$, $E_{z_j} = \hbar^2 k_{z_j}^2/2m^*$, and $dk_{z_j} = \sqrt{m^*/2\hbar^2 E_{z_j}}\,\mathrm{d}E_{z_j}$ gives

$$\begin{aligned}&\nabla_{x_i,y_i}\cdot\varepsilon^*(x_i,y_i)\nabla_{x_i,y_i}V_{\mathrm{D},n_j}(x_i,y_i)\\ &= -\frac{1}{2\pi}\frac{e^2}{\varepsilon_0}\int_0^\infty \mathrm{d}E_{z_j}\sqrt{\frac{m^*(x_i,y_i)}{2\hbar^2 E_{z_j}}}\,\left|\psi_{n_j}(x_i,y_i)\right|^2\,\Theta(E_F - E_{z_j} - \epsilon_j),\end{aligned} \tag{A.18}$$

where E_F is the Fermi level of the system, and Θ is the Heaviside step function, which causes the integrand in Eq. A.18 to be nonzero when $E_{z_j} < E_F - E_{n_j}$, resulting in

$$\nabla_{x_i,y_i}\cdot\varepsilon^*(x_i,y_i)\nabla_{x_i,y_i}V_{\mathrm{D},n_j}(x_i,y_i) = -\frac{1}{\pi\hbar}\frac{e^2}{\varepsilon_0}\sqrt{\frac{m^*(x_i,y_i)(E_F-\epsilon_j)}{2}}\,\left|\psi_{n_j}(x_i,y_i)\right|^2. \tag{A.19}$$

Following the same procedure described above, it can be shown that the exchange interaction, $V_{\mathrm{EXX},n_j}(x_i, y_i)$, satisfies the following Poisson-like equation:

$$\nabla_{x_i,y_i} \cdot \varepsilon^*(x_i, y_i)\nabla_{x_i,y_i} V_{\mathrm{EXX},n_j}(x_i, y_i) = -\frac{1}{\pi\hbar}\frac{e^2}{\varepsilon_0}\sqrt{\frac{m^*(x_i, y_i)(E_F - \epsilon_j)}{2}}\; \psi^*_{n_j}(x_i, y_i)\psi_{n_i}(x_i, y_i). \tag{A.20}$$

Finally, the expression for the electron density, $n_\mathrm{e}(x, y)$, can be derived as follows:

$$\begin{aligned} n_\mathrm{e}(x, y) &= 2\sum_i |\Psi_i(\mathbf{r}_i)|^2 \Theta(E_F - E_{z_i} - \epsilon_i) \\ &= 2\sum_{n_i}\sum_{n_{z_i}} |\Psi_i(\mathbf{r}_i)|^2 \Theta(E_F - E_{z_i} - \epsilon_i) \\ &= \frac{2}{L}\sum_{n_i} |\psi_{n_i}(x_i, y_i)|^2 \int \mathrm{d}n_{z_i} \Theta(E_F - E_{z_i} - \epsilon_i) \\ &= \frac{1}{\pi\hbar}\sum_{n_i} |\psi_{n_i}(x_i, y_i)|^2 \sqrt{2m^*(x_i, y_i)(E_F - \epsilon_i)}, \end{aligned} \tag{A.21}$$

where we have applied similar techniques as those used to derive Eq. A.19.

Appendix B

Comparison of Numerical Methods for Computing Nonlocal Exchange

In this appendix, we compare the speed and memory usage of numerical methods used to calculate the nonlocal exchange terms given by Eqs. 2.14 and 2.24. The solution of Eq. 2.24 results in a system of linear equations having the form:

$$\mathbf{A}\mathbf{X} = \mathbf{B}, \tag{B.1}$$

where $\mathbf{A}$ and $\mathbf{B}$ are $N_p \times N_p$ sparse matrices. One numerical approach is to first compute the inverse of $\mathbf{A}$ and then multiply with $\mathbf{B}$ (i.e., $\mathbf{A}^{-1}\mathbf{B}$), which requires the pre-computation and storage of $\mathbf{A}^{-1}$. Another alternative is to use the built-in `mldivide` function or backslash operation ($\mathbf{A}\backslash\mathbf{B}$) in MATLAB, which does not explicitly require the computation of the matrix inverse, $\mathbf{A}^{-1}$. To compare the time and memory usage in both approaches, we ran a few performance tests with different matrix sizes, shown in Table B.1. Despite $\mathbf{A}$ and $\mathbf{B}$

being sparse, the solution vector, $\mathbf{X}$, is typically dense. The storage cost of $\mathbf{X}$ is the same for both options and is not included in Table B.1. Our comparison shows that the direct inversion method with $\mathbf{A}^{-1}$ precomputed is an order of magnitude faster than the backslash operator. It is worth noting that the overhead time for computing $\mathbf{A}^{-1}$ is typically on the order of the time cost of the backslash operator $\mathbf{A}\backslash\mathbf{B}$. In scenarios requiring repeated solutions of Eq. B.1 where $\mathbf{A}$ does not change between iterations, precomputing $\mathbf{A}^{-1}$ is advantageous in terms of total computational time. However, this method incurs extra memory usage due to the storing of $\mathbf{A}^{-1}$, which is comparable to the storage required for $\mathbf{X}$. Considering the trade-offs between computational efficiency and memory requirements, the SHORYUKEN code employs the direct inversion method to take advantage of its superior speed. This decision was also informed by the relatively modest memory demands of our SHORYUKEN code, which are well within the capabilities of modern computing platforms. C.3 gives a more detailed discussion of the memory footprint of the SHORYUKEN code.

	$\mathbf{A}^{-1}\mathbf{B}$			$\mathbf{A}\backslash\mathbf{B}$		
N_p	2,500	5,000	10,000	2,500	5,000	10,000
Overhead time (s)	6.5	51.0	424.6	0	0	0
Overhead memory (MB)	120.8	381.5	1,528	0	0	0
Time per iteration (s)	0.7	5.9	42.3	6.0	51.9	452.3

Table B.1: Comparison of time and memory usage between the direct inversion method vs. the backslash operator for solving a system of linear equations with various matrix sizes, N_p.

Appendix C

Computational Performance of the SHORYUKEN Code

In this appendix, we examine the performance of the SHORYUKEN code, focusing on its convergence, accuracy, and scalability in execution time and memory usage.

C.1 Convergence and Accuracy

As our first test, we examine the convergence of the self-consistent Fermi level energy as a function of mesh size, h. Figure C.1 plots the error in the Fermi level as a function of mesh size for various doping densities. In the plot, we define the error as $\left|E_F^h - E_F^0\right|$, where E_F^h is the Fermi level energy computed with mesh size h, and E_F^0 denotes the benchmark value obtained with $h = 0.6$ nm. Figure C.1 shows a consistent convergence as the mesh size decreases. Fitting $\left|E_F^h - E_F^0\right|$ vs. h to a quadratic function gives an R^2

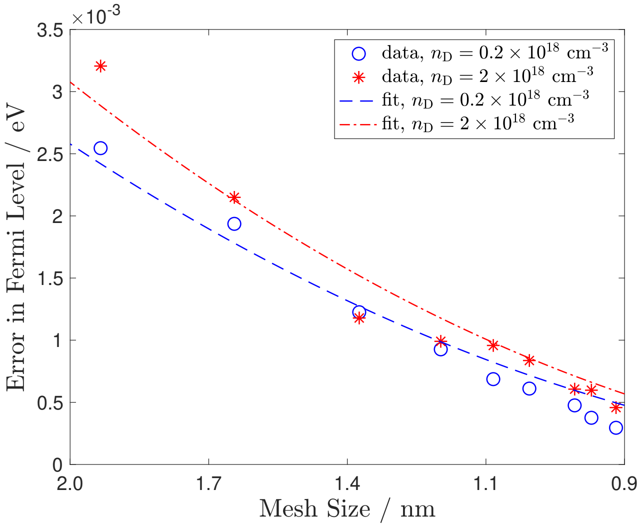

Figure C.1: Convergence of the self-consistent Fermi level energy as a function of mesh size h.

value of 0.966 ($n_\mathrm{D} = 0.2 \times 10^{18}$ cm^{-3}) and 0.955 ($n_\mathrm{D} = 2 \times 10^{18}$ cm^{-3}), which agrees with the quadratic convergence rate typically obtained with DFT methods [46].

To validate the accuracy of our code, we compared results from the SHORYUKEN finite element code against representative calculations obtained from the PAMELA code, which utilizes a pseudospectral approach [33]. Pseudospectral methods are extremely accurate approaches for numerically solving partial differential equations and computing integrals [118] and, therefore, serve as good benchmarks to test the convergence and accuracy of the SHORYUKEN finite element code. Since the PAMELA code can only simulate cylindrical core-shell nanowires, we studied the same geometries in the SHORYUKEN code to allow for a direct comparison. Specifically, we modeled a cylindrical core-shell nanowire with a core radius of $c = 20$ nm, a total shell radius of $s = 40$ nm, and a doping density of $n_\mathrm{D} = 0.15 \times 10^{18}$ cm^{-3}. The computed Fermi level energy and eigenenergies of the occupied wavefunctions for both codes are summarized in Table C.1. We observe an excellent agreement between the SHORYUKEN and PAMELA results, with a ~ 1 meV energy difference in the self-consistent Fermi level energy. Similarly, the eigenenergies exhibit a consistent double degeneracy pattern among many wavefunctions (notably, E2/E3, E4/E5, and E6/E7), with the overall difference of eigenenergies around 1 meV, which validates the accuracy of the SHORYUKEN code.

	E_F	E_1	E_2	E_3	E_4	E_5	E_6	E_7
PAMELA	-0.3839	-0.4184	-0.4154	-0.4154	-0.4069	-0.4069	-0.3930	-0.3930
SHORYUKEN (this work)	-0.3848	-0.4189	-0.4159	-0.4159	-0.4077	-0.4077	-0.3943	-0.3943

Table C.1: Comparison of self-consistent Fermi level energies and eigenvalues (eV) obtained from the PAMELA and SHORYUKEN codes.

C.2 Time Scaling Benchmarks

We carried out a detailed analysis to assess how the computational time scales with the number of finite elements. We explored system sizes ranging from 2,000 to 20,000 elements for hexagonal and both Ga-face/N-face triangular nanowires. Figure C.2a illustrates the wall time required per self-consistent field (SCF) iteration as a function of the finite element count N. Fitting the data to a power law gives scalings of $N^{1.79}$, $N^{1.84}$, and $N^{2.17}$ for hexagonal, Ga-face, and N-face triangular nanowires, respectively. Previous studies by Kaushik et al. [46] suggested a linear time complexity for solving the generalized eigenvalue problem using the finite element method. The computational expense of the SHORYUKEN code exceeds linear scaling due to the inclusion of the nonlocal exchange operator, which introduces additional computational complexity. Unlike local potentials, where the Hamiltonian matrix $\mathbf{H}$ remains sparse with a bandwidth independent of N, the nonlocal exchange potential results in a generally dense Hamiltonian matrix due to the nonlocal exchange term in Eq. 2.33, which results in a superlinear scaling behavior. For practical purposes, selecting $N = 10,000$ finite elements is typically adequate, yielding total wall times ranging from tens of minutes to several hours. However, employing a larger number of elements ($> 20,000$) requires significantly more time, scaling quadratically with the mesh size.

Fig. C.2b depicts the computational time used by each part of the code. The most expensive operation is the `sptarn` MATLAB built-in function, which solves the generalized eigenvalue problem (Eq. 2.33). This is due to the dense nature of the eigenvalue equation and the need to invoke `sptarn` multiple times per iteration to calculate the wavefunction and Fermi level. The second-most costly function arises from the `assem_pde` function in which the matrix form of the exchange operator on the finite element basis is constructed according to Eq. 2.33, which involves the multiplication of dense matrices. The remainder of the computational time, constituting about 10%, is distributed among other less-intensive numerical routines.

C.3 Memory Scaling Benchmarks

This section gives further details into the memory requirements associated with the number of finite elements used in the hexagonal and Ga-face/N-face triangular nanowire simulations. We define "memory" as the aggregate memory consumption of all variables within the code. Fig. C.3a, depicts a quadratic scaling for all three types of nanowires,

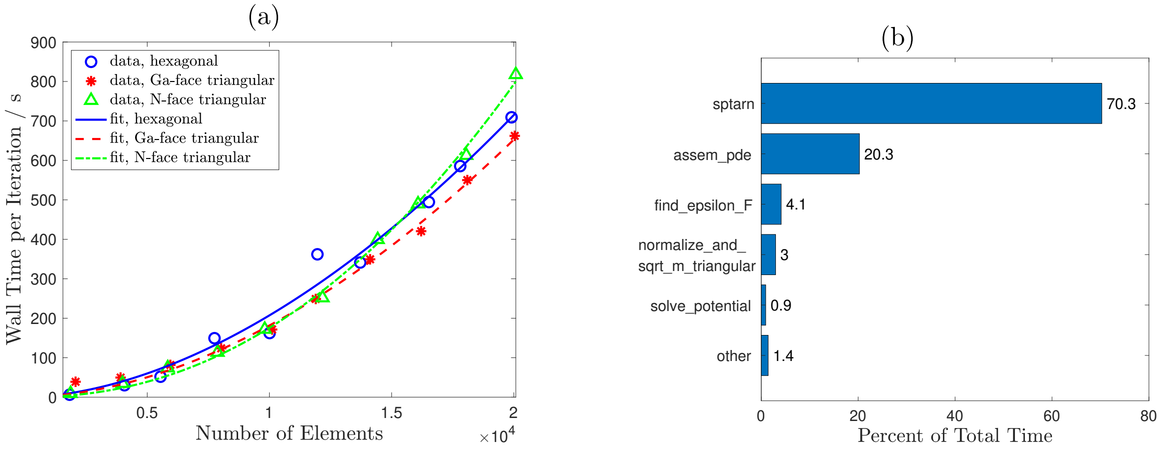

Figure C.2: (a) Scaling of wall time per iteration as a function of the number of elements N. (b) Percent of total computational time for each part of the SHORYUKEN code for a hexagonal nanowire with $N = 10,000$, $c = 30$ nm, $s = 50$ nm, and $n_\mathrm{D} = 1 \times 10^{18}\mathrm{cm}^{-3}$.

which is anticipated due to the prevalence of dense matrices in memory. Notably, for $N = 10,000$, the memory demand ranges between 1 and 2 GB, a requirement easily met by contemporary computing resources.

Further insights into specific memory allocations are provided in Fig. C.3b, which highlights the variables that significantly contribute to the overall memory usage. The `K_inv` and `HH` variables emerge as the largest memory consumers. Specifically, `K_inv` calculates the inverse of the Laplacian-like operator within the finite element framework (Eq. 2.25), and `HH` corresponds to the Hamiltonian matrix (cf. Eq. 2.33), which is integral to the `sptarn` function calls. Additional variables, namely `V_ex`, `V_ex_old`, and `M_ele`, also occupy large memory portions. These variables play crucial roles in the `assem_pde` function. The variable `V_ex` stores the nonlocal exchange operator on the finite element basis (cf. Eq. 2.33) and is used to construct the final Hamiltonian `HH`. The variable `V_ex_old` holds the

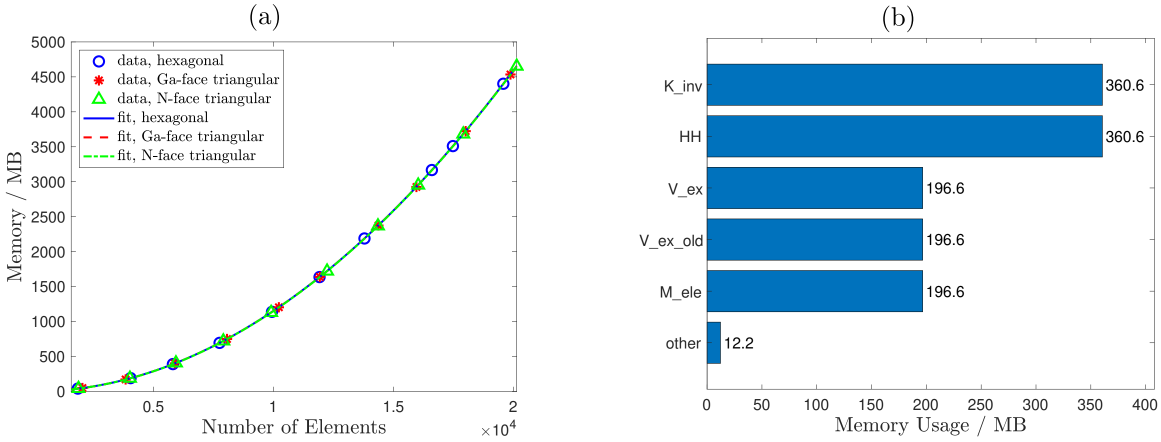

Figure C.3: (a) Scaling of memory usage as a function of the number of finite elements N. (b) Memory usage of various variables of the SHORYUKEN code using $N = 10,000$, which runs on a hexagonal nanowire with $c = 30$ nm, $s = 50$ nm, and $n_\mathrm{D} = 1 \times 10^{18}\mathrm{cm}^{-3}$.

old `V_ex` from the previous iteration, which is used to update the exchange potential in the current iteration. The variable `M_ele` serves an auxiliary purpose during the computation. All of these variables are dense matrices needed to build the nonlocal exchange and final Hamiltonian. The dense representations of the nonlocal exchange operator and Hamiltonian are attributed to the inherent nonlocal nature of exact exchange. Despite the large memory allocations for these dense matrices, the overall memory footprint does not present a substantial challenge for executing the SHORYUKEN code across most systems on modern computational platforms.

Appendix D

Green's Identity

Several equations in the main text can be reduced using Green's identity, which we briefly summarize here for convenience. Given scalar functions $f(r)$, $g(r)$, and $h(r)$, we can define the function, Z:

$$\begin{aligned} Z &= \int_\Omega -\left(\nabla \cdot f\, \nabla g\right) h \;\mathrm{d}^n r \\ &= \int_\Omega (-f\, h)\, \nabla^2 g \;\mathrm{d}^n r - \int_\Omega h \left(\nabla f \cdot \nabla g\right) \mathrm{d}^n r, \end{aligned} \tag{D.1}$$

where f, g, and h are scalar functions of r. For scalar functions ϕ and ψ, Green's first identity gives:

$$\int_\Omega -(\phi \nabla^2 \psi)\;\mathrm{d}^n r = \int_\Omega (\nabla \phi \cdot \nabla \psi)\;\mathrm{d}^n r - \oint_{\partial\Omega} (\phi\, \nabla \psi)\;\mathrm{d}^{n-1} r, \tag{D.2}$$

where the integral over $\partial\Omega$ is the integral over the boundary of the domain Ω. Substituting Eq. D.2 into Eq. D.1 gives:

$$Z = \int_\Omega (\nabla(f\,h) \cdot \nabla g)\ \mathrm{d}^n r - \oint_{\partial\Omega} (f\,h)\,\nabla g\ \mathrm{d}^{n-1} r - \int_\Omega h\,(\nabla f \cdot \nabla g)\ \mathrm{d}^n r. \tag{D.3}$$

Expanding $\nabla(f\,h)$ gives:

$$\begin{aligned} Z &= \int_\Omega f\,(\nabla h \cdot \nabla g)\ \mathrm{d}^n r + \int_\Omega h\,(\nabla f \cdot \nabla g)\ \mathrm{d}^n r - \oint_{\partial\Omega} (f\,h)\nabla g\ \mathrm{d}^{n-1} r - \int_\Omega h\,(\nabla f \cdot \nabla g)\ \mathrm{d}^n r \\ &= \int_\Omega f\,(\nabla h \cdot \nabla g)\ \mathrm{d}^n r - \oint_{\partial\Omega} (f\,h)\nabla g\ \mathrm{d}^{n-1} r. \end{aligned} \tag{D.4}$$

If f, h, or ∇g is zero for the entirety of the domain boundary, the boundary integral vanishes, giving the relation:

$$\int_\Omega -\,(\nabla \cdot f\,\nabla g)\,h\ \mathrm{d}^n r = \int_\Omega f\,(\nabla g \cdot \nabla h)\ \mathrm{d}^n r. \tag{D.5}$$

Appendix E

The Derivation of Forward, Backward Equations and Gradient of Loss Functional

In this appendix, we document the details of calculations of functional derivatives of the loss functional $\mathcal{L}$ with respect to $(\underline{\psi}, \underline{\lambda}, \underline{u})$ mentioned in Chapter 3, specifically the derivations of Eqs. 3.9 - 3.17.

From Eq. 3.8, we know:

$$\mathcal{L}[\underline{\psi}, \underline{\lambda}, \underline{u}] = \mathcal{J}[\rho[\underline{\psi}], \underline{u}] + \mathcal{F}[\underline{\psi}, \underline{\lambda}, \underline{u}], \tag{E.1}$$

where $\mathcal{J}[\rho[\underline{\psi}], \underline{u}]$ is given in Eq. 3.7 and $\mathcal{F}[\underline{\psi}, \underline{\lambda}, \underline{u}]$ is defined as:

$$\mathcal{F}[\underline{\psi}, \underline{\lambda}, \underline{u}] = \mathrm{Re} \sum_{j=1}^{M} \int_0^T \int_\Omega \left(i \frac{\partial \psi_j}{\partial t} - \hat{H}_{\mathrm{KS}}[\underline{\psi}, \underline{u}, t] \psi_j \right) \bar{\lambda}_j \mathrm{d}x \mathrm{d}y \mathrm{d}t, \tag{E.2}$$

where $\bar{\lambda}_j$ represents the complex value of λ_j.

E.1 Calculating Functional Derivative With Respect to $\underline{\lambda}$

We first compute the functional derivative of $\mathcal{L}$ with respect to $\underline{\lambda}$. Since $\mathcal{J}$ does not depend on $\underline{\lambda}$ and $\mathcal{F}$ is linear in $\underline{\lambda}$, we obtain:

$$\begin{aligned} (D_{\lambda_k}\mathcal{L})\delta\lambda_k &= \lim_{\alpha \to 0} \frac{1}{\alpha} \left(\mathcal{L}[\underline{\psi}, \underline{\lambda} + \alpha \delta\lambda_k, \underline{u}] - \mathcal{L}[\underline{\psi}, \underline{\lambda}, \underline{u}] \right) \\ &= \mathrm{Re} \int_0^T \int_\Omega \left(i \frac{\partial \psi_k}{\partial t} - \hat{H}_{\mathrm{KS}}[\underline{\psi}, \underline{u}, t] \psi_k \right) \delta\bar{\lambda}_k \mathrm{d}x \mathrm{d}y \mathrm{d}t. \end{aligned} \tag{E.3}$$

Setting $(D_{\lambda_k}\mathcal{L})\delta\lambda_k = 0$ immediately gives back the time-dependent Kohn-Sham equation:

$$i \frac{\partial}{\partial t} \psi_k = \hat{H}_{\mathrm{KS}}[\underline{\psi}, \underline{u}, t] \psi_k. \tag{E.4}$$

E.2 Calculating Functional Derivative With Respect to $\underline{\psi}$

Since both $\mathcal{J}$ and $\mathcal{F}$ contain $\underline{\psi}$, we need to calculate $(D_{\psi_k}\mathcal{J})\delta\psi_k$ and $(D_{\psi_k}\mathcal{F})\delta\psi_k$.

We first focus on $(D_{\psi_k}\mathcal{F})\delta\psi_k$. Besides a linear part in ψ_k, $\mathcal{F}$ also contains a nonlinear part of ψ_k. Therefore, it is convenient to devide $\mathcal{F}$ into a linear part $\mathcal{F}_l$ and a nonlinear part $\mathcal{F}_n$ with the following definitions:

$$\mathcal{F}_l = \mathrm{Re}\sum_{j=1}^{M}\int_0^T\int_\Omega \left(i\frac{\partial\psi_j}{\partial t} - (-\nabla^2 + v_0 + v_{\mathrm{ctr}})\psi_j\right)\bar{\lambda}_j \mathrm{d}x\mathrm{d}y\mathrm{d}t, \tag{E.5}$$

$$\mathcal{F}_n = \mathrm{Re}\sum_{j=1}^{M}\int_0^T\int_\Omega -(v_{\mathrm{H}} + v_{\mathrm{xc}})\psi_j\bar{\lambda}_j \mathrm{d}x\mathrm{d}y\mathrm{d}t, \tag{E.6}$$

where we have simplified the notation. For example, we skip the mass term m^* and x, y subscripts in the Laplacian operator. Such simplification makes the notation easier and will not affect the derivation below.

We now calculate $(D_{\psi_k}\mathcal{F}_l)\delta\psi_k$ as:

$$\begin{aligned}(D_{\psi_k}\mathcal{F}_l)\delta\psi_k &= \lim_{\alpha\to 0}\frac{1}{\alpha}\left(\mathcal{F}_l[\underline{\psi} + \alpha\delta\psi_k, \underline{\lambda}, \underline{u}] - \mathcal{F}_l[\underline{\psi}, \underline{\lambda}, \underline{u}]\right)\\ &= \mathrm{Re}\int_0^T\int_\Omega\left(i\frac{\partial\delta\psi_k}{\partial t} - (-\nabla^2 + v_0 + v_{\mathrm{ctr}})\delta\psi_k\right)\bar{\lambda}_k\mathrm{d}x\mathrm{d}y\mathrm{d}t.\end{aligned} \tag{E.7}$$

Next, we apply integration by parts so that differential operators $\frac{\partial}{\partial t}$ and ∇^2 act on the adjoint variable $\bar{\lambda}_k$:

$$\begin{aligned}(D_{\psi_k}\mathcal{F}_l)\delta\psi_k =& -\mathrm{Re}\int_\Omega i\lambda_k(x,y,T)\delta\bar{\psi}_k(x,y,T)\mathrm{d}x\mathrm{d}y\\ &+ \mathrm{Re}\int_0^T\int_\Omega\left(i\frac{\partial\lambda_k}{\partial t} - (-\nabla^2 + v_0 + v_{\mathrm{ctr}})\lambda_k\right)\delta\bar{\psi}_k\mathrm{d}x\mathrm{d}y\mathrm{d}t,\end{aligned} \tag{E.8}$$

where we have used the fact that $\delta\psi_k(t = 0) = 0$ due to the initial condition of ψ_k, and that ψ_k and λ_k vanish on the boundary of the domain Ω.

Then, we compute the functional derivative of the nonlinear part $(D_{\psi_k}\mathcal{F}_n)\delta\psi_k$. Since v_{H} and v_{xc} depend on $\underline{\psi}$ through the electron density ρ (Eq. 3.5), we need the derivative of the density, which is computed as:

$$\begin{aligned}\frac{\partial\rho}{\partial\psi_k}\delta\psi_k &= \lim_{\alpha\to 0}\frac{1}{\alpha}\left(\rho[\underline{\psi}+\alpha\delta\psi_k]-\rho[\underline{\psi}]\right)\\ &= 2\mathrm{Re}\left(g_k\psi_k\delta\bar{\psi}_k\right).\end{aligned} \tag{E.9}$$

$\mathcal{F}_n$ contains two parts, the Hartree potential part $\mathcal{F}_H$:

$$\mathcal{F}_H = \mathrm{Re}\sum_{j=1}^{M}\int_0^T\int_\Omega v_{\mathrm{H}}\psi_j\bar{\lambda}_j\mathrm{d}x\mathrm{d}y\mathrm{d}t, \tag{E.10}$$

and the exchange-correlation potential part $\mathcal{F}_{xc}$:

$$\mathcal{F}_{xc} = \mathrm{Re}\sum_{j=1}^{M}\int_0^T\int_\Omega v_{\mathrm{xc}}\psi_j\bar{\lambda}_j\mathrm{d}x\mathrm{d}y\mathrm{d}t. \tag{E.11}$$

We compute the functional derivative of the exchange-correlation part $\mathcal{F}_{xc}$ as follows:

$$
\begin{aligned}
(D_{\psi_k}\mathcal{F}_{xc})\delta\psi_k &= \lim_{\alpha\to 0}\frac{1}{\alpha}\left(\mathcal{F}_{xc}[\underline{\psi}+\alpha\delta\psi_k,\underline{\lambda},\underline{u}]-\mathcal{F}_{xc}[\underline{\psi},\underline{\lambda},\underline{u}]\right)\\
&= \lim_{\alpha\to 0}\frac{1}{\alpha}\mathrm{Re}\sum_{j=1}^{M}\int_0^T\int_\Omega \big\{v_{\mathrm{xc}}[\rho[\underline{\psi}+\alpha\delta\psi_k]](\psi_j+\delta_{jk}\alpha\delta\psi_k)\\
&\qquad -v_{\mathrm{xc}}[\rho[\underline{\psi}]]\psi_j\big\}\,\bar{\lambda}_j\mathrm{d}x\mathrm{d}y\mathrm{d}t\\
&=\mathrm{Re}\sum_{j=1}^{M}\int_0^T\int_\Omega\left(\frac{\partial v_{\mathrm{xc}}}{\partial\rho}\frac{\partial\rho}{\partial\psi_k}\delta\psi_k\psi_j+v_{\mathrm{xc}}\delta_{jk}\delta\psi_j\right)\bar{\lambda}_j\mathrm{d}x\mathrm{d}y\mathrm{d}t\\
&=\mathrm{Re}\sum_{j=1}^{M}\int_0^T\int_\Omega\frac{\partial v_{\mathrm{xc}}}{\partial\rho}2\mathrm{Re}\left(g_k\psi_k\delta\bar{\psi}_k\right)\psi_j\bar{\lambda}_j\mathrm{d}x\mathrm{d}y\mathrm{d}t\\
&\qquad+\mathrm{Re}\int_0^T\int_\Omega v_{\mathrm{xc}}\delta\psi_k\bar{\lambda}_k\mathrm{d}x\mathrm{d}y\mathrm{d}t\\
&=\mathrm{Re}\sum_{j=1}^{M}\int_0^T\int_\Omega 2\frac{\partial v_{\mathrm{xc}}}{\partial\rho}g_k\psi_k\mathrm{Re}\left(\psi_j\bar{\lambda}_j\right)\delta\bar{\psi}_k\mathrm{d}x\mathrm{d}y\mathrm{d}t\\
&\qquad+\mathrm{Re}\int_0^T\int_\Omega v_{\mathrm{xc}}\lambda_k\delta\bar{\psi}_k\mathrm{d}x\mathrm{d}y\mathrm{d}t,
\end{aligned}
\tag{E.12}
$$

where we have used the identity $v_{\mathrm{xc}}[\rho[\underline{\psi}+\alpha\delta\psi_k]]=v_{\mathrm{xc}}[\rho[\underline{\psi}]]+\frac{\partial v_{\mathrm{xc}}}{\partial\rho}\frac{\partial\rho}{\partial\psi_k}\alpha\delta\psi_k+\mathcal{O}(\alpha^2)$ in the third line, and Eq. E.9 in the fourth line.

We can apply similar techniques to compute the functional derivative of $\mathcal{F}_H$. The only difference is that the Hartree potential v_{H} is determined by a Poisson equation:

$$
\nabla^2 v_{\mathrm{H}}=-\rho, \tag{E.13}
$$

where we again omit the x, y subscripts and dielectric constant ε^* for the notation ease. It can be shown [119] that for any simply connected two-dimensional domain Ω, there always exists a Green's function $G(x, y; x', y')$ satisfying

$$-\nabla^2 G(x, y; x', y') = \delta(x - x')\delta(y - y'), \tag{E.14}$$

such that:

$$v_{\mathrm{H}}(x, y) = \int_{\Omega'} G(x, y; x', y')\rho(x', y')\mathrm{d}x'\mathrm{d}y'. \tag{E.15}$$

We thus have the equation:

$$v_{\mathrm{H}}[\rho[\underline{\psi} + \alpha\delta\psi_k]] = v_{\mathrm{H}}[\rho[\underline{\psi}]] + \frac{\partial v_{\mathrm{H}}}{\partial \psi_k}\alpha\delta\psi_k + \mathcal{O}(\alpha^2), \tag{E.16}$$

where $\frac{\partial v_{\mathrm{H}}}{\partial \psi_k}\alpha\delta\psi_k$ is given by:

$$\frac{\partial v_{\mathrm{H}}}{\partial \psi_k}\delta\psi_k = \int_{\Omega'} G(x, y; x', y') 2\alpha \mathrm{Re}\left(g_k \psi_k(x', y')\delta\bar{\psi}_k(x', y')\right)\mathrm{d}x'\mathrm{d}y'. \tag{E.17}$$

Using the techniques in deriving Eq. E.12, we can compute $(D_{\psi_k}\mathcal{F}_H)\delta\psi_k$ as:

$$\begin{aligned}(D_{\psi_k}\mathcal{F}_H)\delta\psi_k = &\lim_{\alpha\to 0}\frac{1}{\alpha}\left(\mathcal{F}_H[\underline{\psi} + \alpha\delta\psi_k, \underline{\lambda}, \underline{u}] - \mathcal{F}_H[\underline{\psi}, \underline{\lambda}, \underline{u}]\right)\\ =&\mathrm{Re}\sum_{j=1}^{M}\int_0^T\int_\Omega \frac{\partial v_{\mathrm{H}}}{\partial \psi_k}\delta\psi_k\psi_j\bar{\lambda}_j\mathrm{d}x\mathrm{d}y\mathrm{d}t\\ &+ \mathrm{Re}\int_0^T\int_\Omega v_{\mathrm{H}}\delta\psi_k\bar{\lambda}_k\mathrm{d}x\mathrm{d}y\mathrm{d}t.\end{aligned} \tag{E.18}$$

The first term in the second line above can be expanded and computed as:

$$\begin{aligned}
&\mathrm{Re}\sum_{j=1}^{M}\int_0^T\int_\Omega \frac{\partial v_{\mathrm{H}}}{\partial \psi_k}\delta\psi_k\psi_j\bar{\lambda}_j\mathrm{d}x\mathrm{d}y\mathrm{d}t\\
=&\mathrm{Re}\sum_{j=1}^{M}\int_0^T\int_\Omega\int_{\Omega'} G(x,y;x',y')2\mathrm{Re}\left(g_k\psi_k(x',y')\delta\bar{\psi}_k(x',y')\right)\mathrm{d}x'\mathrm{d}y'\psi_j(x,y)\bar{\lambda}_j(x,y)\mathrm{d}x\mathrm{d}y\mathrm{d}t\\
=&\mathrm{Re}\sum_{j=1}^{M}\int_0^T\int_{\Omega'} 2\int_\Omega G(x,y;x',y')\mathrm{Re}\left(\psi_j(x,y)\bar{\lambda}_j(x,y)\right)\mathrm{d}x\mathrm{d}y g_k\psi_k(x',y')\delta\bar{\psi}_k(x',y')\mathrm{d}x'\mathrm{d}y'\mathrm{d}t\\
=&\mathrm{Re}\sum_{j=1}^{M}\int_0^T\int_\Omega 2v_{\mathrm{H}}[\mathrm{Re}\left(\psi_j\bar{\lambda}_j\right)]g_k\psi_k\delta\bar{\psi}_k\mathrm{d}x\mathrm{d}y\mathrm{d}t,
\end{aligned} \tag{E.19}$$

where $v_{\mathrm{H}}[\mathrm{Re}\left(\psi_j\bar{\lambda}_j\right)]$ is defined as:

$$v_{\mathrm{H}}[\mathrm{Re}\left(\psi_j\bar{\lambda}_j\right)](x,y) = \int_\Omega G(x,y;x',y')\mathrm{Re}\left(\psi_j(x',y')\bar{\lambda}_j(x',y')\right)\mathrm{d}x'\mathrm{d}y'. \tag{E.20}$$

Or we can compute $v_{\mathrm{H}}[\mathrm{Re}\left(\psi_j\bar{\lambda}_j\right)]$ by solving the Poisson equation below:

$$-\nabla^2 v_{\mathrm{H}}[\mathrm{Re}\left(\psi_j\bar{\lambda}_j\right)] = \mathrm{Re}\left(\psi_j\bar{\lambda}_j\right). \tag{E.21}$$

Next, we aim to compute $(D_{\psi_k}\mathcal{J})\delta\psi_k$. There are four terms: $\mathcal{J}_\beta$, $\mathcal{J}_\gamma$, $\mathcal{J}_\eta$ and $\mathcal{J}_\nu$, the first three terms of which contain $\underline{\psi}$ through the density ρ. It is relatively straightforward to compute functional derivatives of these terms; thus, we give their results below. The term $\mathcal{J}_\beta$ is given by:

$$\mathcal{J}_\beta = \frac{\beta}{2}\int_0^T\int_\Omega \left(\rho(x,y,t)-\rho_p(x,y,t)\right)^2\mathrm{d}x\mathrm{d}y\mathrm{d}t, \tag{E.22}$$

and its functional derivative is computed as:

$$
\begin{aligned}
(D_{\psi_k}\mathcal{J}_\beta)\delta\psi_k &= \lim_{\alpha\to 0}\frac{1}{\alpha}\left(\mathcal{J}_\beta[\underline{\psi}+\alpha\delta\psi_k]-\mathcal{J}_\beta[\underline{\psi}]\right) \\
&= \mathrm{Re}\int_0^T\int_\Omega 2\beta(\rho-\rho_p)g_k\psi_k\delta\bar{\psi}_k \mathrm{d}x\mathrm{d}y\mathrm{d}t.
\end{aligned}
\tag{E.23}
$$

The term $\mathcal{J}_\gamma$ is given by:

$$
\mathcal{J}_\gamma = \frac{\gamma}{2}\int_\Omega \left(\rho(x,y,T)-\rho_d(x,y)\right)^2 \mathrm{d}x\mathrm{d}y,
\tag{E.24}
$$

and its functional derivative is computed as:

$$
\begin{aligned}
(D_{\psi_k}\mathcal{J}_\gamma)\delta\psi_k &= \lim_{\alpha\to 0}\frac{1}{\alpha}\left(\mathcal{J}_\gamma[\underline{\psi}+\alpha\delta\psi_k]-\mathcal{J}_\gamma[\underline{\psi}]\right) \\
&= \mathrm{Re}\int_\Omega 2\gamma(\rho(T)-\rho_d)g_k\psi_k(T)\delta\bar{\psi}_k(T)\mathrm{d}x\mathrm{d}y.
\end{aligned}
\tag{E.25}
$$

The term $\mathcal{J}_\eta$ is given by:

$$
\mathcal{J}_\eta = \frac{\eta}{2}\int_\Omega \chi(x,y)\rho(x,y,T)\mathrm{d}x\mathrm{d}y,
\tag{E.26}
$$

and its functional derivative is computed as:

$$
\begin{aligned}
(D_{\psi_k}\mathcal{J}_\eta)\delta\psi_k &= \lim_{\alpha\to 0}\frac{1}{\alpha}\left(\mathcal{J}_\eta[\underline{\psi}+\alpha\delta\psi_k]-\mathcal{J}_\eta[\underline{\psi}]\right) \\
&= \mathrm{Re}\int_\Omega \eta\chi g_k\psi_k(T)\delta\bar{\psi}_k(T)\mathrm{d}x\mathrm{d}y.
\end{aligned}
\tag{E.27}
$$

Finally, setting $(D_{\psi_k}\mathcal{L})\delta\psi_k = 0$ and combing Eqs. E.8, E.12, E.18, E.23, E.25 and E.27 give the backward propagation equations for ajoint states, Eqs 3.9 - 3.10.

E.3 Calculating Functional Derivative With Respect to $\underline{u}$

We start by computing $(D_{u_k}\mathcal{F})\delta u_k$. Since $\mathcal{F}$ is linear in $\underline{u}$, it is simple to show:

$$\begin{aligned} (D_{u_k}\mathcal{F})\delta u_k &= \lim_{\alpha\to 0}\frac{1}{\alpha}\left(\mathcal{F}[\underline{\psi},\underline{\lambda},\underline{u}+\alpha\delta u_k]-\mathcal{F}[\underline{\psi},\underline{\lambda},\underline{u}]\right) \\ &= -\mathrm{Re}\sum_{j=1}^{M}\int_0^T\int_\Omega \delta u_k V_k\psi_j\bar{\lambda}_j \mathrm{d}x\mathrm{d}y\mathrm{d}t. \end{aligned} \tag{E.28}$$

Next, we compute $(D_{u_k}\mathcal{J})\delta u_k$. Note that only the term $\mathcal{J}_\nu$ depends on $\underline{u}$. We first discuss the case where $\mathcal{J}_\nu$ uses the L^2 norm. The term is defined as:

$$\mathcal{J}_\nu = \frac{\nu}{2}\sum_{k=1}^{C}\int_0^T u_k^2\mathrm{d}t, \tag{E.29}$$

and its functional derivative can be readily computed as:

$$\begin{aligned} (D_{u_k}\mathcal{J})\delta u_k &= \lim_{\alpha\to 0}\frac{1}{\alpha}\left(\mathcal{J}[\underline{\psi},\underline{u}+\alpha\delta u_k]-\mathcal{J}[\underline{\psi},\underline{u}]\right) \\ &= \int_0^T \nu u_k\delta u_k\mathrm{d}t. \end{aligned} \tag{E.30}$$

Therefore, we obtain the funtional derivative of $\mathcal{L}$:

$$(D_{u_k}\mathcal{L})\delta u_k = \int_0^T\left[\nu u_k - \mathrm{Re}\sum_{j=1}^{M}\int_\Omega V_k\psi_j\bar{\lambda}_j\mathrm{d}x\mathrm{d}y\right]\delta u_k\mathrm{d}t. \tag{E.31}$$

By the Riesz representation theorem [111, 11], we can identify the gradient $\nabla_{u_k}\mathcal{L}$ of $\mathcal{L}$ by

$$\langle\nabla_{u_k}\mathcal{L},\delta u_k\rangle_{L^2(0,T)} = (D_{u_k}\mathcal{L})\delta u_k. \tag{E.32}$$

The gradient of the loss functional when we use the L^2 norm is:

$$\nabla_{u_k}\mathcal{L} = \nu u_k - \mathrm{Re}\sum_{j=1}^{M}\int_{\Omega} V_k\psi_j\bar{\lambda}_j \mathrm{d}x\mathrm{d}y. \tag{E.33}$$

Next, we consider the case where the H^1 norm is used. In this case, $\mathcal{J}_\nu$ is defined as:

$$\mathcal{J}_\nu = \frac{\nu}{2}\sum_{k=1}^{C}\int_0^T \left(u_k^2 + \dot{u}_k^2\right)\mathrm{d}t, \tag{E.34}$$

and its functional derivative is computed as:

$$\begin{aligned}(D_{u_k}\mathcal{J})\delta u_k &= \int_0^T \nu\left(u_k\delta u_k + \dot{u}_k\delta\dot{u}_k\right)\mathrm{d}t \\ &= \int_0^T \nu\left(u_k - \ddot{u}_k\right)\delta u_k \mathrm{d}t,\end{aligned} \tag{E.35}$$

where we use integration by parts and the assumption that $u_k(0) = u_k(T) = 0$ in the last line.

We denote the H^1-Riesz representative of $(D_{u_k}\mathcal{L})\delta u_k$ by h_k. Therefore, we have:

$$\begin{aligned}\langle h_k, \delta u_k\rangle_{H^1(0,T)} &= \int_0^T \left(h_k\delta u_k + \dot{h}_k\delta\dot{u}_k\right)\mathrm{d}t \\ &= \int_0^T \left(h_k - \ddot{h}_k\right)\delta u_k \mathrm{d}t.\end{aligned} \tag{E.36}$$

By the Riesz representation theorem $\langle h_k, \delta u_k\rangle_{H^1(0,T)} = (D_{u_k}\mathcal{L})\delta u_k$, we obtain:

$$\int_0^T \left(h_k - \ddot{h}_k\right)\delta u_k \mathrm{d}t = \int_0^T \left(\nu\left(u_k - \ddot{u}_k\right) - \mathrm{Re}\sum_{j=1}^{M}\langle\lambda_j, V_k\psi_j\rangle\right)\delta u_k \mathrm{d}t. \tag{E.37}$$

If we write h_k as:

$$h_k = \nu u_k + f_k, \tag{E.38}$$

by substituting it into Eq. E.37, we can observe that f_k should satisfy the following:

$$f_k - \ddot{f}_k = -\mathrm{Re}\sum_{j=1}^{M} \langle \lambda_j, V_k \psi_j \rangle. \tag{E.39}$$

This concludes all derivations of functional derivatives of the loss functional $\mathcal{L}$ with respect to $(\underline{\psi}, \underline{\lambda}, \underline{u})$.

Appendix F

The Derivation of the Kinetic Propagator With Spatially-Varying Mass

In this appendix, we provide the derivation of the time-propagation formula given in Eq. 3.22 in the main text. Propagating wavefunctions only with the kinetic term amounts to solving the following free particle time-dependent Schrödinger equation with the spatially varying mass:

$$i\hbar\frac{\partial\psi(\mathbf{r},t)}{\partial t} = -\frac{\hbar^2}{2}\nabla\cdot\left(\frac{1}{m^*(\mathbf{r})}\nabla\psi(\mathbf{r},t)\right), \tag{F.1}$$

where we have explicitly included Planck's constant expressed in SI units. Given the initial wavefunction, $\psi(\mathbf{r}_0, t_0)$, at time t_0, the solution is:

$$\psi(\mathbf{r}, t) = \int \mathrm{d}^2\mathbf{r}_0 K(\mathbf{r}, t; \mathbf{r}_0, t_0)\psi(\mathbf{r}_0, t_0),\ t \geq t_0 \tag{F.2}$$

where $K(\mathbf{r}, t; \mathbf{r}_0, t_0)$ is the propagator or Green's function, which satisfies the following two properties:

$$\lim_{t\to t_0} K(\mathbf{r}, t; \mathbf{r}_0, t_0) = \delta^2(\mathbf{r} - \mathbf{r}_0), \tag{F.3}$$

$$i\hbar\frac{\partial K(\mathbf{r}, t; \mathbf{r}_0, t_0)}{\partial t} = -\frac{\hbar^2}{2}\nabla \cdot \left(\frac{1}{m^*(\mathbf{r})}\nabla K(\mathbf{r}, t; \mathbf{r}_0, t_0)\right),\ t > t_0, . \tag{F.4}$$

The differential equation in Eq. F.4 has no analytical solution due to the position-dependent coefficient. However, we can use a WKB expansion to approximate the solution since $\hbar \ll 1$ [120]. Inspired by the uniform free space propagator, the Green's function can be written as:

$$K(\mathbf{r}, t; \mathbf{r}_0, t_0) = \left(\frac{1}{2\pi\hbar}\right)^2 \int \mathrm{d}^2\mathbf{k} \exp\left(-i\frac{\mathbf{k}\cdot\mathbf{r}_0}{\hbar}\right) \exp\left(\frac{i}{\hbar}\sum_{n=0} \hbar^n S_n(\mathbf{r}, t; t_0; \mathbf{k})\right), \tag{F.5}$$

where the exponent is expanded as a series in powers of $\hbar$. A direct application of Eq. F.3 gives:

$$\begin{aligned} S_0(\mathbf{r}, t_0; t_0; \mathbf{k}) &= \mathbf{k}\cdot\mathbf{r}, \\ S_j(\mathbf{r}, t_0; t_0; \mathbf{k}) &= 0,\ j \geq 1. \end{aligned} \tag{F.6}$$

Substituting Eq. F.5 into Eq. F.4, and comparing powers of $\hbar$ gives a set of equations to determine S_n:

$$\begin{gathered}\frac{\partial S_0}{\partial t} + \frac{(\nabla S_0)^2}{2m^*} = 0, \\ \frac{\partial S_j}{\partial t} - \frac{i}{2}\left(\nabla \frac{1}{m^*}\right) \cdot \nabla S_{j-1} - \frac{i}{2m^*}\nabla^2 S_{j-1} + \frac{1}{2m^*}\left(\sum_{k=0}^{j} \nabla S_k \cdot \nabla S_{j-k}\right) = 0,\ j \geq 1.\end{gathered} \tag{F.7}$$

To solve these nonlinear differential equations, we assume a short time interval $\Delta t = t - t_0 \ll 1$ and expand S_n in powers of Δt:

$$S_n(\mathbf{r}, t_0 + \Delta t; t_0; \mathbf{k}) = \sum_{j=0} c_{nj}(\mathbf{r}; t_0; \mathbf{k})(\Delta t)^j. \tag{F.8}$$

Similarly, substituting this back into Eq. F.7 and collecting terms with the same powers of Δt gives the coefficient functions c_{nj}:

$$\begin{aligned} & c_{00} = \mathbf{k} \cdot \mathbf{r},\ c_{01} = -\frac{\mathbf{k}^2}{2m^*},\ c_{02} = \frac{\mathbf{k}^2 \mathbf{k}}{2m^*} \cdot \left(\nabla \frac{1}{m^*}\right),\ \cdots . \\ & c_{10} = 0,\ c_{11} = \frac{i\mathbf{k}}{2} \cdot \left(\nabla \frac{1}{m^*}\right), \\ & c_{12} = -\frac{i\mathbf{k}^2}{4m^*}\nabla^2 \frac{1}{m^*} - \frac{i\mathbf{k}^2}{4}\left(\nabla \frac{1}{m^*}\right)^2 - \frac{i\mathbf{k}}{2m^*} \cdot \left(\nabla\nabla \frac{1}{m^*}\right) \cdot \mathbf{k}\ , \cdots \end{aligned} \tag{F.9}$$

Finally, we arrive at the wavefunction, $\psi(\mathbf{r}, t_0 + \Delta t)$, propagated from $\psi(\mathbf{r}_0, t_0)$, which obeys the dynamics of Eq. F.1:

$$\begin{aligned}
&\psi(\mathbf{r}, t_0 + \Delta t) \\
&= \int \mathrm{d}^2\mathbf{r}_0 K(\mathbf{r}, t + \Delta t; \mathbf{r}_0, t_0)\psi(\mathbf{r}_0, t_0) \\
&\approx \left(\frac{1}{2\pi\hbar}\right)^2 \int\int \exp\left(i\frac{\mathbf{k}\cdot(\mathbf{r}-\mathbf{r}_0)}{\hbar} - i\frac{\mathbf{k}^2}{2m^*\hbar}\Delta t\right) \exp\left(\frac{\mathbf{k}\cdot\nabla m^*}{2m^{*2}}\Delta t\right)\psi(\mathbf{r}_0, t_0)\mathrm{d}^2\mathbf{r}_0\mathrm{d}^2\mathbf{k} \quad \text{(F.10)} \\
&\approx \int \exp\left(i\frac{\mathbf{k}\cdot\mathbf{r}}{\hbar} - i\frac{\mathbf{k}^2}{2m^*\hbar}\Delta t\right) \exp\left(\frac{\mathbf{k}\cdot\nabla m^*}{2m^{*2}}\Delta t\right)\psi(\mathbf{k}, t_0)\mathrm{d}^2\mathbf{k} \\
&\approx \int \exp\left(i\frac{\mathbf{k}\cdot\mathbf{r}}{\hbar}\right)\mathcal{K}(\mathbf{r}, \mathbf{k})\psi(\mathbf{k}, t_0)\mathrm{d}^2\mathbf{k},
\end{aligned}$$

where we have used the first-order time propagator in the second line. The Fourier transform of the wavefunction in the third line of Eq. F.10 is defined as:

$$\psi(\mathbf{k}, t_0) = \left(\frac{1}{2\pi\hbar}\right)^2 \int \exp\left(-i\frac{\mathbf{k}\cdot\mathbf{r}_0}{\hbar}\right)\psi(\mathbf{r}_0, t_0)\mathrm{d}^2\mathbf{r}_0, \tag{F.11}$$

and the first-order kernel, $\mathcal{K}(\mathbf{r}, \mathbf{k})$, in the last line of Eq. F.10 is given by:

$$\mathcal{K}(\mathbf{r}, \mathbf{k}) = \exp\left(-i\frac{\mathbf{k}^2}{2m^*\hbar}\Delta t\right) \exp\left(\frac{\mathbf{k}\cdot\nabla m^*}{2m^{*2}}\Delta t\right). \tag{F.12}$$

The MISTER-T software package uses the expression for the second-order kernel, which is given by:

$$
\begin{aligned}
&\mathcal{K}(\mathbf{r},\mathbf{k}) \\
=&\exp\left\{-i\frac{\mathbf{k}^2}{2m^*\hbar}\Delta t+\frac{i\mathbf{k}^2\mathbf{k}}{2m^*\hbar}\cdot\left(\nabla\frac{1}{m^*}\right)\Delta t^2\right\}\cdot \\
&\exp\left\{-\frac{\mathbf{k}}{2}\cdot\left(\nabla\frac{1}{m^*}\right)\Delta t+\left(\frac{\mathbf{k}^2}{4m^*}\nabla^2\frac{1}{m^*}+\frac{\mathbf{k}^2}{4}\left(\nabla\frac{1}{m^*}\right)^2+\frac{\mathbf{k}}{2m^*}\cdot\left(\nabla\nabla\frac{1}{m^*}\right)\cdot\mathbf{k}\right)\Delta t^2\right\}.
\end{aligned}
\tag{F.13}
$$

If the mass is constant over space, one can check that the propagated wavefunction, $\psi(\mathbf{r},t_0+\Delta t)$, reduces to $\int\exp\left(i\frac{\mathbf{k}\cdot\mathbf{r}}{\hbar}\right)\exp\left(-i\frac{\mathbf{k}^2}{2m\hbar}\Delta t\right)\psi(\mathbf{k},t_0)\mathrm{d}^2\mathbf{k}$, which amounts to computing $\exp\left(i\frac{\Delta t}{2m\hbar}\nabla^2\right)\psi(\mathbf{r}_0,t_0)$ in Fourier space.

The WKB approach is a “semiclassical” approximation in the sense that it is valid in the limit of $\hbar \ll 1$ or the mass is “slowly varying” compared to the de Broglie wavelength. Note that in Eq. F.9, we truncate at the linear term and consider only the first two terms, S_0 and S_1. Such a truncation requires two relations to be satisfied [120]:

$$
\begin{gathered}
\hbar S_{n+1} \ll S_n,\ n \geq 0, \\
\hbar S_2 \ll 1.
\end{gathered}
\tag{F.14}
$$

Consequently, to make the second-order approximation for the kernel (Eq. F.13) valid, the following three inequalities must hold:

$$\left|\frac{m^*}{\mathbf{k}^2}\left(\mathbf{k}\cdot\nabla\frac{1}{m^*}\right)\hbar\right| \ll 1, \tag{F.15}$$

$$\left|\mathbf{k}\cdot\left(\nabla\frac{1}{m^*}\right)\Delta t\right| \ll 1, \tag{F.16}$$

$$\frac{\mathbf{k}^2\Delta t}{2m^*\hbar}\left|\mathbf{k}\cdot\left(\nabla\frac{1}{m^*}\right)\Delta t\right|^2 \ll 1. \tag{F.17}$$

The physical meaning of Eq. F.15 is more clear in the following form:

$$\frac{m^*}{|\nabla m^*|} \gg \frac{\hbar}{|\mathbf{k}|} = \frac{\lambda}{2\pi}, \tag{F.18}$$

which shows that $\lambda/2\pi$ should be small compared to the characteristic distance over which the mass varies appreciably. If we use the Dirichlet boundary condition where the wavefunctions $\underline{\psi}$ are set to zero at the boundary, the wavelength, λ, can be estimated numerically by $D = n\lambda, n = 1, 2, 3, \cdots$, where D denotes the size of the system. Roughly speaking, the characteristic distance, $m^*/|\nabla m^*|$, must be large compared to the size D. The other two inequalities in Eqs. F.16 and F.17 impose constraints on the time step, Δt.

Appendix G

Accuracy of Pseudoskeleton Decomposition Based on Pivoted QR Factorization and Random Sampling

In this work, we utilize a pseudoskeleton decomposition [121, 122, 112] to accelerate the computation of propagated wavefunctions and adjoint states. Specifically, the decomposition uses an approach based on pivoted QR factorization and random sampling [113], which has been shown to be effective in constructing low-rank approximations for kernels and solving time-dependent Schrödinger equations [114].

Here, we assess the accuracy of Algorithm 1, which was utilized to construct an approximation of the second-order kernel (Eq. F.13) within the MISTER-T code. Specifically, in Subsection 3.5.3, we explore a dynamic system where the effective mass gradually changes throughout the domain, and consequently, the kernel, given by Eq. F.13, varies with both position $\mathbf{r}$ and momentum $\mathbf{k}$. To quantify the accuracy of Algorithm 1, we define the relative error metric, ε, as follows:

$$\varepsilon = \frac{\sqrt{\sum_{i,j} \left| \mathcal{K}_{\mathrm{pd}}(\tilde{\mathbf{r}}_i, \tilde{\mathbf{k}}_j) - \mathcal{K}(\tilde{\mathbf{r}}_i, \tilde{\mathbf{k}}_j) \right|^2}}{\sqrt{\sum_{i,j} \left| \mathcal{K}(\tilde{\mathbf{r}}_i, \tilde{\mathbf{k}}_j) \right|^2}}, \tag{G.1}$$

where $\mathcal{K}(\tilde{\mathbf{r}}_i, \tilde{\mathbf{k}}_j)$ represents the kernel's direct evaluation at the specified position and momentum points, and $\mathcal{K}_{\mathrm{pd}}(\tilde{\mathbf{r}}_i, \tilde{\mathbf{k}}_j)$ is the approximation obtained via the pseudoskeleton decomposition. Figure G.1 illustrates the relative error associated with the pseudoskeleton decomposition across varying rank values, r_ε (see Eq. 3.26), for different numbers of elements. This analysis demonstrates that the error introduced by the pseudoskeleton decomposition can be effectively managed and kept very small by selecting a proper rank value. In Table G.1, we catalog the minimal rank values, r_ε, necessary to maintain certain predefined relative errors across the number of elements, N, and timesteps, Δt.

To further examine the effect of the pseudoskeleton decomposition on solving the time-dependent Kohn-Sham equation, we propagate the wavefunction using both the exact kernel expression (Eq. F.13) and the approximation provided by Algorithm 1. We then evaluate the relative L1 errors in electron densities derived from various rank values, r_ε. This analysis involves solving for the ground state as described in Section 3.5.3 and propagating this state under a sinusoidal control field given by $u(t) = \kappa \sin(\pi t / t_0)$, with $\kappa = 10^{-1}$ a.u. and $t_0 = 1$ a.u. Figure G.2 depicts the relative L1 error in the electron density as a function

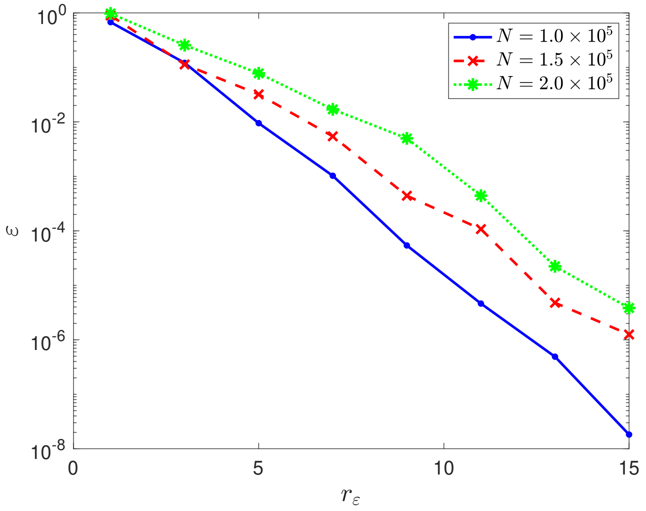

Figure G.1: Relative error, ε, of the pseudoskeleton decomposition as a function of rank, r_ε, for different numbers of elements N, at $\Delta t = 0.01$ a.u.

of r_ε at the final time $t = 1$ a.u. for a system size of $N = 1.0 \times 10^5$ and a timestep $\Delta t = 0.01$ a.u. The relative L1 error was calculated as $||\rho_{\text{pd}} - \rho||_1/||\rho||_1$, where ρ_{pd} is the electron density evolved using the kernel approximation from the pseudoskeleton decomposition, and ρ is the density evolved using the kernel's exact expression. It is crucial to highlight that the direct computation using Eq. F.13 requires significant execution time and extensive memory resources, often rendering it impractical for dense mesh grids and long-time propagations. In contrast, the pseudoskeleton decomposition approach exhibits a very small error with considerable advantages in computational speed and memory efficiency.

	$\Delta t = 0.01$ a.u.			$\Delta t = 0.001$ a.u.		
ε	10^{-5}	10^{-6}	10^{-7}	10^{-5}	10^{-6}	10^{-7}
$N = 1.0 \times 10^5$	11	13	15	5	6	8
$N = 1.5 \times 10^5$	13	16	17	6	7	8
$N = 2.0 \times 10^5$	15	17	20	6	8	10

Table G.1: Smallest value of r_ε required to achieve the prescribed relative error, ε, for different number of elements, N, and timesteps, Δt.

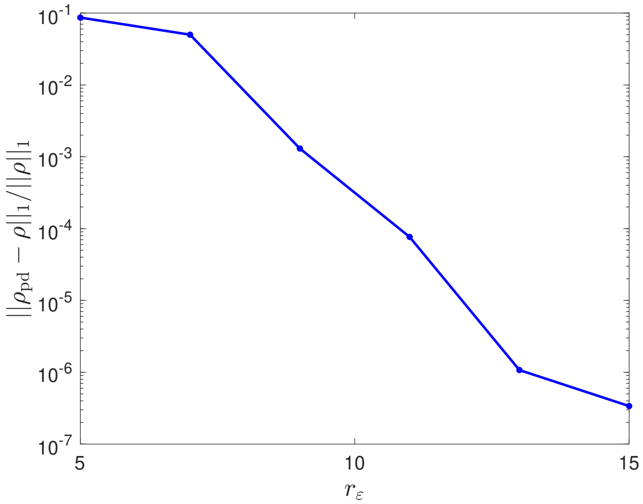

Figure G.2: Relative L1 errors of electron density at final time $t = 1$ a.u., as a function of values of rank r_ε. $N = 1.0 \times 10^5$. $\Delta t = 0.01$ a.u.

Appendix H

Rates of Convergence for Solution of the Forward Time-Dependent Kohn-Sham Equation

In this appendix, we examine the convergence rates of the forward time-dependent Kohn-Sham solution with respect to the finite-element mesh size, h, and time step, Δt. We use the example from Section 3.5.2 as the benchmark system for studying convergence rates.

We start by examining the convergence with respect to mesh size. To discretize the space, we utilize the Delaunay triangulation algorithm within MATLAB, which generates a Delaunay-triangulated grid of points and uses a set of local basis functions that are linear on each element [52]. To isolate the spatial discretization as the primary source of error, thereby minimizing contributions from time-discretization and pseudoskeleton decomposition errors, we use a very small timestep of $\Delta t = 0.0005$ a.u. for the wavefunction propagation. Additionally, employing a uniform effective mass helps eliminate errors arising from the pseudoskeleton decomposition. For this analysis, we first calculated the ground state and then propagated this state under a sinusoidal control field given by $u(t) = \kappa \sin(\pi t/t_0)$, where $\kappa = 0.001$ a.u. and $t_0 = 1$ a.u. Figure H.1a depicts the convergence rate of the relative L1 error in the electron density as a function of mesh size h at the final time $t = 1$ a.u. The relative L1 error was calculated as $||\rho_h - \rho_{h,\mathrm{ref}}||_1/||\rho_{h,\mathrm{ref}}||_1$, where ρ_h is the electron density computed with mesh size h, and $\rho_{h,\mathrm{ref}}$ is the reference electron density obtained with a finer mesh of $h = 0.03$ a.u. Through fitting the data to a power law of the form $||\rho_h - \rho_{h,\mathrm{ref}}||_1/||\rho_{h,\mathrm{ref}}||_1 \propto h^q$, we obtain $q = 3.09$ with an R^2 value of 0.999.

Next, we analyzed the convergence with respect to temporal discretization. For this analysis, we used a refined mesh grid with $h = 0.03$ a.u. to suppress errors stemming from the spatial discretization. We then propagated the ground state using various timesteps, Δt. Figure H.1b depicts the convergence rate of the relative L1 error in the electron density as a function of the timestep at the final time $t = 1$ a.u. The relative L1 error was computed as $||\rho_{\Delta t} - \rho_{\Delta t,\mathrm{ref}}||_1/||\rho_{\Delta t,\mathrm{ref}}||_1$, where $\rho_{\Delta t}$ is the final electron density computed with time step Δt, and $\rho_{\Delta t,\mathrm{ref}}$ denotes the reference value obtained using a smaller time step with $\Delta t = 0.005$ a.u. By fitting the data to a power law, $||\rho_{\Delta t} - \rho_{\Delta t,\mathrm{ref}}||_1/||\rho_{\Delta t,\mathrm{ref}}||_1 \propto (\Delta t)^q$, we obtain a convergence rate of $q = 2.04$, which agrees well with the second-order temporal accuracy of the Strang splitting method [11] employed in this work.

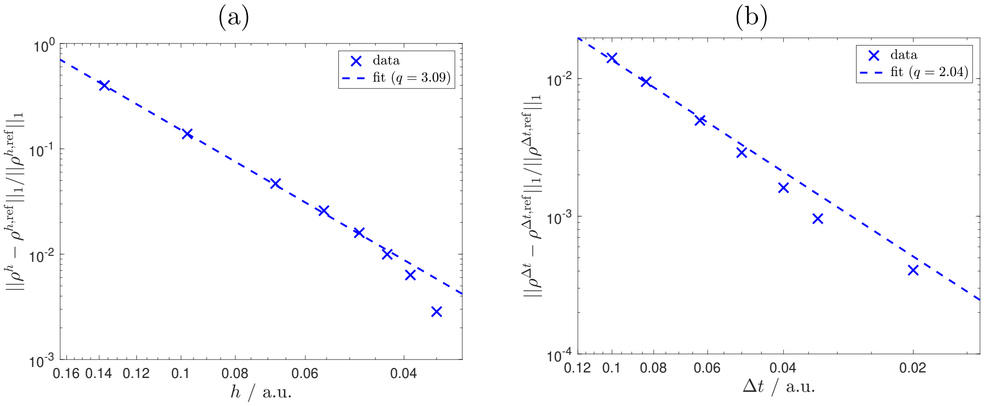

Figure H.1: Rate of convergence with respect to (a) finite-element mesh size, h, and (b) time step Δt.